An Investigation into Metallic Impurities in Silicon for Solar Cells

A thesis submitted to the University of Manchester for the degree of Doctor of Philosophy in the Faculty of Engineering and Physical Sciences

2015

Simon Leonard

Electrical and Electronic Engineering

Contents

Word Count: 30,057

List of Figures:

List of Abbreviations:

ε	Permittivity of Material
η	Power Conversion Efficiency
σ_n	Apparent Capture Cross Section
A	Amps
C	Capacitance
CB	Conduction Band
CCGT	Combined Cycle Gas Turbine
c_n	Capture Rate
Cz	Czochralski
DLTS	Deep Level Transient Spectroscopy
E_A	Activation Energy
EDX	Energy Dispersive X-ray
FIT	Feed in Tariff
FLH	Full Load Hours
FF	Fill Factor
FZ	Float Zone
GHI	Global Horizontal Irradiation
HAADF	High Angle Annular Dark Field
I_{SC}	Short Circuit Current
IV	Current Voltage
k_B	Boltzmann Constant
LCOE	Levelized cost of electricity
L_D	Debye Tail Length
LDLTS	Laplace Deep Level Transient Spectroscopy
LED	Light Emitting Diode
MCTS	Minority Carrier Transient Spectroscopy
MG	Metallurgical Grade
N_D	Donor Concentration
N_T	Trap Concentration
P_{in}	Power Delivered by Photons
PV	Photovoltaic
q	Charge of an Electron
Q	Charge
RF	Radio Frequency
SIMS	Secondary Ion Mass Spectroscopy
SRH	Shockley-Read-Hall
STEM	Scanning Transmission Electron Microscopes
T	Temperature
TEM	Transmission Electron Microscopy
t_p	Filling Pulse
UMIST	University of Manchester Institute of Science and Technology
V	Volts
VB	Valence Band
V_{OC}	Open Circuit Voltage
w	Depletion Width
W	Watts
v_n	Thermal Velocity for Electrons

List of Papers and Contributions

Included in Thesis

Passivation of titanium by hydrogen in silicon

S. Leonard, V. P. Markevich, A. R. Peaker, and B. Hamilton, Appl. Phys. Lett., vol. 103, no. 13, p. 132103, 2013.

Experimental work: S. Leonard

Writing: S. Leonard

Editing, discussion and corrections: V. P. Markevich, A. R. Peaker, and B. Hamilton

Titanium in silicon: Lattice positions and electronic properties

V. P. Markevich, S. Leonard, A. R. Peaker, B. Hamilton, A. G. Marinopoulos, and J. Coutinho, Appl. Phys. Lett., vol. 104, no. 15, p. 152105, Apr. 2014.

Experimental work: V. P. Markevich and S. Leonard

Modelling: A. G. Marinopoulos, and J. Coutinho

Writing: V. P. Markevich

Editing, discussion and corrections: S. Leonard, A. R. Peaker, B. Hamilton, A. G. Marinopoulos, and J. Coutinho

Evidence for an-Iron Hydrogen Complex in p-type Silicon

S. Leonard, V. P. Markevich, A. R. Peaker, B. Hamilton and J. D. Murphy, Appl. Phys. Lett., vol. 107, p. 032103, 2015.

Experimental work: S. Leonard

Writing: S. Leonard

Editing, discussion and corrections: V. P. Markevich, A. R. Peaker, B. Hamilton and J. D. Murphy

Samples provided by: J. D. Murphy

Molybdenum nano-precipitates in silicon: A TEM and DLTS study

S. Leonard, V. P. Markevich, A. R. Peaker, B. Hamilton, K. Youssef, and G. Rozgonyi, Phys. Status Solidi, vol. 251, no. 11, pp. 2201–2204, Nov. 2014.

Experimental work: S. Leonard and V. P. Markevich

TEM: K. Youssef

Writing: S. Leonard

Editing, discussion and corrections: V. P. Markevich, A. R. Peaker, B. Hamilton, G. Rozgonyi

Electron Capture and Emission at Nanoscale Transition Metal Precipitates in Semiconductors

J. Jacobs, S. Leonard, V. P. Markevich, A. R. Peaker and B. Hamilton, Submitting to Phys. Rev. Lett.

Experimental work: S. Leonard

Modelling: J. Jacobs and B. Hamilton

Writing: J. Jacobs, B. Hamilton and S. Leonard

Editing, discussion and corrections: S. Leonard, A. R. Peaker and VP Markevich

Not Included in Thesis

Recombination via nano-precipitates ... a new mechanism for efficiency loss in solar silicon?

A. R. Peaker, B. Hamilton, S. Leonard, V. P. Markevich, K. Youssef, and G. Rozgonyi, in Proceedings IEEE 40th Photovoltaic Specialist Conference (PVSC) pp. 37–41, 2014.

Lattice Positions and Electronic Properties of Titanium in Silicon

A. G. Marinopoulos, J. Coutinho, V. P. Markevich, S. Leonard, A. R. Peaker, and B. Hamilton, in 29th European Photovoltaic Solar Energy Conference and Exhibition, pp. 804–808, 2014.

The University of Manchester

Abstract

Submitted by Simon Leonard for the degree of Doctor of Philosophy and entitled:

An Investigation into Metallic Impurities in Silicon for Solar Cells, 2015

Photovoltaics is an exciting area of research with the potential to completely change the world's energy landscape. Silicon still dominates the photovoltaics market and shows no sign of being overtaken by other materials systems for large scale manufacture. Huge strides have been made in recent years to reduce the cost of solar modules, mainly through the introduction of mass production solar panel plants. However producing very pure single crystalline silicon is still a relatively expensive, energy intensive process. If cheaper less pure silicon could be cast into multi-crystalline ingots, without significant losses to the conversion efficiency this could be a game changer in the photovoltaics industry. For this to happen we need to have greater knowledge and understanding of the role of metallic impurities in solar silicon. If we can find ways to passivate or getter these impurities in cost effective processes that lend themselves to mass production then this would be the key to cost effective solar energy.

In the work in this thesis I have investigated some of the most common and most harmful metallic impurities in silicon solar cells using a combination of Deep Level Transient Spectroscopy (DLTS), Capacitance Voltage (CV) measurements, Secondary Ion Mass Spectroscopy and Tunnelling Electron Microscopy (TEM). The specific transition metals I studied were iron, as it is one of the most common impurities and also titanium and molybdenum, because they are very harmful, have slow diffusivities and hard to get rid of with traditional gettering techniques. I have then looked at using hydrogen to electrically passivate these defects, and show evidence that hydrogen passivation is possible for interstitially incorporated titanium in silicon, but is unlikely to happen for interstitially incorporated iron.

Another important part of this thesis was the observation and characterisation of molybdenum nano-precipitates in silicon. We have observed the nano-precipitates both electrically in DLTS, and physically in TEM. The precipitates have very interesting electrical properties, and appear to be very strong minority carrier recombination centres, which would have a very negative effect on solar cell performance. It is possible that these nano-precipitates could form from any of the slow diffusing transition metals, and could be a key reason to explain the efficiency gap between low purity cast silicon and high purity single crystal silicon.

Declaration

No portion of the work referred to in the thesis has been submitted in support of an application for another degree or qualification of this or any other university or other institute of learning.

Copyright Statement

The Author

I completed a MEng in Materials Science and Engineering at The University of Manchester in 2011, including a year spent working on a Free Electron Laser at Daresbury Laboratory. During the PhD I have been part of the North West Nano Science (NOWNANO) Doctoral Training Centre.

Alternative Format Thesis

This thesis has been submitted in the alternative format to allow the incorporation of published and submitted papers. The format consists of a general introduction which includes: some chapters explaining the science behind the work in this thesis, a chapter explaining the experimental techniques, and a chapter explaining the significance and context of the work in the thesis. The five papers from my work in this thesis are then presented, with a final conclusion summing up the achievements of the PhD and the scope for further work. This format has been approved by the Faculty of Engineering and Physical Sciences (presentation of theses policy, section 7).

Acknowledgements

I would like to say a big thank you to everyone who I have worked with throughout my PhD. In particular I would like to thank my supervisor Bruce Hamilton, for accepting me on to the PhD, giving me the freedom to do what I was interested in and always having my best interests at heart. I would like to give a special thank you to Vladimir Markevich who gave me a lot of guidance during my PhD, showing me how to use everything in the lab, always being there to help me whenever I encountered problems and who taught me so much about the world of defects in semiconductors. I'd also like to give a big thank you to Tony Peaker for all of his help and support and the interesting discussions we had over the last few years.

I'd like to thank all the staff which have helped me along the way, in particular Eric Whittaker for the help he gave me at the start of my PhD, Mal McGowan for all of the fun times in the clean room and Ian Hawkins who I had many interesting discussions with while we were fixing things.

I have been lucky enough to meet lovely people wherever I have been, and would like to thank everyone I have spent the last few years with in the PSI, Sackville Street and everyone from the NoWNano DTC. Together we have had many fun conferences, trips to the pub and conversations to take our mind of science and lab work for a bit.

The last four years would not have been nearly as much fun without all of my old house mates and friends, who mainly helped me to keep my mind off science, but sometimes on it too. So a big thank you to Darcy, Wan, Foster, Asia, Ben, Beef, Harriet, Callum, Dicky, Lisa, Sev, Will, Landi and the rest of the guys who have made my time in Manchester so enjoyable. In particular a special thank you to Hannah for being the wonderful girlfriend that you are, always putting a smile on my face and supporting me through everything I do. You have truly made the last few years special!

Finally I would like to say a massive thank you to my family. My brother for his advice, support and friendship and my mum for being the best mother I could have wished for, who has helped and supported me in everything I have done and always been there for a chat. You have been an inspiration to me, so thank you for everything you have done!

1. Introduction

Civilization as we know it today is highly dependent on energy. Most conventional sources of energy are limited and produce greenhouse gases as a by-product which are harmful to our environment. Solar energy is a renewable energy which has no harmful by-products (apart from in the manufacturing of the solar panels), and occupies a growing position on the energy market. One key hindrance to solar cells is that existing technologies are either not sufficiently efficient, or are expensive compared to other energy sources. If the efficiency of solar panels could be increased in a cost effective way, it could be worth a huge amount to the solar industry. With the earth receiving more solar energy in an hour than the current annual global energy consumption, successfully harnessing this power could prove key to our future.

The market for solar photovoltaics (PV) has expanded rapidly due at least in part to subsidies provided by governments world wide. However in the long term the success of the industry will depend on the cost of solar generated power compared with other energy sources. Figure 1 shows the levelized cost of electricity (LCOE) in Germany in Euros/kWh by various different generation techniques. As can be seen the cost of electricity generated from solar photovoltaics is greater than coal sources and onshore wind, but for large scale utilities, it is now beginning to compete with combined cycle gas turbines (CCGT).

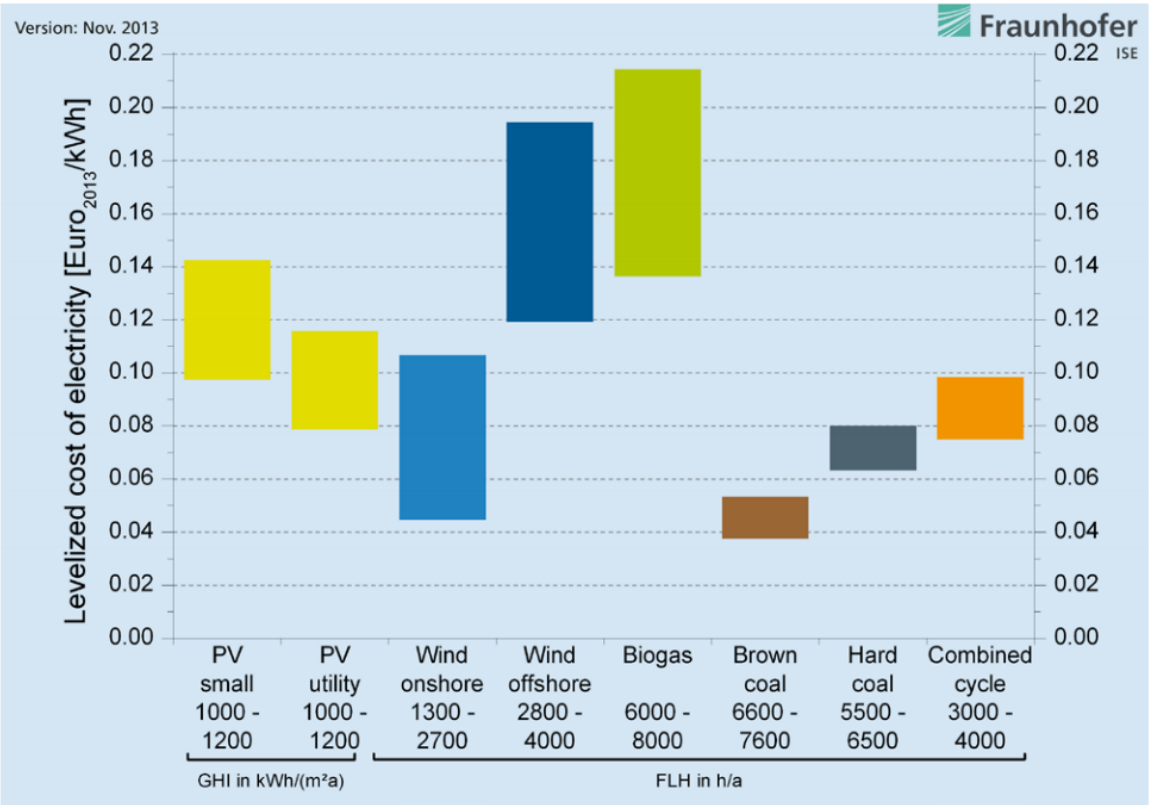

Figure 1. Reproduced from [1]**. LCOE of renewable energy technologies and conventional power plants at locations in Germany in 2013. The value under the technology refers in the case of PV to the insolation global horizontal irradiation (GHI) in kWh/(m²a), for the other technologies it refers to the number of full load hours (FLH) for the power plant per year. Specific investments are taken into account with a minimum and maximum value for each technology.**

The progress made with installed solar capacity in the last decade has been remarkable. The average increase in cumulative installed capacity has been 49% per year between 2003 and 2013, rising from less than 1 GW to over 135 GW [2]. This is shown in Figure 2, along with the countries with the largest installed PV capacity. Germany has the largest amount of PV capacity with over 36 GW, which provides 5.3% of their electricity needs. In total the global energy demand is ~10 TW a year, meaning in 2013 only 1.4% of the world's energy was provided by solar, showing there is still a huge way for the industry to go if it is to have a major impact on the global energy landscape.

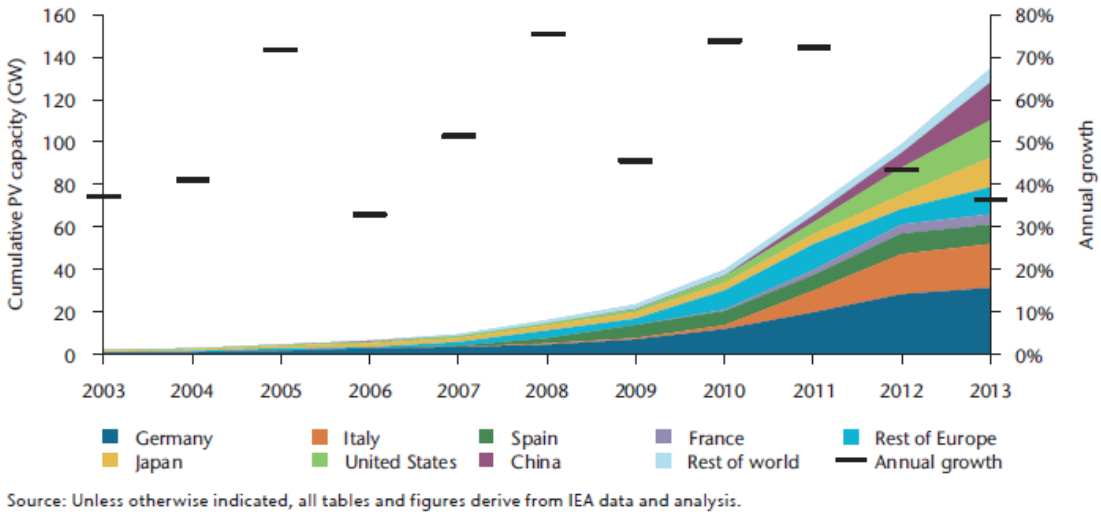

Figure 2. Figure reproduced from [2]**. Global cumulative growth of PV capacity (left hand axis) and annual growth rate (right hand axis signified by black lines).**

The price of solar modules has been consistently falling since they were introduced. In fact the cost reduction of solar modules fits very well to Swanson's law, which in 2006 stated that for every doubling of production of solar capacity, the module cost ($/Watt) will be reduced by 20% [3]. The present day curve is shown in Figure 3, and has actually increased to a 21.5% reduction in cost per doubling of solar capacity.

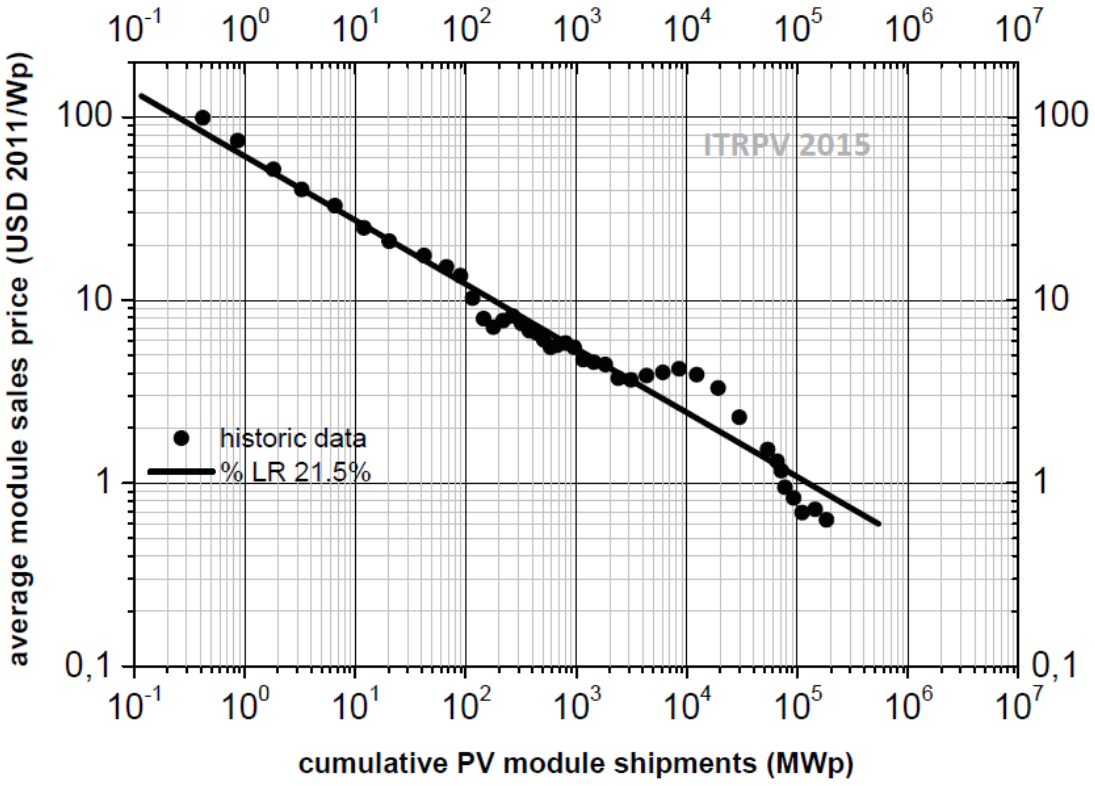

Figure 3. Reproduced from [4]**. Average solar module price as a function of cumulative PV module shipments.**

A lot of the growth of installed solar capacity currently comes from government initiatives, with many countries around the world introducing feed in tariffs (FITs) to encourage people to install solar panels. These schemes see the government pay solar panel owners for electricity that they feed back into the grid. There has been an almost direct correlation in Europe between FIT rates and solar panel uptake [5]. However as the price of solar panels continues to decrease the need for FITs will be reduced. The FIT rate for domestic dwellings dropped in the UK from 41.3 p/kWh in its introduction [6] to 13.39 p/kWh in 2015. In fact, in various countries around the world, such as Germany, Italy and some parts of the USA, grid parity with retail electricity cost has been reached, where the cost of generating energy from solar power is the same, or less than buying energy off the grid [2]. This of course is considerably more expensive than the generating cost from conventional power stations and it is grid parity with suppliers' costs that is the key stage in the evolution of solar

photovoltaics. If solar cell production continues to increase at the same rate as in the last decade while maintaining Swanson's law, then solar power could be of huge significance in the future. However this will only be possible by finding ways to continually decrease the cost per kWh of solar power. In this thesis I will be examining the effect of some specific metal impurities in silicon, with the ultimate goal to provide a deeper understanding of the role they play in the efficiency of silicon solar cells, so that cheaper manufacturing routes can be used to create high efficiency solar cells.

2. An Outline of how Solar Cells Work

To explain how a solar cell works a simple silicon solar cell will be described, but it must be emphasised that the cell structure to achieve optimum efficiency from specific silicon materials is now quite complex and beyond the remit of this thesis. For a detailed overview of high efficiency silicon solar cells see ref [7]. Solar cells are made from semiconductors, which are most commonly made from group IV materials, mainly silicon, or from a combination of group III and V materials. A semiconductor is a material which has a band gap which which is small enough for electrons to be excited from the valence band to the conduction band. . A band gap is a material specific property, and is the minimum amount of energy required to lift an electron from the material's highest valence band state to the conduction band minimum, producing a charge carrying electron and hole. It defines the forbidden energy region between the top of the valence band, where electrons occupy bonding states (but holes Bloch states) and the bottom of the conduction band, where the electrons can move freely and contribute to conduction (Bloch states). In a metal the conduction band overlaps with the valence band, meaning there is no barrier for electron movement and electrons near the Fermi surface are free to conduct. In an insulator the barrier (gap) is too big to be overcome in normal circumstances, preventing the many valence electrons from conducting. However in a semiconductor there is a small band gap which can be overcome by adding energy to an electron equal to or greater than the band gap. This is shown in Figure 4. The Valance band is made up of many different energy levels, as for each atom in a crystal there is an associated electron occupying each level, and Pauli's exclusion principle states no two electrons, with identical quantum numbers can be at the same electron energy. The Fermi energy is the energy of the highest electron occupied level in the crystal. As can be seen in Figure 4 this is located in the conduction band for the metallic conductor, meaning it conducts, and the band gap in the semiconductor and insulator meaning without external perturbation they will not conduct.

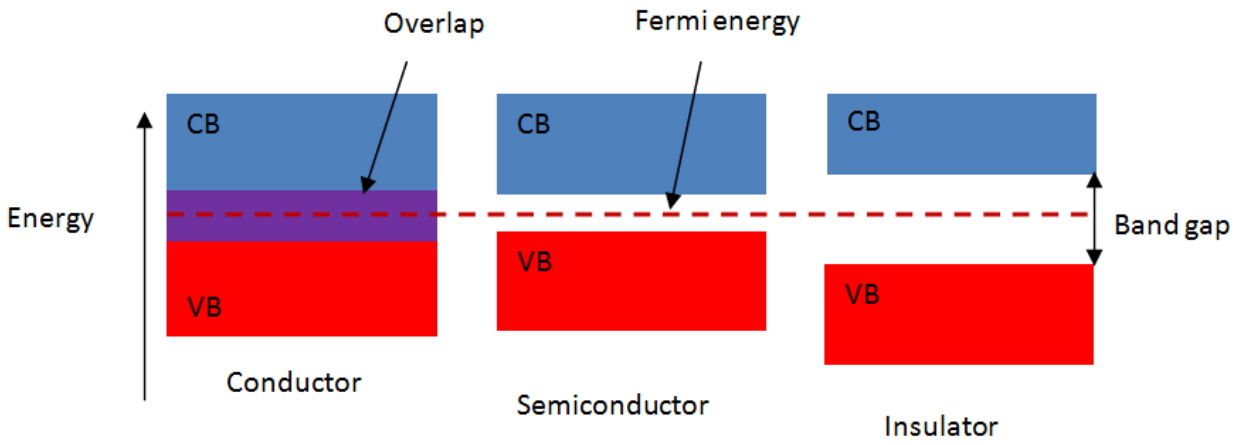

Figure 4. Energy band diagrams for a Conductor, Semiconductor and Insulator. CB is conduction band and VB is valence band. In the conductor the CB and VB overlap allowing conduction. The semiconductor and insulator have band gaps, with the insulator being much larger so that it typically isn't overcome.

In a semiconductor, when an electron is excited from the valence band into the conduction band the electron will become a charge carrier and contribute to conduction. However another conduction process also occurs when this happens. When the electron leaves the valence band it leaves an unoccupied energy level. Such an empty level (a broken bond) is mobile: the neighbouring electron may "move into this space", moving the broken bond. This process will happen repeatedly. The missing bond can be accounted for mathematically as a particle with a mass similar to that of an electron and with positive charge; this particle is known as a "hole" and will also conduct electricity in the semiconductor. This is shown in Figure 5.

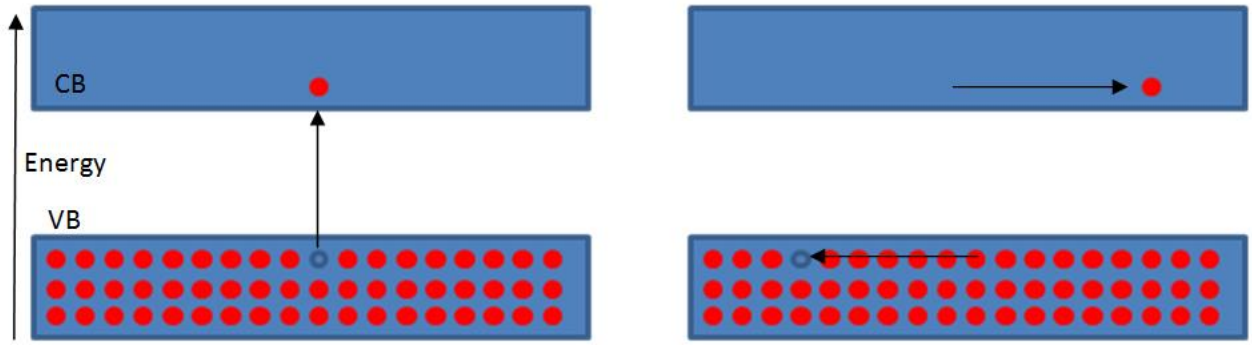

Figure 5. Energy band diagram showing how when an electron is excited into the conduction band it leaves a hole which will also conduct.

In reality the missing electrons near the top of the valence band allows the other electrons to gain mobility. These electrons have negative effective mass (and negative charge), and this combination is mathematically equivalent to particles with positive charge and positive mass. This is the origin of the term hole, which is convenient to use in order to quantify current flow. If a semiconductor does not have any impurity atoms it is called intrinsic. However by adding impurity atoms in what is known as 'doping' it is possible to increase the conductivity of a semiconductor. If you take a silicon atom, it has 4 outer shell electrons which can form 4 covalent bonds with other silicon atoms. By adding a group V element such as phosphorous, which has 5 outer shell electrons, it allows an extra electron to become a charge carrier. This is known as n-type doping. Similarly by adding a group III element such as boron, there will be an electron missing or a "hole" which becomes a charge carrier. This is called p-type doping and is shown in Figure 6. In a typical silicon semiconductor there are normally around 10^{23} atoms cm^{-3} and the doping levels will be around 10^{16} to 10^{17} atoms cm^{-3}.

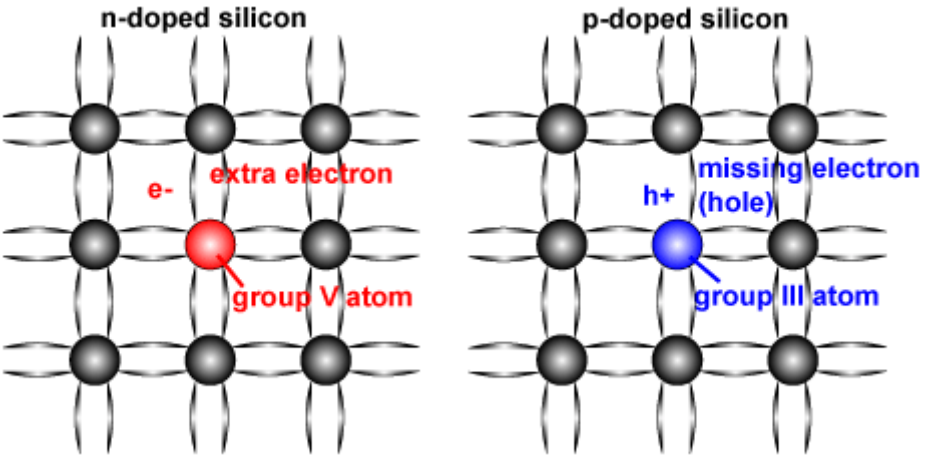

Figure 6. Picture reproduced from ref [8]**. Illustration of how doping silicon with group V atoms make it n-type and doping with group III atoms make it p-type.**

If a p-doped material is placed next to an n-doped material a p-n junction is formed. When this happens, at the junction the excess holes from the p-doped region diffuse to the n-doped region and excess electrons from the n-doped region diffuse to the p side. This leaves positive ion cores from the dopant atoms exposed on the n side and negative ion cores from the dopant atoms on the p side. This results in an electric field being created between the two regions, which sweeps carriers back into their original side, leaving a depletion region in the middle, where there are no carriers due to the electric field. This is illustrated in Figure 7 and shown on an energy band diagram in Figure 8.

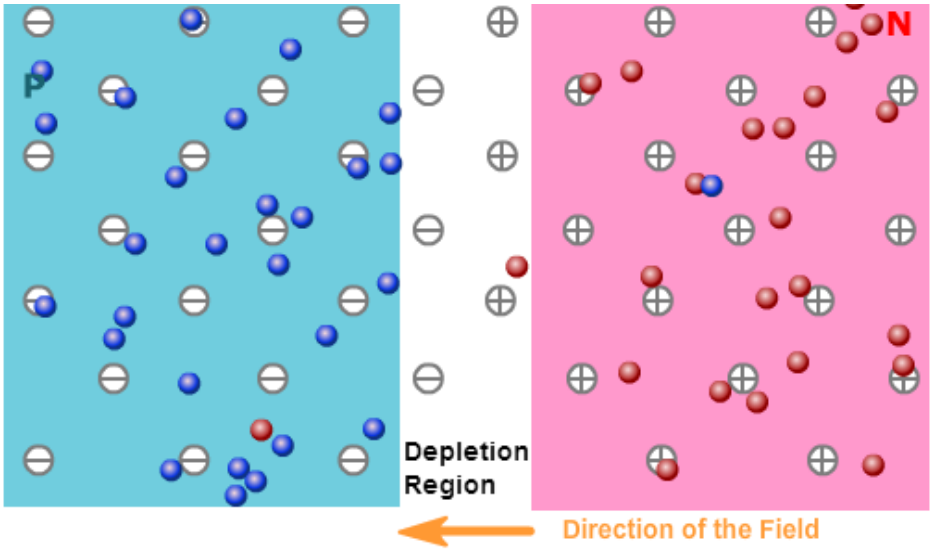

Figure 7. Picture reproduced from ref [8]**. Illustration of how a depletion region and electric field occur when p and n doped silicon is placed next to each other. Electrons are red and holes are blue. The diffusion of carriers across the junction leaves positive cores exposed which form an electric field.**

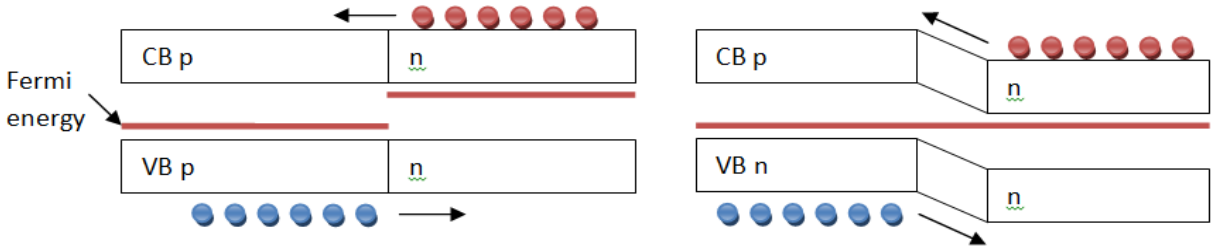

Figure 8. Left hand side shows the energy band diagram when a p and n doped material are initially placed next to each other. There is no barrier for the electrons (red) to move from the n to the p side, or for the holes (blue) to move from the p to the n side. The carriers will diffuse across until equilibrium is reached when the Fermi energies are level for the p and the n side, as shown on the right hand diagram. This is the point where the majority carriers climbing up the energy barrier is equal to the minority carriers falling back down.

When sunlight shines onto the solar cell it will be bombarded with a wide range of photons with different energies. If photons with energy less than the band gap of the material hit it, they will generally be transmitted, passing straight through the cell. However if photons with energy equal to or above the band gap of the material hit it, they may be absorbed, creating electron hole pairs. High

energy photons with energies greater than the band gap of the material will lose their excess energy as heat, meaning they will be inefficiently collected. This is shown in Figure 9.

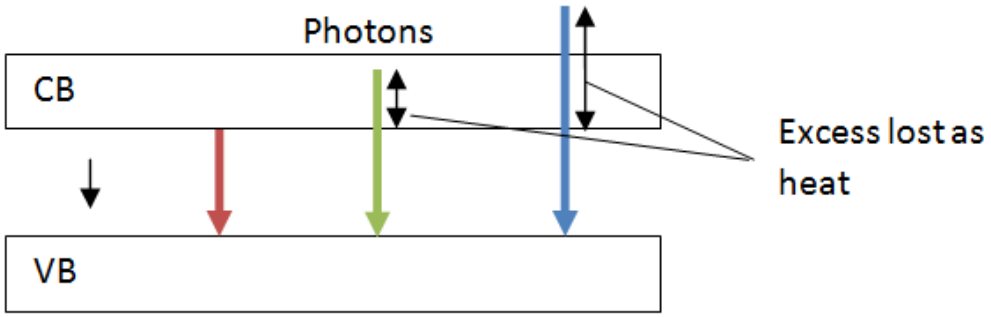

Figure 9. Band diagram showing what happens to different wavelength photons when they hit a semiconductor. The black arrow represents a high wavelength photon, with low energy which will pass straight through the semiconductor. The red arrow represents a photon with exactly the same energy as the band gap of the semiconductor which may create an electron hole pair if it is absorbed, losing no energy to heat. The green and blue arrows represent photons with high energies, which may also create electron hole pairs if they are absorbed but will also lose their excess energy as heat.

The influx of photons causes an increased number of both holes on the p side of the junction and electrons on the n side of the junction. This means that the electric field across the junction is reduced due to the increase of charge carriers, countering the ion cores. This results in an increase in carrier diffusion across the junction. If the cell is not connected the light induced current will be balanced by the forward bias of the cell as there can be no net current. This will cause a potential difference in the cell which is known as the open circuit voltage (V_{OC}) [9].

If the cell is connected when sunlight hits the cell and is absorbed, photons with a sufficient energy will excite the electrons into the conduction band, as they were before. With the cell now connected this will cause a current to flow meaning there will be more minority carriers on both sides of the junction. The electric field will not be diminished, and most of the carriers will be taken over the junction by drift from the electric field. The current in this scenario is known as the short circuit

current (I_{SC}) [9]. The open circuit voltage and short circuit current can be derived from an IV measurement (explained in more detail in chapter 4.1), and a typical IV plot from an illuminated solar cell is shown in Figure 10. From this plot the V_{OC} is obtained at the point where the current is equal to 0 and the I_{SC} is obtained when the voltage is equal to 0. The maximum power point, where the product of the current and voltage gives the highest power is also shown, with the current at this point being I_{mp} and the voltage V_{mp}. The fill factor (FF) is the measure of the squareness of the IV curve and is defined as:

$$FF = \frac{V_{mp} I_{mp}}{V_{OC} I_{SC}}$$

The efficiency of a solar cell can then be calculated as:

$$\eta = \frac{V_{OC} I_{SC} FF}{P_{in}}$$

where η is power conversion efficiency and P_{in} is the power delivered by photons hitting the solar cell.

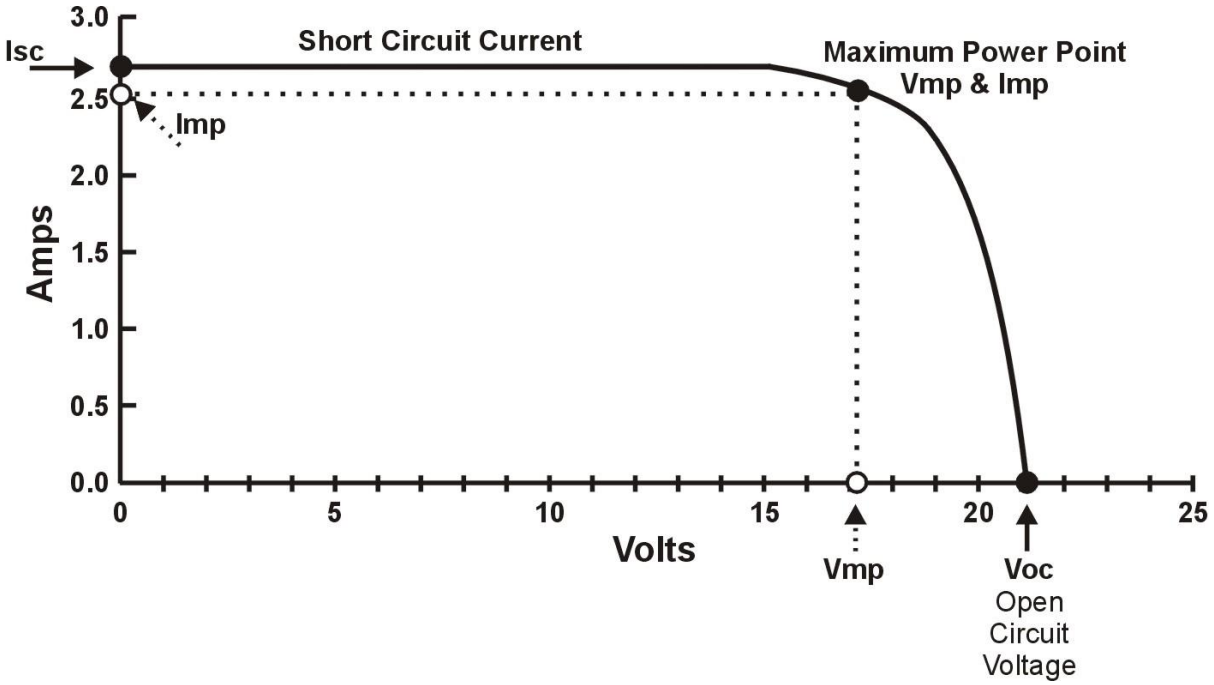

Figure 10. Typical IV plot for a solar cell under illumination.

3. Silicon

Crystalline silicon as of 2013 occupied 89% of the solar energy market and therefore is currently the market leader. The reason for this is mainly because it is relatively cheap to produce, very abundant and offers good efficiencies, up to 25% for mono-crystalline silicon, and up to 21% for multi-crystalline silicon [10]. Figure 11 shows the market share of different solar materials in 2013. Cadmium telluride technology is of comparable cost per watt but has issues associated with toxicity and is unlikely to expand its current market share. Amorphous silicon is potentially cheap to produce but offers lower efficiencies and suffers from major degradation problems. Other emerging technologies such as quantum dots, InGaN solar cells and multijunction solar cells are still too expensive or not efficient enough to compete with the existing silicon market.

Recently materials such as the perovskites have been seen to have considerable potential for the future but are still at the research stage with many problems associated with stability and reproducibility so they do not at the moment present a threat to silicon's dominant position [11].

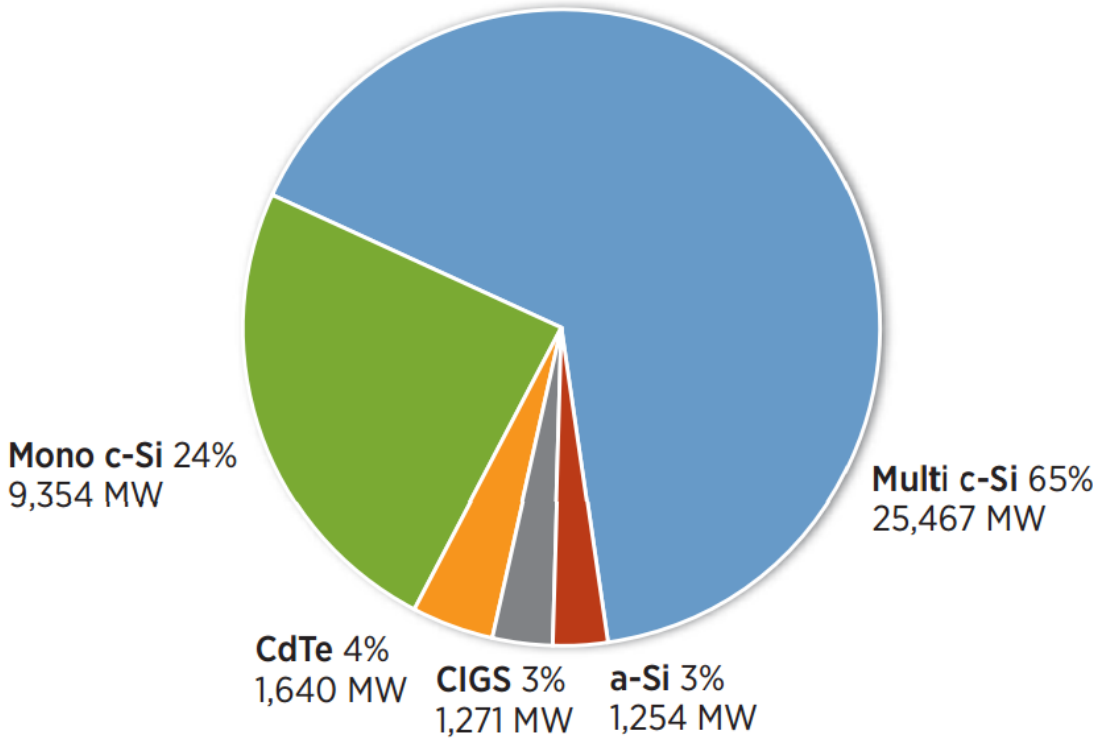

Figure 11. Reproduced from [12]**. Market share of PV technologies. Multi c-Si is multi-crystalline silicon, Mono c-Si is mono-crystalline silicon, CdTe is cadmium telluride solar cells, a-Si is amorphous silicon and CIGS is copper indium gallium selenide solar cells.**

Silicon is the second most abundant element of the earth's crust but is typically found in the form of complex silicate minerals or as silicon dioxide (commonly referred to as silica). Silica is the starting material in the production of solar cells. High purity silica is put in an electric arc furnace with a carbon source to produce silicon according to the following reaction:

$$SiO_2 + 2C = Si + 2CO$$

The resultant silicon is commonly referred to as Metallurgical Grade (MG) silicon and is typically about 99% pure with common impurities including Fe, Al, Ti, Mc, C, Ca, Mg, B, P, Mo and many more [13]. For most solar cells MG silicon is then converted to what is known as polysilicon via the Siemens Process. In this process MG silicon is reacted with dry hydrochloric acid in the presence of a

copper catalyst at around 250 ^{o}C to produce trichlorosilane ($SiHCl_3$). This will produce around 90% trichlorosilane which is then further purified by distillation and exchange resin absorptions typically operating around 1150 ^{o}C [14]. The reduction reaction for the process is:

$$SiHCl_3 + H_2 \leftrightarrow Si + 3HCl$$

Most techniques for making crystalline silicon solar cells start off with the raw material polysilicon, but the manufacturing steps are energy intensive and expensive. If solar cells could be made directly from MG silicon and maintain high efficiencies this would vastly reduce the cost of solar cell production. The most common processes for making crystalline silicon will be explained in the following chapters.

3.1. Czochralski Silicon

The Czochralski (Cz) process produces monocrystalline silicon and although more costly than cast silicon (described later) is very attractive because cells produced from this silicon process normally have higher efficiencies. A diagram of the Czochralski process is shown in Figure 12. Poly silicon is melted in a quartz crucible with the desired dopant atoms and a high purity crystal seed is dipped into the melt and slowly rotated and pulled out. By controlling the temperature gradient, rate of pulling and rotation speed, a single crystal can be pulled from the melt. Due to its high segregation coefficient for metallic impurities it produces very pure silicon with defect concentrations typically below 1×10^{11} cm^{-3}.

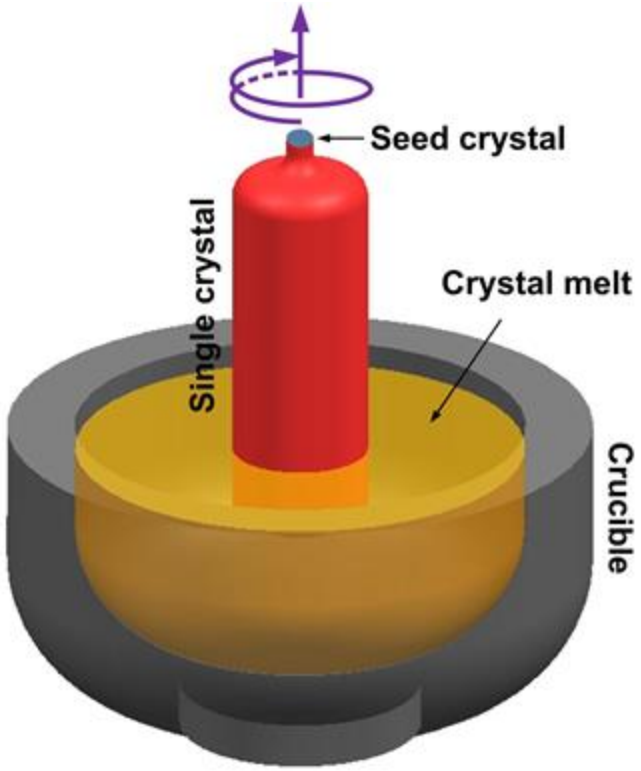

Figure 12. Diagram reproduced from [15]**. Diagram of the Czochralski process. Silicon Is heated in the crucible until molten, and then a high purity seed is dipped in the melt and slowly rotated while being pulled out to create a large single crystal.**

During the process the quartz crucible will gradually dissolve and release oxygen into the melt. While a large quantity of oxygen is removed as silicon monoxide gas, this still leaves the ingot with relatively high oxygen concentrations, typically in the range 10^{17} to 10^{18} cm^{-3}. The presence of the oxygen is very beneficial in manufacturing in that the oxygen gives the Cz silicon considerable strength against breakages

3.2. Float Zone Silicon

Float Zone (FZ) silicon is not generally used in large scale manufacturing of solar cells as it is an expensive method so is generally reserved for the electronics industry where the requirements for high purity silicon are more important. Figure 13 shows a typical float zone pulling process. The

process starts with a high purity polycrystalline rod of silicon with a seed with the desired orientation placed at the bottom.

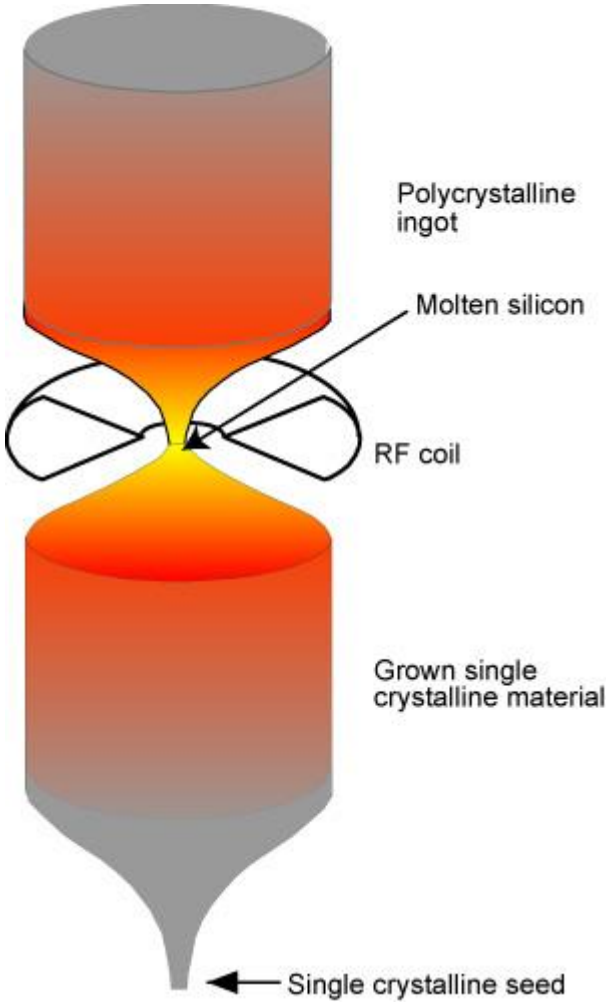

Figure 13. Diagram reproduced from [8]**. Diagram of the Float Zone process. A high purity poly silicon rod is placed on a seed, and then a RF coil is used to melt the polysilicon, removing defects and forming a single crystal.**

A radio frequency (RF) coil is then used to melt a small section of the polysilicon, starting at the bottom by the seed. The RF coil is then slowly moved up the rod and as the silicon solidifies it takes the crystal orientation of the seed, producing a single crystal. Also as the solubility of most impurities is higher in the liquid phase it purifies the rod as it goes along. This process can be repeated to

improve the purity of the ingot with concentrations of less than 10^{10} cm^{-3} achievable. The process does not require a crucible and is typically done in an argon atmosphere. This allows ingots with oxygen concentrations often below 10^{15} cm^{-3}. The main difference between FZ and Cz silicon is the oxygen concentration, making it a useful research tool to examine the effect of oxygen in Cz silicon.

3.3. Multi-crystalline Silicon

Multi-crystalline silicon is much cheaper to produce than FZ and Cz silicon and has the added advantage that it is not limited to circular wafers. A diagram of the process is shown in Figure 14. The feedstock is melted in a quartz crucible and then the heaters are slowly raised up the crucible creating a temperature gradient. The silicon will initially solidify at the bottom of the crucible and crystals will grow upwards providing there is a constant temperature gradient.

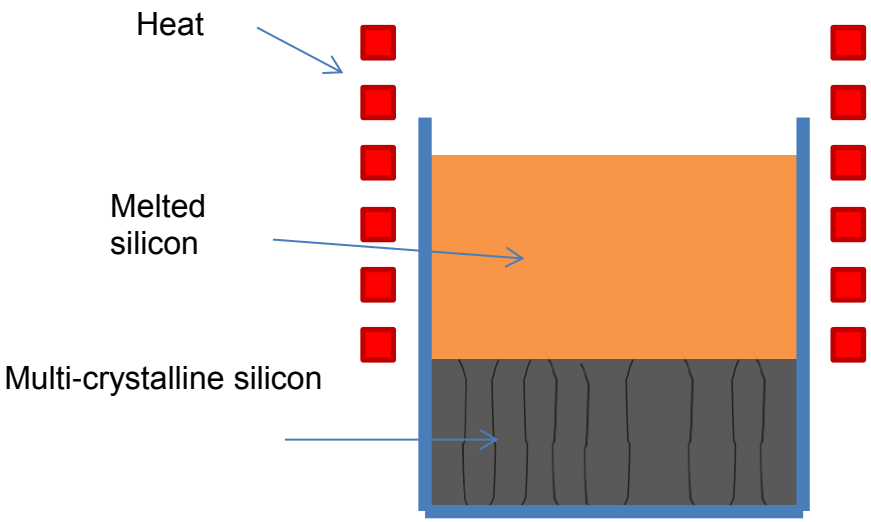

Figure 14. Diagram of the multi-crystalline process. Silicon is melted in a crucible and the heaters are slowly raised up the crucible so grow large crystals.

The growth rate is proportional to the temperature gradient difference between the solidified silicon and the liquid silicon. Metal impurities are segregated out to some extent to the top of the ingot in

multi-crystalline silicon. However there are typically far more metal impurities than in Cz or FZ silicon, with concentrations above 10^{13} not uncommon. There are also far more of other defects such as dislocations and grain boundaries which will also have an effect on the efficiency of multi-crystalline silicon.

3.4. Impurities in Silicon

In silicon there will typically be both desired and undesired impurities. Atoms such as boron or phosphorous are generally intentionally added to silicon to act as donors or acceptors. However as covered in the previous chapters, there will also be metallic impurities whichever way the silicon ingots are manufactured. In some cases these metallic impurities can be desirable, such as in certain power devices, but for solar cells and Integrated circuits (ICs) these impurities are normally highly undesirable. The effect of a lot of the most common metal impurities on silicon for PV was examined in what is known as the Westinghouse study [16]. In this study approximately 200 different Czochralski silicon ingots were grown, each with varying concentrations of different common impurity metals added in the melt, for both p-type and n-type silicon. The concentrations of the impurities in the ingots were measured using neutron activation analysis and spark source mass spectrometry. The ingots were cut into wafers and turned into solar cells, and the efficiency of the cells was measured. The results for p-type silicon are shown in Figure 15. The results show that even tiny concentrations of transition metals in silicon can have very large effects on solar efficiency. Having even as little as 1 part in a billion of impurity metals such as Ta, Mo, Nb, Zr, W, Ti and V can be seen to have a huge effect on solar efficiency.

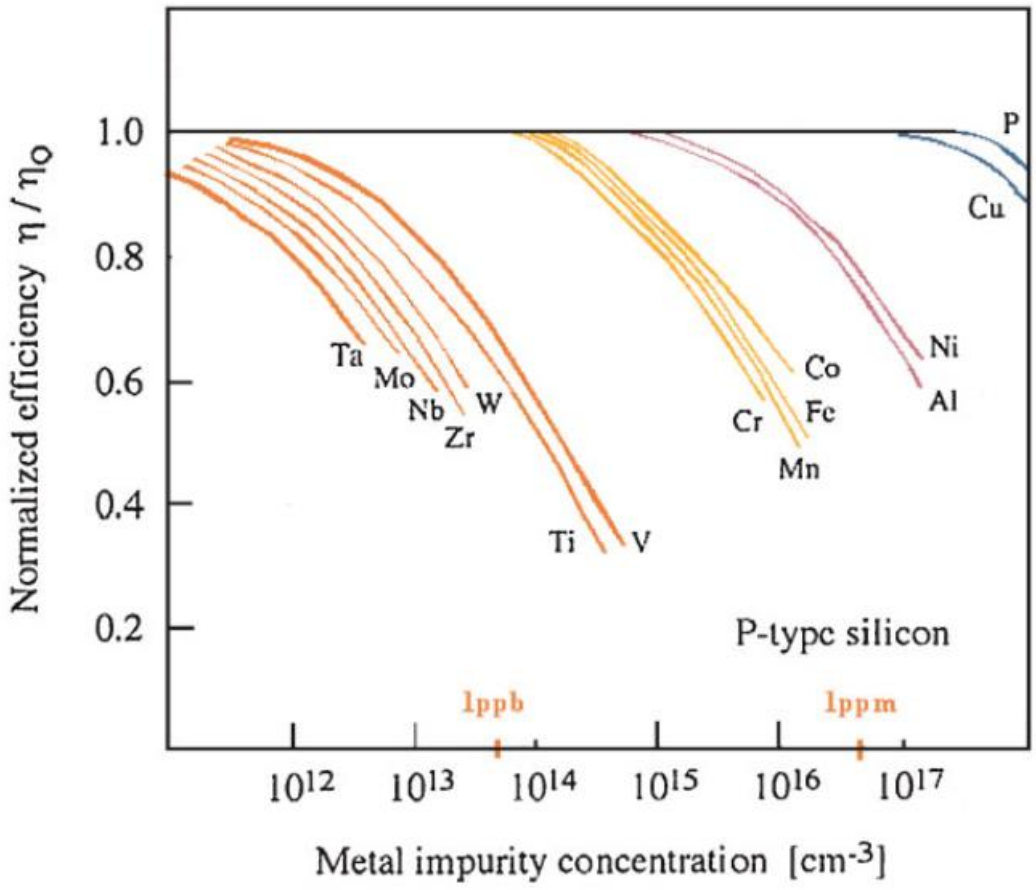

Figure 15. Data from[16]**, figure re-plotted in colour by**[14]**. Graph shows the effect of the concentration of metallic impurities in Czochralski silicon on the normalized efficiency of the solar cells.**

Impurity metals in silicon will tend to either be single point defects within the crystal, or form precipitates with other impurity metals. Whether the atoms will form precipitates or be point defects depends on the impurity atoms solubility, diffusivity and concentration with-in the ingot. Impurity metals with a high diffusivity and solubility are more likely to form precipitates, especially during heating processes with slow cooling times. When silicon is heated, the solubility and diffusivity of the impurity metals is increased, allowing them to diffuse more freely through the silicon. Upon cooling the solubility will decrease and the metal impurities will clump together and form precipitates. Figure 16 shows the diffusivity and solubility of the 3d transition metals at 1100 ^{o}C. It can clearly be seen that the metals with a higher solubility and diffusivity are also the metals

which tend to have the least negative effect on the efficiency of the solar cells shown in Figure 15. One reason for this is because a higher percentage of these elements will be in precipitates, which tend to have a smaller effect on solar cell efficiency due to having fewer recombination centers than if they were dispersed point defects.

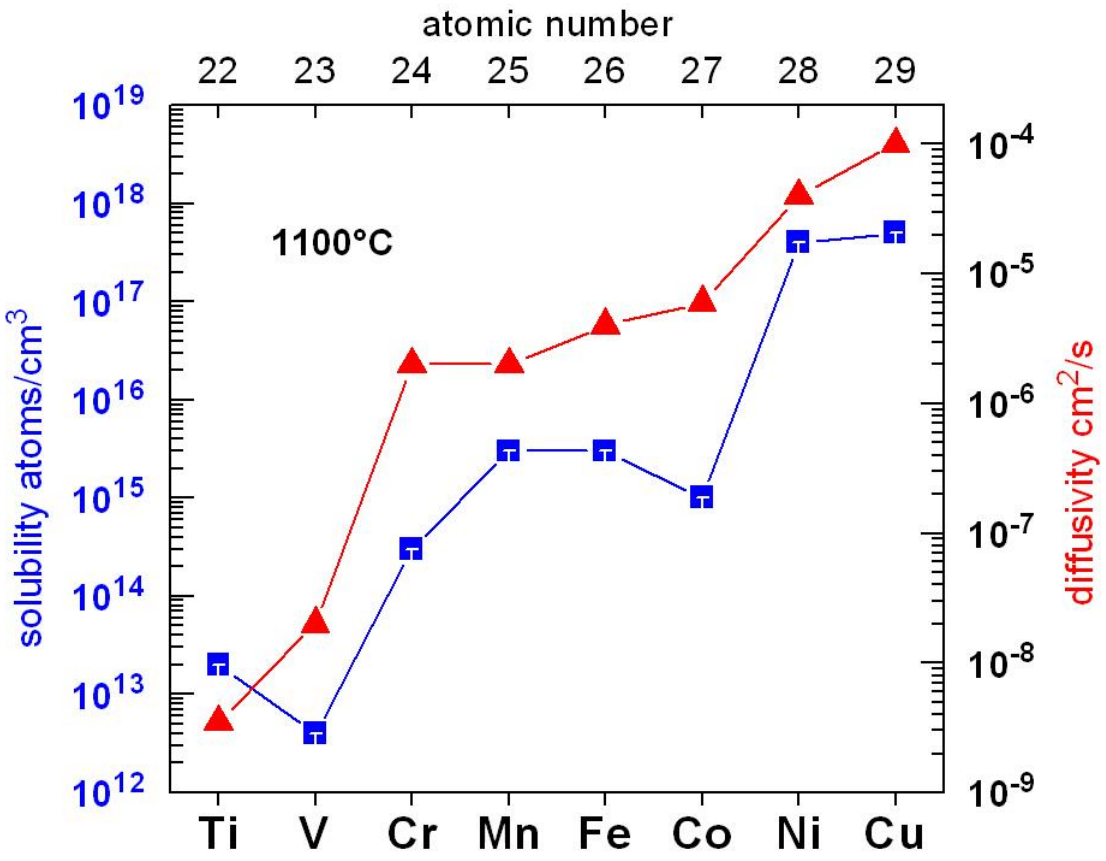

Figure 16. Reproduced from [17]**. Solubility (blue squares) and diffusivity (red triangles) of the 3d transition metals at 1100 °C. They are plotted in order of their atomic number.**

3.5. Recombination in Silicon

Recombination occurs when an electron from the conduction band (CB) transitions to the valence band (VB) thereby also eliminating a valence band hole. There are three main types of recombination mechanism, commonly known as: Auger, Radiative and Shockley-Read-Hall (SRH) recombination and their mechanisms are represented in Figure 17. Radiative (or band to band) recombination occurs when an electron drops from the CB to the VB emitting a photon (hence radiative) in the process and is the basic principle of how a Light Emitting Diode (LED) works. However this is far more likely to happen in direct band gap semiconductors than indirect semiconductors due to the difference in electron and hole momentum in indirect semiconductors. As silicon is an indirect semiconductor this process can only happen with phonon assistance and therefore is usually neglected in calculations due to the prominence of other recombination processes.

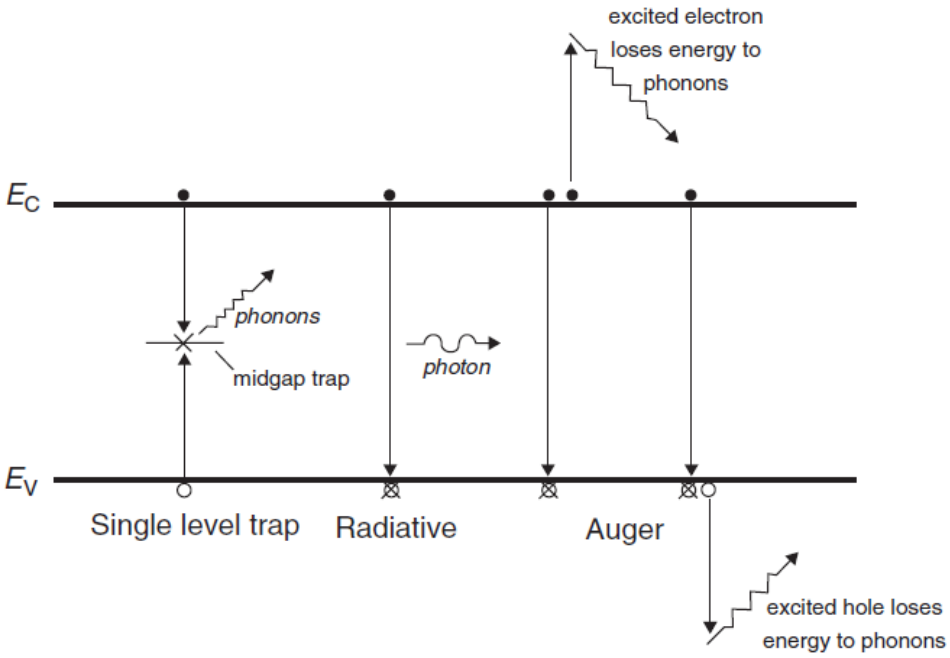

Figure 17. reproduced from [9]**. Energy band diagram showing SRH (single level trap), radiative and Auger recombination.**

Auger recombination occurs when an electron falls to the VB, but instead of releasing a photon, it gives its energy to either an electron in the conduction band or a hole in the valence band. This excited carrier will then thermally relax releasing its excess energy as phonons. This process is especially important in high injection circumstances, such as concentrator solar cells, and does limit the carrier lifetime of solar cells.

SRH recombination is caused by defects, such as metal impurities and is generally considered to be the type of recombination which effects the carrier lifetime the most. It is a two-step process, where electrons from the conduction band or holes from the valence band are trapped in a mid-gap energy state caused by a defect. Once the electron (hole) is trapped at this state, it can then either be re-emitted to the CB (VB) or it can be thermally emitted to the VB (CB) and recombine. This recombination is far more likely to happen than radiative recombination, as the energy barrier to a mid-gap trap will be less than from the CB to the VB.

3.6. Electrical Properties of Impurity Atoms

Different defects will have different electrical properties depending on various factors, such as their size, atomic location and chemical structure. Point defects are the most well understood type of defect and typically the most common in crystalline silicon. Dopant atoms will introduce shallow levels which have very little effect on solar cell efficiency as shallow levels tend only to trap carriers and not to lead to recombination. Metallic impurities however often lead to deep levels which can be strong recombination centers. Figure 18 shows an energy band diagram outlining how the recombination process occurs at a deep level, as well as the trapping process which is more common at shallow levels. Defects can be either electrically active, when they have states in the band gap, or electrically inactive if they don't form states in the band gap. An electrically active defect will either be a donor state or an acceptor state. If the state is positive when it is empty but neutral when it accepts an electron it is known as a donor state. If the state is neutral when empty and positive

when filled by an electron it is called an acceptor [18]. Double donor and double acceptor states are also possible if two charge carriers are accepted to the same defect.

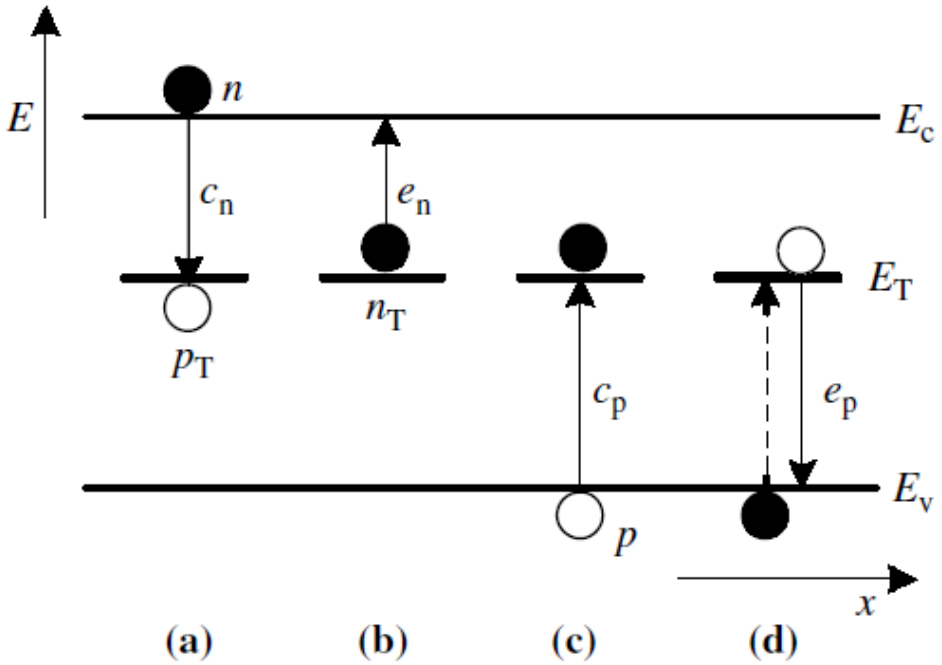

Figure 18. Reproduced from [9]**. Energy band diagram showing the stages of recombination. If an electron is trapped by a centre (a) but then re-emitted to the conduction band (b), recombination will not take place. Similarly recombination will not take place if a hole is trapped at a centre (c) followed by the hole being re-emitted to the valence band (d). However if an electron is trapped by a defect (a) and also a hole to the defect (c), recombination will happen. Similarly if (d) is followed by (b) recombination will also occur.**

The state of the defect will have a large effect on the minority carrier capture cross section. The capture cross section describes the effectiveness of a defect to capture carriers, and depends on the potential around the defect. The minority carrier capture cross section will be much bigger if there is Coulombic attraction between either a hole and a defect with a negative charge state or an electron and a defect with a positive charge state.

4. Schottky Diodes and Experimental Techniques

In this chapter the main techniques used for the work carried out in this thesis will be explained. The majority of work undertaken in this thesis was electrical measurements carried out on Schottky diodes. A Schottky diode is created when a metal contact is evaporated onto the surface of a semiconductor and a potential barrier is formed at the metal-semiconductor interface. The theory was first introduced by Schottky in 1942 [19]. For simplicity everything in this chapter will be describing n-type silicon. The energy diagram for the formation of a Schottky contact is shown in Figure 19. When the metal and semiconductor are initially placed into contact the Fermi levels of the metal and the semiconductor will not be lined up, causing electrons to flow from the semiconductor to the metal. The electrons will leave behind a positive donor charge, causing an energy barrier and a depletion region as the Fermi levels will line up between the semiconductor and the metal. The diode will reach equilibrium as the number of electrons jumping from the metal to the semiconductor will be the same as from the semiconductor to the metal. In reality a thin oxide layer will grow on the silicon, preventing a perfect contact between the metal and the semiconductor. However if processed correctly this will be thin enough so that electrons can tunnel through and will have a minimal effect.

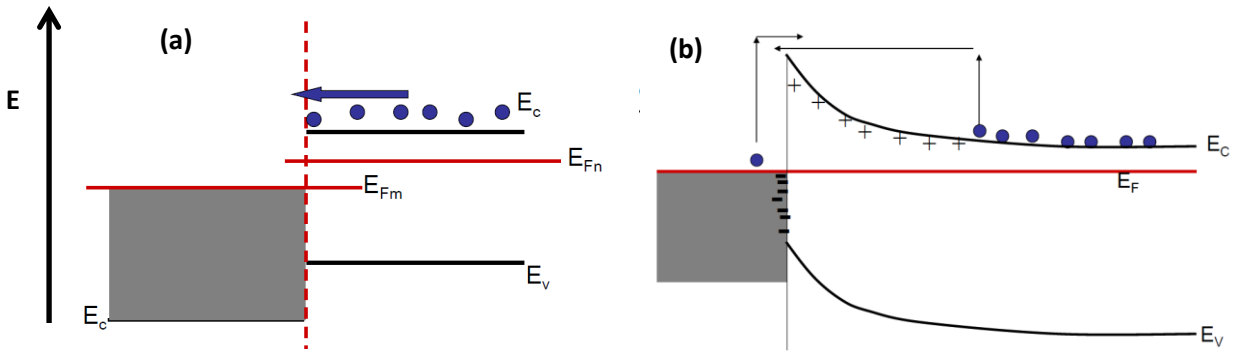

Figure 19. Energy band diagrams of a metal semiconductor contact before (a) and after contact (b). A Schottky diode is formed in (b) as electrons flow from the semiconductor to the metal, leaving behind a depleted region and an electric field due to remaining positive donor ions.

To produce the Schottky diodes, 1 mm diameter circular dots were evaporated or sputtered onto the silicon using either gold (n-type silicon) or titanium (p-type silicon). Ohmic contacts were then evaporated on to the backside of the silicon using aluminum (n-type) or gold (p-type). The diodes were then put onto a substrate using silver paint and a gold wire bonder was used to attach the Schottky diode to the substrate. A diagram of a typical Schottky diode used in this thesis is shown in Figure 20.

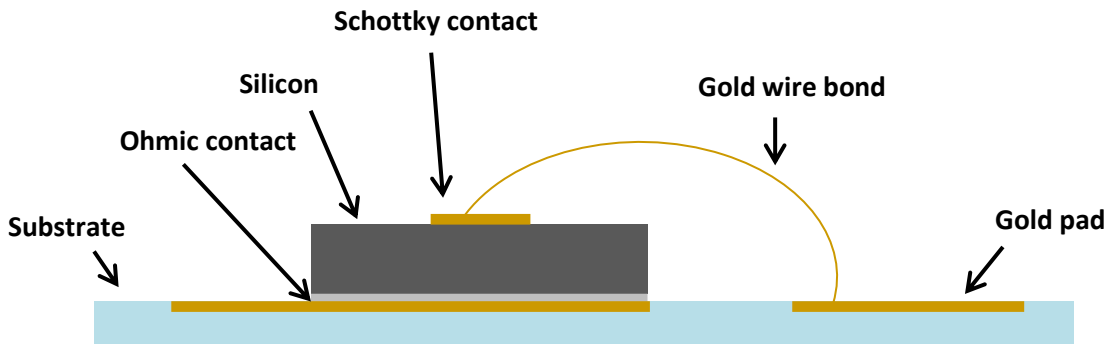

Figure 20. Side view diagram of typical silicon Schottky diode sample on a gold padded ceramic substrate.

If a forward bias is applied to the diode the Fermi level of the semiconductor will be raised compared to the metal. This will reduce the height of the potential barrier and cause a flow of electrons from the semiconductor to the metal. However if a reverse bias is applied to the diode, the Fermi level of the semiconductor will be lowered compared to the metal. This will cause the potential barrier to be increased for electrons in the semiconductor but not for electrons in the metal in an ideal Schottky diode, causing the depletion region to increase in size. However this means the current will not increase across the diode until a certain limit is reached where dielectric breakdown of the semiconductor occurs.

By solving Poisson's equations the electric field potentials and widths can be calculated. The boundary conditions can be obtained from the barrier height and the fact that the electric field in

the bulk can be assumed to be 0. Therefore they can be written as V(0) = Vd and E(∞) = 0. For a layer of metal on a semiconductor we can consider it in one dimension so Poisson's equation can be written as:

$$\frac{d^2V}{dx^2} = \frac{1}{\varepsilon}p(x) \tag{1}$$

where p(x) is the total charge density in the semiconductor at a depth x, and ε is the permittivity of the material. For simplicity the depletion approximation is used which divides the semiconductor into two regions, the bulk, and the depletion region. It assumes that no electric field exists in the bulk and that the depletion region has no free carriers. Therefore in the depletion region where $x \leq w$, $p(x) = qN_D$ where q is the charge of an electron, N_D is the donor concentration and w is the depletion width. In the bulk, $x \geq w$, $p(x) = 0$. Therefore by integrating equation (1) twice with respect to the boundary conditions the width of the depletion region will be:

$$w = \sqrt{\frac{2\varepsilon V_d}{qN_D}} \tag{2}$$

the electric field can be given by:

$$E(x) = -\frac{qN_D(w-x)}{\varepsilon} \tag{3}$$

and the potential in the depletion region is:

$$V(x) = -\frac{qN_D}{2\varepsilon}(w-x)^2 \tag{4}$$

The charge per unit area in the depletion region is:

$$Q_D = qwN_D = \sqrt{2q\varepsilon N_D V_d} \tag{5}$$

therefore the capacitance per unit area of the diode can be written as:

$$C = \frac{dQ_D}{dV_d} = \sqrt{\frac{\varepsilon q N_D}{2V_d}} = \frac{\varepsilon}{w} \quad (6)$$

In reality the assumption used in the depletion approximation that there are no free carriers in the depletion is not correct. There will be a small region which is only partly depleted of free carriers in what is known as the Debye tail. The Debye tail length is given by:

$$L_D = \sqrt{\frac{\varepsilon k_B T}{q^2 N_D}} \quad (7)$$

where k_B is the Boltzmann constant and T is temperature.

4.1. Current Voltage Measurements and Capacitance Voltage

Current Voltage (IV) measurements were undertaken on all samples to check the quality of the Ohmic contacts and Schottky diodes. The voltage was typically scanned from -10 V to 1 V in 0.1 V steps using a Hewlett Packard 4140B IV meter, and an IV curves were plotted. Schottky diodes typically had saturation currents in the range 10^{-5} – 10^{-7} A at room temperature.

Capacitance Voltage (CV) measurements were then undertaken on the best diodes to observe the spatial distribution of active dopants with in the space charge region. The capacitance is measured by applying a bias and then superimposing a small oscillating voltage. The current due to this oscillating voltage is then measured and the capacitance is calculated from

$$C = \frac{\Delta Q}{\Delta V} \quad (8)$$

The width of the depletion region can then be calculated from equation (6) and the donor concentration from equation (2). The CV measurements were carried out using a Hewlett Packard

4192B typically between -10 V to 0 V with the frequency of the AC voltage at 1 MHz and the amplitude at 0.05 V.

4.2. Deep Level Transient Spectroscopy

Deep Level Transient Spectroscopy (DLTS) is a capacitance transient thermal scanning method which can be used to measure and characterize defects in a semiconductor. The technique in the form that it is mostly widely used now was first implemented by Lang in 1974 and requires a cryostat, a voltage source and a capacitance meter [20]. Either a Schottky diode or p-n junction can be measured, but for the work in this thesis a Schottky diode was always used. A Schottky diode is typically cooled down to ~30K and is then put in reverse bias. The reverse bias is then reduced or completely removed in what is known as a filling pulse. At this stage the space charge region of the diode will be filled with either electrons (n-type) or holes (p-type). If there are electrically active defects, such as those from impurity metals, they will act as traps for the carriers if they are below the Fermi level. The reverse bias will then be re-applied and the electrons or holes will be re-emitted from the traps if they are above the Fermi Level. This emission of carriers will change the capacitance of the diode, and therefore can be measured to a very high degree of accuracy with a capacitance meter. A transient of the capacitance change over time can then be recorded, and the change in capacitance is related to the trap concentration with in the scanned area. A diagram showing how the bias is changed and the effect this has on the capacitance is shown in Figure 21.

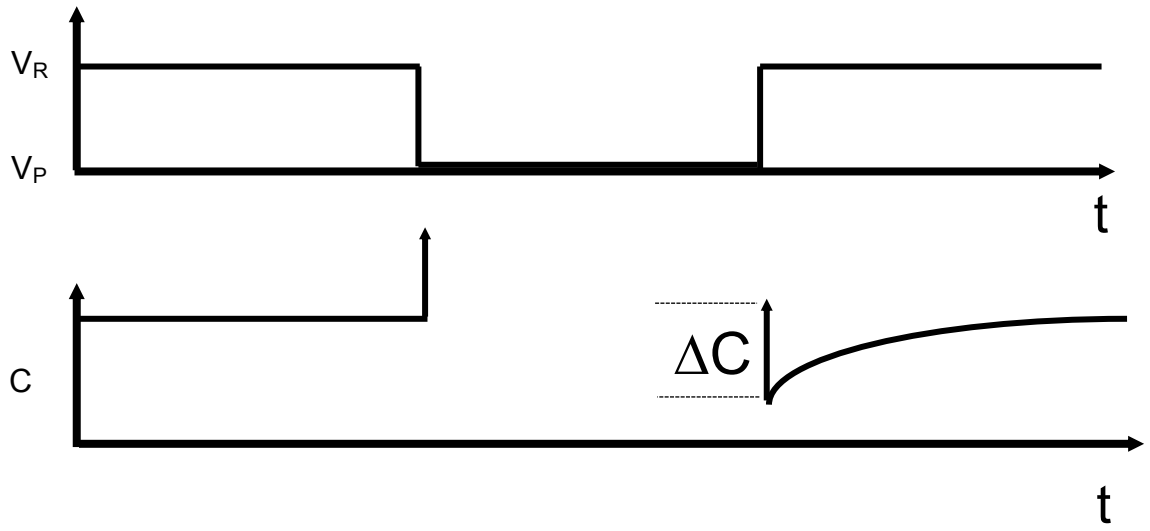

Figure 21. Diagram showing how the bias is varied over time in a typical DLTS measurement, and what effect this has on the diodes capacitance.

The emission rate of the carriers from the traps is strongly dependent on temperature, as an increase in temperature will change the position of the Fermi level and increase the emission rate. So by scanning the temperature, the emission rate from different traps will change. By setting an emission rate window, where only transients are recorded with emission rates within this window, traps with different energy levels can be observed at different temperatures. By changing the values of the reverse bias and filling pulse, the width of the space charge region will change according to equation (2). This means that it is possible to scan at different depths in the space charge region by using different biases.

By combining results taken from CV measurements and DLTS measurements it is possible to calculate the approximate concentrations of traps within the measurement region as:

$$N_T = \frac{2\Delta C N_D}{C_0} \tag{9}$$

where N_T is concentration of traps, C_0 is capacitance at bias and ΔC is change in capacitance in the transient rate window. However as a trap closer to the surface of a semiconductor will have more effect on the capacitance than a trap further away the following correction factor is used:

$$f = \frac{{W_B}^2}{({W_B}^2 - {W_P}^2)} \tag{10}$$

where W_B is depletion width at bias and, W_P is depletion width at pulse. Therefore the concentration of traps is normally calculated as:

$$N_T = \frac{2\Delta C N_D {W_B}^2}{C_0({W_B}^2 - {W_P}^2)} \tag{11}$$

DLTS is one of the most sensitive detection techniques in semiconductors and has a detection limit of ~10^5 less than then the carrier concentration of the semiconductor. Either a Boonton S4910 capacitance meter, or a meter specially designed for DLTS at the University of Manchester Institute of Science and Technology (UMIST) were used in this work. The bias was controlled with a UMIST card.

4.3. Laplace DLTS

One drawback of DLTS is that peaks tend to be very broad and that the time constant resolution is not good enough to study fine structure in the emission process. Therefore if there are two or more defects, with similar emission rates it is often not possible to resolve them using conventional DLTS. To overcome this, a technique known as Laplace DLTS (LDLTS) was developed which uses an algorithm that effectively performs an inverse Laplace transform on the DLTS transients. This has shown that the resolution can be improved by orders of magnitude compared to conventional DLTS [21]. Instead of scanning the temperature, a transient is taken at a fixed temperature and up to

three mathematical routines based on the Tikhonov regularization method are performed on the transient. These routines are CONTIN [22], a modified version of FTIKREG [23] and FLOG which was specifically designed for LDLTS by A. Matulis. Using 2 or more of the algorithms is common practice throughout the work carried out in this thesis to increase the level of confidence in the resultant spectra. Figure 22 shows the DLTS and LDLTS spectra of hydrogenated silicon containing gold by from a paper by Deixler et al [24]. The inset shows the DLTS spectrum and only one broad peak can be seen. However using LDLTS it can clearly be seen that there are two peaks, one attributed to electron emission from the gold acceptor and the other to a gold-hydrogen level (G4).

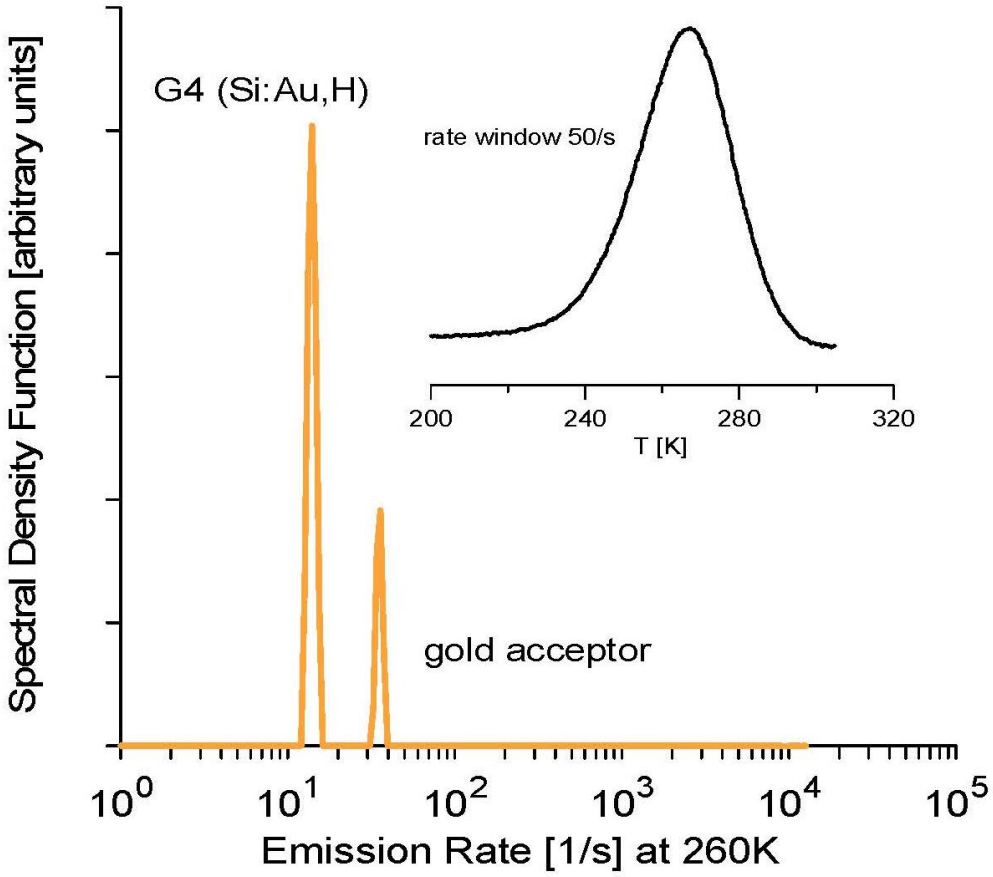

Figure 22. Reproduced from [24]**. LDLTS peaks and (inset) DLTS peaks of the same gold defect in silicon. Using LDLTS it is possible to resolve two peaks, whereas only one broad peak is seen in DLTS.**

4.4. Minority Carrier Transient Spectroscopy

Another limitation to DLTS is that it only measures majority carrier capture and emission process, and for solar cells the effect of minority carriers is of far more importance. However by using an above band gap LED for backside illumination of a Schottky diode, a pure minority carrier flux can be achieved. The technique was first used to observe centers in Gallium Phosphide in 1979 by Hamilton et al [25]. In a typical Minority Carrier Transient Spectroscopy (MCTS) scan, the diode will be held at a constant reverse bias, depending on the depth of the sample that is to be examined. Then instead of an electrical pulse to fill the space charge region with majority carriers, an LED pulse is used to fill it with minority carriers. For this to be effective, the minority carrier diffusion length needs to be greater than the thickness of the wafer or the majority of the minority carriers will recombine before they reach the space charge region. When the LED pulse is removed the minority carriers will be emitted from the traps if the traps are above the Fermi level position, resulting in a negative transient. A diagram showing how the LED effects the capacitance in this process is shown in Figure 23.

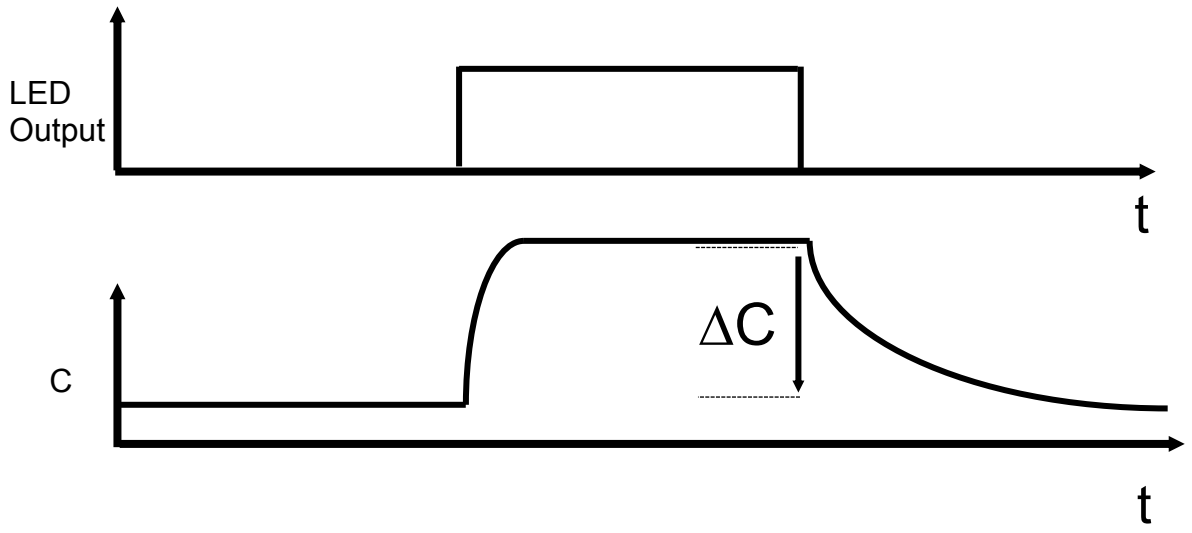

Figure 23. Diagram showing how the LED is operated over time in a typical MCTS measurement, and what effect this has on the diodes capacitance.

To test the minority carrier flux, the photocurrent of the diode when illuminated is measured. In samples where either the sample is too thick or the minority carrier lifetime is too low, front side illumination from a near band gap LED with semi-transparent Schottky diodes can be used. However there is a slight disadvantage as front side illumination will also generate some majority carriers.

4.5. DLTS and LDLTS Characterization Techniques

DLTS or LDLTS can be used to characterize traps by calculating their energy level with in the band gap and their capture cross section. The position of a defect with-in the band gap is determined by looking at the thermal activation of the emission process. This was typically done with LDLTS by measuring the emission rate at several temperatures around the position of the peak measured in conventional DLTS. The activation energy, E_A, and pre exponential factor, A, can then be determined from an Arrhenius plot of $\ln(e_n/ T^2)$ as a function of 1/kT. The apparent capture cross section can then be calculated from the pre exponential factor as

$$e_n(T) = \sigma_n v_n N_D \exp(-\frac{E_A}{kT}) \tag{12}$$

where σ_n is the apparent capture cross section and v_n is the thermal velocity for electrons. Therefore the apparent capture cross section is

$$\sigma_n = \frac{A}{v_n N_D} \tag{13}$$

However measuring the apparent capture cross section does not take the temperature dependence of the trap into account. To measure the true capture cross section at a certain temperature, the filling pulse width (t_p) is varied and the magnitude of the transient is measured using LDLTS at each filling pulse width. As the filling pulse width is reduced, this will cause incomplete filling of the traps

and a reduction in LDLTS signal. Plotting LDLTS signal (L) by t_p will typically give a monoexponential curve for most point defects and be fitted using the following function:

$$L(t_p) = C_0 + \Delta C\left(1 - \exp\left(-c_n t_p\right)\right) \quad (14)$$

where C_0 is the LDLTS signal at the lower saturation point, ΔC is the change in LDLTS signal from complete filling to C_0 and c_n is the capture rate. The true capture cross section can then be calculated from the following equation:

$$c_n = \sigma_n v_n N_D \quad (15)$$

4.6. Secondary Ion Mass Spectroscopy

Secondary Ion Mass Spectroscopy (SIMS) is a technique which can determine the elemental composition of a surface using an ion beam. Using a combination of SIMS and DLTS can give invaluable information about the electrical and spatial properties of metal impurities in silicon. Using DLTS by itself it is can be difficult to know if a reduction in the size of peak related to a metal impurity is caused by electrical passivation, or by out diffusion or some other reason. The use of SIMS can give a spatial distribution of elements within the semiconductor, and when compared with electrical measurements from DLTS allows much better understanding of how metallic impurities are behaving.

The technique works by bombarding a surface with an energetic beam of primary ions. This will cause a mixture of secondary ions to be emitted from the targets surface. These secondary ions are then analyzed in a mass spectrometer. In order to be able to do this accurately the expected molecular mass of the ions is needed so that the mass spectrometer can be set up to detect these ions. As the mass spectrometer will only determine the molecular weight of an element,

inaccuracies can arise if certain molecules happen to have the same molecular weight as the element of interest. The ion count on the detector of the mass spectrometer will be recorded as a function of the primary ion beam sputtering time. By comparing the ion count to a calibration sample ion count with a known concentration of the element it is possible to determine the concentration of the element. Similarly the depth is calculated according to the sputter time. The detection limit of SIMS varies with the element being examined, depending on their abundance with-in the measurement system. For common elements such as Fe or H it is typically around 10^{15} cm^{-3}, whereas for less common impurities such as Ti or Mo it is around 10^{14} cm^{-3}.

4.7. Transmission Electron Microscopy and Analytical Techniques

Transmission Electron Microscopy (TEM) is a microscopy technique that transmits a beam of electrons through an ultra-thin sample, generally around 50 nm. The technique was first demonstrated by Knoll and Ruska in 1931. The electron beam will interact with the sample as it passes through, and the sample will typically emit a range of different signals, including bright field, dark field, backscattered electrons, secondary electrons, energy-loss electrons and x-rays [26]. The bright field image typically refers to the image collated on the detector due to a beam that has been transmitted through the sample, whereas the dark field is made up of a diffracted beam. The properties of the sample, such as density and composition will determine how the electron beam behaves through the sample. This technique is particularly useful for observing precipitates with in silicon. Modern day systems tend to be scanning transmission electron microscopes (STEMs) with resolutions down to the molecular scale and also have further analysis tools which can prove invaluable for determining the presence and composition of precipitates. In particular, by looking at high angle Rutherford scattered electrons, it is possible to obtain an image that has far greater compositional contrast than a typical TEM or x-ray image [27]. This technique is known as High Angle

Annular Dark Field (HAADF) imaging. Once an area with different composition has been found using HAADF imaging it is possible to determine what the composition might be using energy dispersive X-ray (EDX) measurements. As different elements have unique atomic structures, when the sample is scanned with an electron beam, characteristic x-rays can be collimated and detected. The energy of the collected electrons can be compared to calibration values, and the chemical structure of the sample can then be deduced at the nano-meter scale.

5. Significance of Work in Thesis

The papers presented in this thesis all investigate the effect of metallic impurities in silicon using the techniques discussed in the previous chapters. Three different transition metals have been studied: Ti, Mo, and Fe. Ti and Mo were chosen as they are particularly hard to getter due to their low diffusivity [28] and are also more likely to form precipitates. Fe was chosen as it is one of the most common impurities in silicon and is a strong recombination center with a very detrimental effect to solar cell performance [29].

Chapters 7 and 9 focus on the reaction of hydrogen with Ti and Fe respectively in the silicon lattice. This is an important topic as hydrogen is known to passivate some defects [30] and is incorporated into silicon in solar cell manufacturing when the silicon nitride anti reflection coating is deposited. If it is energetically favourable, hydrogen will form complexes with transition metals. This will change the electronic properties of the transition metal, and in some cases can make them electrically inactive, where they no longer have any levels in the band gap. This means the transition metal will no longer act as a recombination centre and is “passivated”. If this can be easily achieved it is obviously very desirable for solar cell performance.

There are different techniques, such as gettering, which also reduce the electrical activity of metal defects, and one such technique is discussed in chapter 8. By creating vacancies with ion implantation, it is possible to move metal impurities from interstitial to substitutional lattice sites. This will similarly change the electronic properties of the defects, and in the case of Ti, was seen to change the defect from a strong recombination centre into an electrically inactive defect. It was only possible to confirm this process using a combination of DLTS and SIMS. This is due to it not being clear what was the reason was for the electrical disappearance of the Ti signals in DLTS. The use of SIMS can confirm that the Ti still remains, and hasn’t out diffused, which shows the importance of using different techniques to analyse the samples. Similarly by using both FZ and Cz samples we learnt more about the process. The gettering was observed to be far more prominent in FZ silicon,

with the reason being the extra oxygen in Cz silicon forms vacancy-oxygen complexes which prevent the Ti from moving to the substitutional lattice site.

Finally chapters 9 and 10 focus on the topic of nano-precipitates in silicon. This is a topic of research that has had very little attention until this work, and may be of crucial significance to understanding the efficiency gap between lower purity cast silicon and high quality single crystalline silicon. By using a combination of DLTS, and TEM we have managed to both electrically and physically observe molybdenum nano-precipitates in the range of 2-10 nm. These nano-precipitates have been studied using LDLTS and MCTS, as well as being extensively modelled and have very interesting electronic behavior. They have very large minority carrier capture cross sections and mid gap energy levels, making them very strong recombination centres. The nano-precipitates represent a new class of recombination centre and it is likely that they will also form from other slow diffusing transition metals, making them a very important topic of research.

References

[1] "Fraunhofer Institute for Solar Energy Systems, Levelized Cost of Electricity Renewable Energy Technologies," no. November, 2013.

[2] "International Energy Agency Technology Roadmap, Solar Photolvotaic Energy," 2014.

[3] R. M. Swanson, "A Vision for Crystalline Silicon Photovoltaics," Prog. Photovolt Res. Appl., vol. 14, pp. 443–453, 2006.

[4] "International Technology Roadmap for Photovoltaics," 2015.

[5] C. Huhne, C. Jones, A. Foster, and F. Ewing, "UK Renewable Energy Roadmap, Department of Climate Change," 2011.

[6] "Department of Energy and Climate Change, Feed-in-Tariff scheme October 2007 – October 2011," pp. 1–18, 2011.

[7] M. a. Green, "The Passivated Emitter and Rear Cell (PERC): From conception to mass production," Sol. Energy Mater. Sol. Cells, vol. 143, pp. 190–197, Dec. 2015.

[8] C. Honsberg and S. Bowden, "PV Education," http://pveducation.org/pvcdrom/pn-junction/doping. .

[9] A. Luque and S. Hegedus, Photovoltaic Science Handbook of Photovoltaic Science. 2011.

[10] M. A. Green, K. Emery, Y. Hishikawa, W. Warta, and E. D. Dunlop, "Solar cell efficiency tables (version 46)," no. version 46, pp. 805–812, 2015.

[11] M. a. Green, A. Ho-Baillie, and H. J. Snaith, "The emergence of perovskite solar cells," Nat. Photonics, vol. 8, no. 7, pp. 506–514, Jun. 2014.

[12] C. Richard, V. Reed, L. Putnam, A. Brown, J. Cochran, P. Denholm, D. Feldman, B. Hannegan, J. Logan, M. Mann, D. Mooney, R. Newmark, M. Pacheco, G. Porro, P. Schwabe, and K. Wipke, "NREL Renewable Energy Data Book," 2013.

[13] J. Safarian, G. Tranell, and M. Tangstad, "Processes for Upgrading Metallurgical Grade Silicon to Solar Grade Silicon," Energy Procedia, vol. 20, no. 1876, pp. 88–97, 2012.

[14] S. Pizzini, "Bulk solar grade silicon: how chemistry and physics play to get a benevolent microstructured material," Appl. Phys. A, vol. 96, no. 1, pp. 171–188, Jan. 2009.

[15] J. Lu and J. Miao, "Growth mechanism of carbon nanotubes: a nano Czochralski model.," Nanoscale Res. Lett., vol. 7, no. 1, p. 356, Jan. 2012.

[16] J. R. Davis, A. Rohatgi, R. H. Hopkins, P. D. Blais, P. Rai-Choudhury, J. R. McCormick, and H. C. Mollenkopf, "Impurities in Silicon Solar Cells," IEEE Trans. Electron Devices, vol. 27, no. 4, p. 677, 1980.

[17] A. R. Peaker, V. P. Markevich, B. Hamilton, G. Parada, A. Dudas, A. Pap, E. Don, B. Lim, J. Schmidt, L. Yu, Y. Yoon, and G. Rozgonyi, “Recombination via point defects and their complexes in solar silicon,” Phys. Stat. Sol. A, vol. 209, no. 10, pp. 1884–1893, Oct. 2012.

[18] M. Jaros, “Deep levels in semiconductors,” Adv. Phys., vol. 29, no. 3, pp. 409–525, Jul. 2006.

[19] V. W. Schottky, “Simplified and advanced theory of boundary layer rectifier,” , vol. 539, pp. 539–592, 1941.

[20] D. V. Lang, “Deep-level transient spectroscopy: A new method to characterize traps in semiconductors,” J. Appl. Phys., vol. 45, no. 7, p. 3023, 1974.

[21] L. Dobaczewski, P. Kaczor, I. D. Hawkins, and a. R. Peaker, “Laplace transform deep-level transient spectroscopic studies of defects in semiconductors,” J. Appl. Phys., vol. 76, no. 1, p. 194, 1994.

[22] S. W. Provencher, “A Constrained Regularization Method For Inverting Data Represented by Linear Algebraic or Integral Equations,” Comput. Phys. Commun., vol. 27, pp. 213–227, 1982.

[23] J. Weese, “A reliable and fast method for the solution of Fredholm integral equations of the first kind based on Tikhonov regularization,” Comput. Phys. Commun., vol. 69, pp. 99–111, 1992.

[24] P. Deixler, J. Terry, I. D. Hawkins, J. H. Evans-Freeman, a. R. Peaker, L. Rubaldo, D. K. Maude, J.-C. Portal, L. Dobaczewski, K. Bonde Nielsen, a. Nylandsted Larsen, and a. Mesli, “Laplace-transform deep-level transient spectroscopy studies of the G4 gold–hydrogen complex in silicon,” Appl. Phys. Lett., vol. 73, no. 21, p. 3126, 1998.

[25] B. Hamilton, a. R. Peaker, and D. R. Wight, “Deep-state-controlled minority-carrier lifetime in n-type gallium phosphide,” J. Appl. Phys., vol. 50, no. 10, p. 6373, 1979.

[26] M. A. X. T. Otten, “High-Angle Annular Dark-Field Imaging on a TEM / STEM System,” J. Electron Microsc. Tech., vol. 230, pp. 221–230, 1991.

[27] S. J. Pennycook and J. Narayan, “Direct imaging of dopant distributions in silicon by scanning transmission electron microscopy,” Appl. Phys. Lett., vol. 45, no. 4, p. 385, 1984.

[28] S. M. Myers, M. Seibt, and W. Schröter, “Mechanisms of transition-metal gettering in silicon,” J. Appl. Phys., vol. 88, no. 7, p. 3795, 2000.

[29] A. A. Istratov, H. Hieslmair, and E. R. Weber, “Iron and its complexes in silicon,” Appl. Phys. A, vol. 69, pp. 13–44, 1999.

[30] G. W. Trucks, K. Raghavachari, G. S. Higashi, and Y. J. Chabal, “Mechanism of HF Etching of Silicon Surfaces: A Theoretical Understanding of Hydrogen Passivation,” Phys. Rev. Lett., vol. 65, no. 4, pp. 504–507, 1990.

Paper 1

Passivation of titanium by hydrogen in silicon

S. Leonard, V. P. Markevich, A. R. Peaker, and B. Hamilton

Appl. Phys. Lett., vol. 103, no. 13, p. 132103, 2013.

6. Passivation of titanium by hydrogen in silicon

6.1.Abstract

Interactions of hydrogen with titanium have been studied in Ti-doped n-type crystalline Si using capacitance-voltage profiling and deep level transient spectroscopy (DLTS). Hydrogen plasma treatments of the samples at room temperature have resulted in the suppression of DLTS signals due to interstitial Ti atoms (Ti_i) and the appearance of three strong DLTS peaks which are related to three different Ti-H defects. After annealing of the hydrogenated samples at 150 ^oC in nitrogen the signals due to Ti_i and two of the three H-related defects were not detected in the spectra showing that almost complete passivation of all electrically active defects occurred.

6.2.Introduction

Titanium (Ti) is a common impurity in solar grade silicon which is seen in both multi-crystalline and mono-cast material. Ti acts as a strong recombination centre in silicon, which reduces carrier lifetime and solar cells efficiency [1]. Ti atoms normally reside at tetrahedral interstitial sites [2] and being at this position give rise to a double donor level at E_V +0.28 eV, a donor level at E_C – 0.27 eV and an acceptor level at E_C – 0.08 eV [3].

Ti is known to be a slow diffuser in silicon, [4]-[5] which makes it very difficult to getter [1]. Hydrogen on the other hand is a very fast diffuser in silicon and is commonly used in Si-based photovoltaic cells to passivate recombination active defects. Hydrogen is usually introduced into the cells from silicon nitride anti-reflective coatings during high-temperature manufacturing steps [6]. However, it is not fully understood what defects are effectively passivated with hydrogen. Previous studies on the passivation of Ti with hydrogen have had conflicting results. Singh et al. [7] concluded that hydrogen passivation is effective only for the fast diffusing transition metals but not for Ti. More recently Jost and Weber found that hydrogen could interact with Ti, especially in n-type silicon [8]. By means of deep level transient spectroscopy (DLTS) they detected two electron traps due to Ti-H_n complexes in the hydrogenated Si samples and from annealing studies concluded that there was at least one Ti-H_n complex with no energy levels in the gap [8]. In the present work we show that interactions of H atoms with interstitial Ti atoms (Ti_i) occur in n-type Si and result in the formation of three different electrically active Ti-H defects, which can further be transformed into electrically inert complexes upon annealing in the temperature range 100-150 ^oC. It is found that almost complete passivation of Ti can be achieved through hydrogen plasma treatments at room temperature and a 30 minute heat treatment at 150 ^oC.

6.3.Experimental Methods

Titanium was introduced into n-type Czochralski-grown (Cz) silicon with resistivity of 0.7 ± 0.2 Ωcm by multi-energy low-dose ion implantation (ion energies in the range of 300 keV to 2 MeV and doses from 2×10^{10} to 5×10^{10} cm^{-2}). The implantation was aimed at achieving uniform Ti concentration in the layer of 2 μm from the surface. Samples were then cut from the middle of the wafer, cleaned and annealed for 30 minutes at 650 ^{o}C in a nitrogen gas ambient in order to remove the implantation damage and activate the Ti. Hydrogen was introduced into the samples by a 60 minute treatment from a remote hydrogen plasma at room temperature. The following plasma parameters were used: power – 50 W, gas pressure – 1-2 mbar, gas flow – 200 cm^3/min. Shottky diodes were then formed on the samples by thermal evaporation of Au through a shadow mask and a layer of Al was thermally evaporated onto the back side to form an Ohmic contact. 30-minute isochronal annealing of the samples with the Schottky diodes was then carried out in a nitrogen gas ambient in the temperature range 100 - 250 ^{o}C.

Current-voltage and capacitance-voltage (C-V) measurements were undertaken at different temperatures to check the quality of the diodes, determine the concentration of shallow uncompensated donors and evaluate the probing depths for capacitance transient measurements. Deep Level Transient Spectroscopy (DLTS) and Laplace DLTS (LDLTS) [9] were used to characterize defects with deep electronic levels.

6.4.Results and Discussion

Fig. 1 shows the conventional DLTS spectra of the Ti-implanted Si samples, which were annealed at 650 ^{o}C {spectra 1(a)-1 and 1(b)-1} and then treated in hydrogen plasma {spectra 1(a)-2 and 1(b)-2}. The spectra in Fig. 1(a) and Fig. 1(b) were taken from the regions with low and high hydrogen concentrations respectively, after the plasma treatment. Hydrogen incorporated into n-type silicon strongly interacts with shallow donor impurities which can be seen in the uncompensated shallow donor concentration (N_d^+) profiles [10]-[11]. The N_d^+ profile measured after the H plasma treatment

indicates that the hydrogen has penetrated about 1 μm into the silicon. Two strong peaks with their maxima at about 40 K and 150 K dominate the DLTS spectra of the non-hydrogenated samples. These spectra resemble those reported in the literature for n-type Si samples which were doped with Ti either during crystal growth or by high-temperature in-diffusion [5],[8],[12]-[13]. Electronic signatures (activation energy for electron emission and pre-exponential factor) were determined for the dominant traps from Arrhenius plots of T^2-corrected electron emission rates, measured with the use of LDLTS. A comparison of the derived values (given in Table I) with those known from the literature for defects in Ti-doped n-Si crystals allows us to associate these peaks with electron emission from the singly negatively charged and neutral states of interstitial Ti atoms [3],[13].

Trap	Activation Energy (eV)	Pre exponential factor ($s^{-1}K^{-2}$)	Apparent Capture Cross section (cm^2)	Assignment
E(40)	0.07 ± 0.01	1.1×10^{7}	1.7×10^{-15}	$Ti_i(-/0)$
E(45)	0.075 ± 0.01	4.0×10^{6}	6.1×10^{-16}	$Ti\text{-}H_n$?
E(150)	0.27 ± 0.01	3.0×10^{6}	4.6×10^{-16}	$Ti_i(0/+)$
E(175)	0.34 ± 0.015	2.0×10^{7}	3.1×10^{-15}	$Ti\text{-}H_n$?
E(270)	0.56 ± 0.01	2.4×10^{7}	3.7×10^{-15}	$Ti\text{-}H_n$?

TABLE I. Activation energies for electron emission (E_e), pre-exponential factors, apparent capture cross sections, and possible assignments of deep level traps in hydrogenated Ti-implanted Silicon. The given uncertainties in the E_e values include both the data scattering in the Arrhenius plots and the variations for a few samples measured.

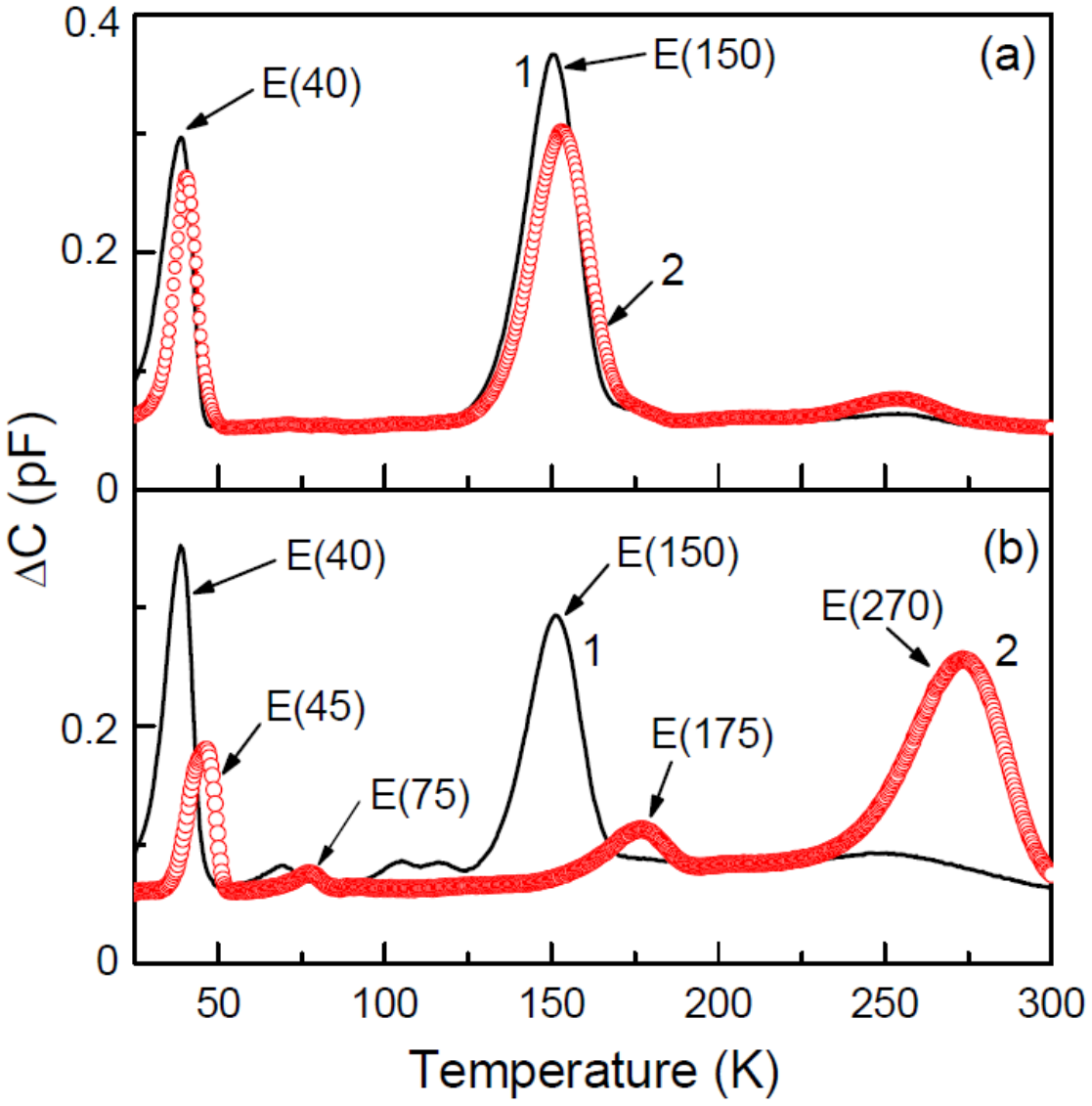

FIG. 1. DLTS spectra of Ti implanted n-type Cz-Si samples taken after a 30 minute annealing at 650 ^{o}C {spectra 1(a)-1 and 1(b)-1} and a following 60 minute hydrogen plasma treatment at room temperature {spectra 1(a)-2 and 1(b)-2}. The measurement conditions were the following: 1a) rate window (e_n) – 80 s^{-1}, reverse bias (U_r) – -4 V, filling pulse voltage (U_p) – -2 V, and filling pulse length (t_p) – 1 ms; 1b) e_n = 80 s^{-1}, U_r = -1 V, U_p = 0 V, and t_p = 1 ms. The spectra are shifted by 0.05 pF along the vertical axis for clarity.

The DLTS spectra taken after the hydrogen plasma treatment {spectra 1(a)-2 and 1(b)-2 in Fig. 1} strongly depend on the depth from the surface of the region studied. It can be seen from Fig. 1a) that the spectrum recorded with reverse bias of -4 V and pulse voltage of -2 V (the probing depth was from 0.91 μm to 1.06 μm at 40 K and from 0.80 μm to 0.97 μm at 300 K) is similar to that for the

non-hydrogenated samples. An analysis showed that some changes in magnitudes and positions of the dominant Ti-related DLTS peaks in this spectrum are associated mainly with the changes in diode capacitance and probing depths caused by the hydrogen passivation of phosphorus donors close to the surface. Fig. 1b) shows that close to the surface (from 0.62 μm to 0.81 μm at 40 K and from 0.47 μm to 0.69 μm at 300 K) drastic changes in the spectrum of deep levels were induced by the plasma treatment. The Ti_i-related DLTS peaks are not observed in the spectrum of the hydrogenated sample, and have been replaced with four other signals with peak maxima at about 45 K, 75 K, 175 K and 270 K. These emerging signals are labelled as E(45), E(75), E(175) and E(270) in Fig. 1. The signal with the peak maximum at about 75 K is rather weak. Further, it has been observed in the DLTS spectrum of a plasma-treated sample, which was not implanted with Ti. So, this peak will not be considered in the further analysis.

Laplace DLTS measurements have shown that the peak with its maximum at about 270 K consists of contributions from two emission signals. An emission signal with a smaller magnitude was observed in the LDLTS spectrum of a plasma-treated sample, which was not implanted with Ti. The dominant LDLTS signal was observed only in the H-plasma-treated Ti-doped samples. The concentration depth profiles of the Ti_i-related traps and the three dominant H-plasma-induced traps in the hydrogenated sample are shown in Fig. 2. The two profiles assigned to the Ti_i traps are very similar confirming that the traps are related to two different energy levels of the same defect. However, the three H-related traps all have very different profiles, suggesting that they are related to three different Ti-H complexes. These results vary somewhat to those obtained by Jost and Weber, [8] who found a far weaker passivating effect due to hydrogen, although this could be because they did not probe a region close to the surface. In the DLTS spectra presented by them a broadening of the peak at 40 K is observable, but they have not been able to resolve it as two different signals related to Ti_i and a Ti-H complex. They have also tentatively suggested that the two Ti-H-related signals with peak maxima close to those for the E(175) and E(270) signals could be associated with energy levels of the same defect but it can now clearly be seen that these are due to energy levels of two different Ti-H

complexes. Table I summarizes the data on electronic signatures of the dominant traps in hydrogenated Ti-doped samples. Determining compositions (number of hydrogen atoms incorporated and structure) of the Ti-H-related complexes is a difficult task. Sachse et al. [14] in a similar experiment involving Pt instead of Ti also observed three H-related DLTS peaks after a hydrogen treatment, which similarly had three different concentration profiles. They used a method outlined by Feklisova and Yarykin to relate the gradients of the far edges of the profiles to the number of hydrogen atoms attached to an impurity atom [15]. In their case this method suggested the observed DLTS signals were due to PtH, PtH_2 and PtH_3 complexes. The application of the same method to the profiles obtained by us (Fig. 2) did not give any conclusive results. A theoretical study by Backlund and Estreicher [16] suggests that interactions of hydrogen atoms with Ti_i will result in the formation of two different Ti-H complexes, but Ti-H_2 and Ti-H_3 complexes are not stable as the structures consisting of Ti_i and TiH with a separate hydrogen molecule are more energetically favourable. They also predict the existence of an electrically inactive TiH_4 complex. It should be noted that a small proportion of the implanted Ti atoms could exist in an electrically inactive substitutional configuration (Ti_s) in our samples because of the interaction of Ti_i atoms with implantation-induced vacancies [17]. Further, hydrogen could interact with the Ti_s atoms forming some electrically active complexes. An analysis of the concentration profiles in Fig 2 shows that the Ti_s-H complexes might be responsible for the DLTS peak with its maximum at 175 K but not for the Ti-H related peaks with their maxima at 45 K and 270 K. The maximum concentrations of the E(45) and E(270) traps exceed the concentration expected for the Ti_s atoms whereas the E(175) trap does not. The DLTS signals with maxima close to 175 K and 270 K were observed by Jost and Weber in hydrogenated n-Si samples, which were doped with Ti during growth [8]. It is believed that nearly all Ti atoms are located at interstitial sites in such samples, so the Ti-H-related traps with the DLTS peak maxima at 175 K and 270 K are likely to be related to Ti_i-H complexes.

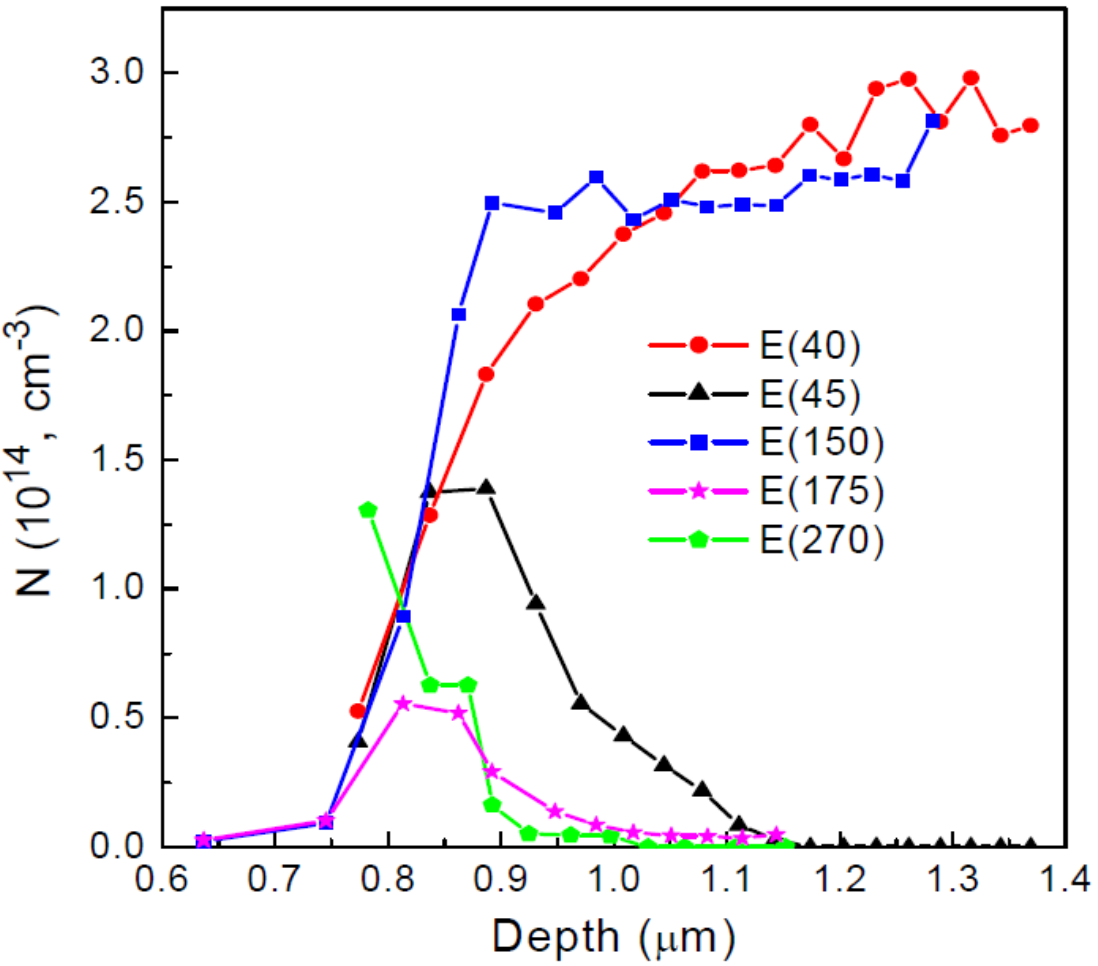

FIG. 2 Concentration depth profiles of the five dominant deep level traps seen in Figure 1. Profiles were taken with reverse bias varied from -10 V to -1 V and filling pulse voltage varied from -9 V to 0 V with 1 V difference between the bias and pulse voltages.

Figure 3 shows the changes in concentration profiles of uncompensated donor centers (N_d^+) and the DLTS spectra measured with reverse bias of -4 V and pulse voltage of 0 V (the probing depth varies with annealing steps and was from 0.3-0.45 μm to about 0.8-1.0 μm upon 30-minute isochronal annealing of a hydrogenated Ti-doped sample). A strong drop in the N_d^+ values close to the surface after the hydrogen plasma treatment is related to hydrogen passivation of phosphorus donors [10]-

[11]. This effect can be seen to disappear with increasing annealing temperature as the phosphorus-hydrogen defect is known to dissociate upon heat-treatments at T ≥ 100 °C.[11]

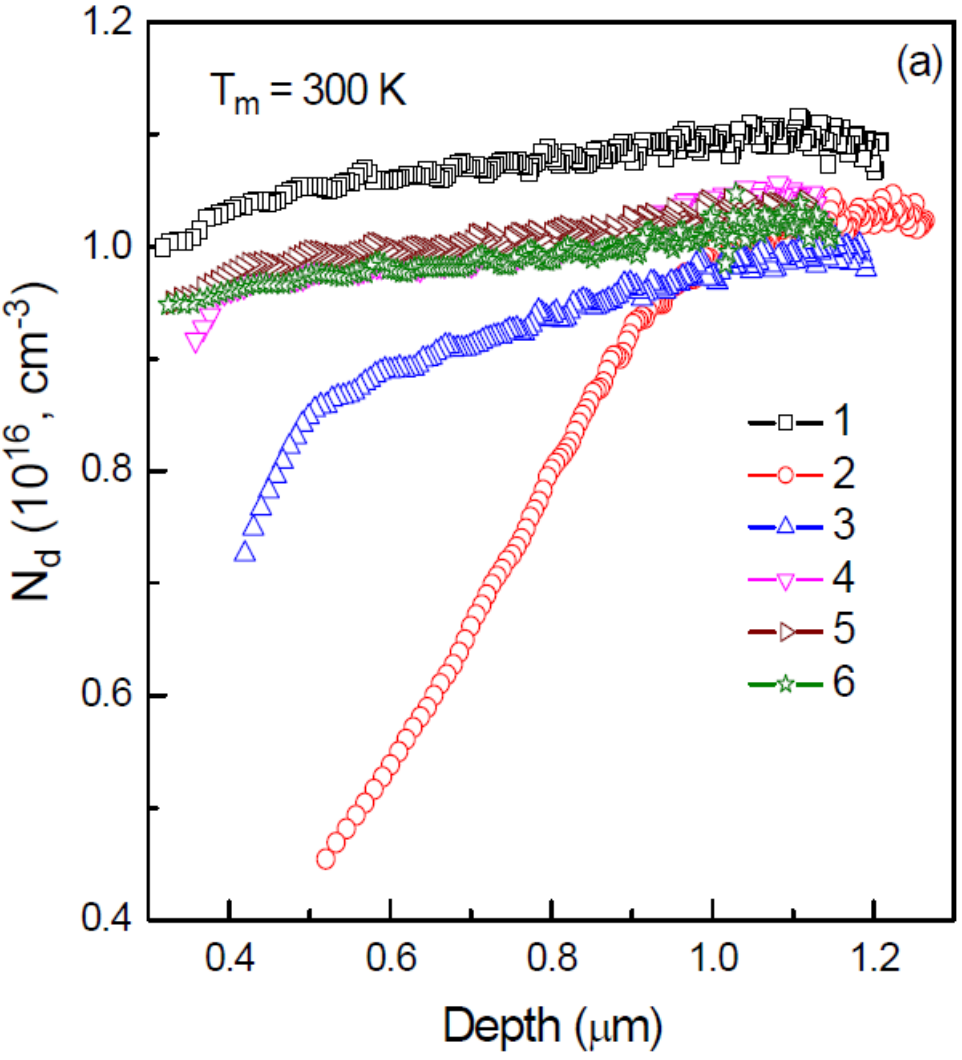

FIG. 3 (a) Profiles of uncompensated donors for a Ti implanted n-type Cz-Si sample taken after 1) 30 minute annealing at 650 °C in N_2 gas ambient, 2) subsequent hydrogen plasma treatment at room temperature and 3)-6) 30 minute isochronal annealing in the temperature range 100-250 °C with 50 °C increments.

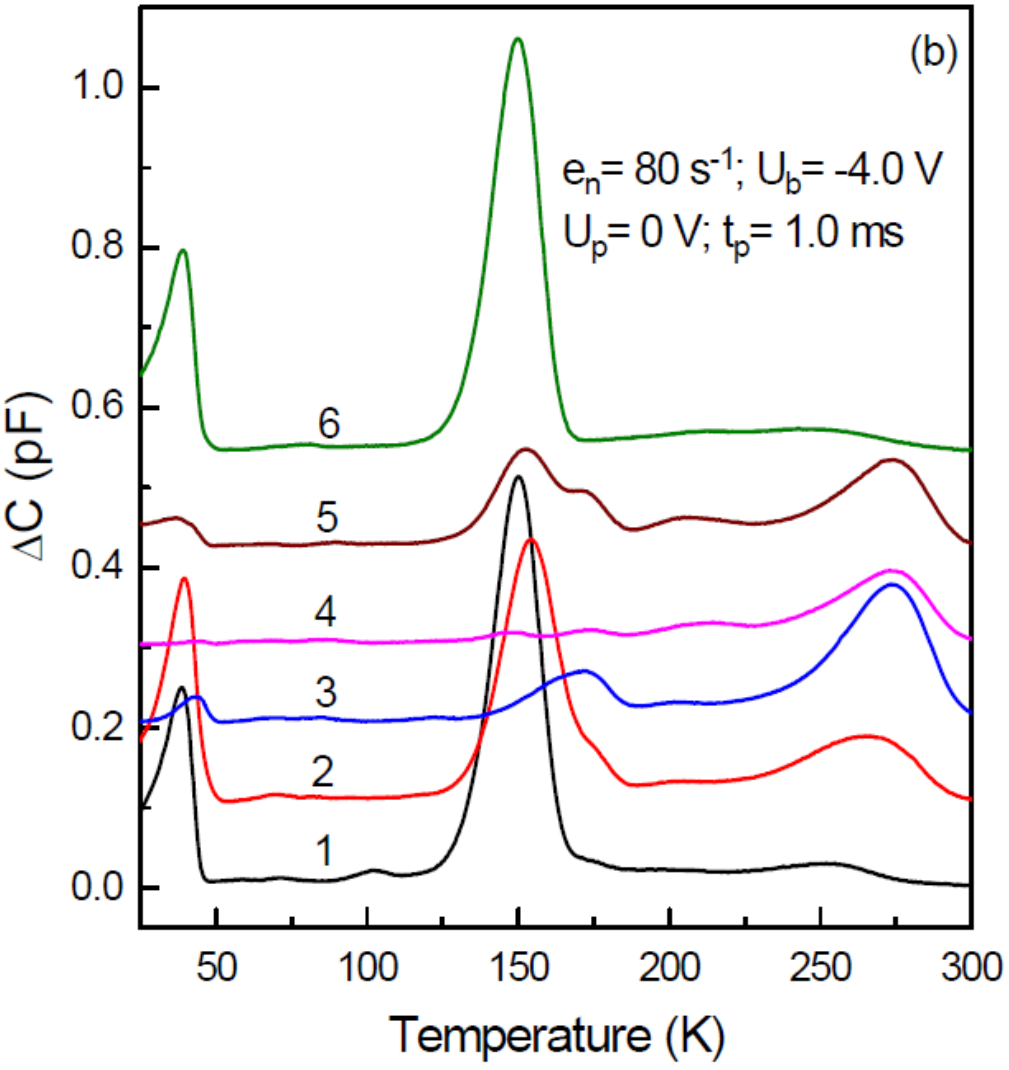

FIG. 3 (b) DLTS spectra for a Ti implanted n-type Cz-Si sample taken after 1) 30 minute annealing at 650 ^{o}C in N_2 gas ambient, 2) subsequent hydrogen plasma treatment at room temperature and 3)-6) 30 minute isochronal annealing in the temperature range 100-250 ^{o}C with 50 ^{o}C increments. The DLTS spectra were recorded with the following parameters: U_r = 4 V, U_p = 0 V, e_n = 80 s^{-1}, and t_p = 1 ms.

The DLTS spectrum taken after the hydrogen plasma treatment is similar to that shown in Fig. 1a) for the measurements with U_r = -4 V and U_p = -2 V. In the DLTS spectrum recorded after annealing at 100 ^oC, the DLTS peaks due to Ti_i nearly disappear and the three H-related peaks, which were seen in the subsurface region after the H-plasma treatment (Fig. 1b), are observed. The annealing at 150 ^oC caused almost complete passivation with only a small peak at 270 K due to a H-related complex remaining. Obviously, interactions of hydrogen atoms with the interstitial Ti atoms upon annealing at 150 ^oC have resulted in the formation of an electrically neutral Ti-H defect. It is likely that this defect is related to the TiH_4 complex [14]. The DLTS spectra recorded after annealing at 200 and 250 ^oC show that the Ti-H complexes are not stable in this temperature range and a recovery of the electrical activity of Ti_i atoms occurs. The spectrum after annealing at 250 ^oC almost exactly resembles the spectrum taken before the hydrogen plasma treatment.

6.5.Conclusion

Summarizing, it can be stated that the effective passivation of Ti with hydrogen was observed in n-type silicon. Hydrogenation at room temperature of Ti-doped n-type Cz-Si samples resulted in the passivation of phosphorus donors, a decrease in magnitudes of DLTS signals related to energy levels of Ti_i atoms, and the appearance of three hydrogen-related DLTS peaks. An analysis of the concentration profiles of the H-related deep levels showed that these levels are related to three different defects. A release of hydrogen caused by the dissociation of phosphorus-hydrogen centers upon heat-treatments in the temperature range 100-150 ^oC resulted in a further decrease in concentration of electrically active Ti_i atoms and in changes in the concentration of deep-level H-related defects. After annealing at 150 ^oC no signals due to Ti_i atoms and two of the three H-related defect were observable in the DLTS spectra showing that almost complete passivation of Ti_i atoms is possible with hydrogen. It appears that interactions of hydrogen with Ti_i atoms have led to the formation of a Ti-H complex with no deep energy levels in the higher part of the gap. Upon further

annealing in the temperature range 200-250 ^{o}C a recovery of electrical activity of Ti_i occurred. 30 minutes annealing at 250 ^{o}C resulted in the total recovery of the original (before hydrogenation) Ti_i-related DLTS spectrum.

6.6.Acknowledgements

We would like to thank the EPSRC (UK) for funding and Professor Russel Gwilliam of the Surrey Ion Beam Centre for undertaking the Ti implants.

6.7.References

[1] J. T. Borenstein, J. I. Hanoka, B. R. Bathey, J. P. Kalejs, and S. Mil'stein, Appl. Phys. Lett. **62**, 1616 (1993).

[2] D. A. van Wezep, R. van Kemp, E. G. Sieverts, and C. A. J. Ammerlaan, Phys. Rev. B **32**, 7129 (1985).

[3] K. Graff, Metal Impurities in Silicon-Device Fabrication (Springer, Berlin, 1995).

[4] S. Hocine, and D. Mathiot, Appl. Phys. Lett. **53**, 1269 (1988).

[5] S. Kuge and H. Nakashima, Jpn. J. Appl. Phys. **30**, 2659 (1991).

[6] F. Jiang, M. Stavola, A. Rohatgi, D. Kim, J. Holt, H. Atwater, and J. Kalejs, Appl. Phys. Lett. **83**, 931 (2003).

[7] R. Singh, S. J. Fronash, and A. Rohatgi, Appl. Phys. Lett. **49**, 800 (1986).

[8] W. Jost and J. Weber, Phys. Rev. B **54**, R11038 (1996).

[9] L. Dobacewski, A. R. Peaker, and K. Bonde Nielsen, J. Appl. Phys. **96**, 4689 (2004).

[10] N. M. Johnson, C. Herring, and D. J. Chadi, Phys. Rev. Lett. **56**, 789 (1986).

[11] J. Zhu, N. M. Johnson, and C. Herring, Phys. Rev. B **41**, 12354 (1990).

[12] A. C. Wang and C. T. Sah, J. Appl. Phys. **56**, 1021 (1984).

[13] D. Mathiot and S. Hocine, J. Appl. Phys. **66**, 5862 (1989).

[14] J.-U. Sachse, J. Weber, and E. Ö. Svenbjörnsson, Phys.Rev. B 60, 1474(1999).

[15] O. V. Feklisova and N. Yarykin, Semicond. Sci. Techn. **12**, 742 (1997).

[16] D. J. Backlund and S. K. Estreicher, Phys. Rev. B **82**, 155208 (2010).

[17] D. J. Backlund and S. K. Estreicher, Phys. Rev. B **81**, 2352138 (2010).

Paper 2

Titanium in silicon: Lattice positions and electronic properties

V. P. Markevich, S. Leonard, A. R. Peaker, B. Hamilton, A. G. Marinopoulos, and J. Coutinho

Appl. Phys. Lett., vol. 104, no. 15, p. 152105, 2014.

7. Titanium in silicon: Lattice positions and electronic properties

7.1.Abstract

Secondary ion mass spectroscopy (SIMS) and deep level transient spectroscopy measurements were carried out on Czochralski (Cz)- and float-zone-grown (FZ) Si crystals, which were implanted with Ti ions and annealed in the temperature range 600-900 ^{o}C. The electrical behavior of Ti atoms is found to be different in Cz- and FZ-Si annealed at 650 ^{o}C although the Ti SIMS profiles are similar. It is argued that interstitial Ti atoms (Ti_i) in FZ-Si crystals interact with implantation-induced vacancies and take a substitutional position (Ti_s). No energy levels which can be assigned to Ti_s have been detected in this work or in previous experimental literature. However previous calculations suggest that Ti_s is a deep acceptor in Si. We show from density functional calculations that by taking proper account of interactions within the d-shell of the Ti impurity the electronic structure of Ti_s has no levels in the band gap. The calculations show that Ti_i is more energetically favorable than Ti_s and that Ti_i binds more strongly to the silicon vacancy than interstitial oxygen does, explaining the observed differences between FZ- and Cz-irradiated materials.

7.2.Introduction

Titanium in silicon is a powerful recombination center[1]-[3] and a slow diffuser,[4]-[5] thus being simultaneously difficult to getter and an efficiency-limiting impurity in solar cells fabricated from some types of solar grade silicon[1],[6]. It is thought that Ti incorporates into the Si lattice mainly as single interstitial (Ti_i) atoms at tetrahedral sites,[2],[7] and these are responsible for three energy levels in the gap: a double donor level at $E_V + 0.26$ eV, a donor level at $E_C - 0.27$ eV and an acceptor level at $E_C - 0.08$ eV [1]-[2],[5],[8]-[11]. Recently, Ti doped silicon has been seriously considered as a promising intermediate-band material for fabrication of third generation solar cells [12]-[13]. Such an intermediate-band absorber requires a Ti doping level above the Mott transition (~ 5×10^{19} cm^{-3}), [14] which is only achievable by ion implantation. Olea et al. [12] have produced ~ 6×10^{19} cm^{-3} interstitial Ti impurities in laser annealed Si implanted with Ti ions, but they found that a significant fraction of Ti was located at substitutional sites (Ti_s). It was not clear what the relative role of interstitial and substitutional Ti was in terms of the optical and electrical properties of the implanted Si absorbers.

From theory, the general picture is that Ti at the tetrahedral interstitial lattice site produces three levels in the gap, whereas Ti_s introduces an acceptor level lying just below the conduction band (CB) minimum and perhaps a donor level edging the valence band maximum (see Refs. [15] and [16] and references therein). While these results account well for the observations related to Ti_i, the existence of any Ti_s-related levels lacks experimental confirmation.

7.3.Experimental Method

In order to obtain more information on the lattice positioning and electronic properties of Ti atoms in Si, we carried out secondary ion mass spectroscopy (SIMS) and deep level transient spectroscopy (DLTS) measurements on Czochralski-grown (Cz) and float-zone-grown (FZ) Si crystals. Further, we

calculated the stable configurations, electronic structure and formation energies of Ti centers, as well as reaction energetics of Ti with some relevant vacancy-related defects in Si.

Titanium was introduced into n-type and p-type Cz-grown and FZ-grown Si wafers with the ⟨111⟩ orientation by multi-energy low-dose ion implantation (ion energies in the range of 300 keV to 2 MeV and doses from 2×10^{10} to 5×10^{10} cm^{-2}). The implantation was planned to achieve a near uniform Ti concentration in the Si layer from the surface to 2 μm deep. Samples were then cut from the wafers, cleaned and annealed for 30 minutes in the temperature range 600-900 ^{o}C in a nitrogen gas ambient for removing the implantation damage and activating the Ti. Schottky diodes were formed on the n(p)-type samples by thermal evaporation of Au(Ti) through a shadow mask and a layer of Al(Au) was evaporated onto the back side to form an Ohmic contact.

Current-voltage and capacitance-voltage (C-V) measurements were undertaken to check the quality of the diodes and determine the concentration of shallow uncompensated donors and acceptors. Deep Level Transient Spectroscopy (DLTS) and Laplace DLTS (LDLTS)[17] were used to characterize defects with deep electronic levels. Concentration and depth distribution of Ti were determined by means of SIMS using a Cameca Ims 4f microanalyzer. O^{2+} ions with the energy of 10 keV were used for sputtering. The secondary ions monitored were $^{48}Ti^{+}$ and $^{30}Si^{+}$. Depth scales were determined by measuring the sputtered crater depths using a Dektak 6M. The data were quantified using an implanted reference sample of Ti in Si.

For the theoretical calculations we employed the spin-polarized density-functional theory (DFT) and the projector augmented-wave (PAW) method [18] as implemented in the VASP code [19]. The exchange-correlation potential was considered both within the generalized-gradient approximation (GGA) [20] and within the intra-atomic correlation-corrected GGA (GGA+U) [21]. Several values for the Oon-site Mott-Hubbard effective interaction U were tested (from 1 to 6 eV) spanning the range of U-values commonly used for the Ti 3d orbitals in TiO_2 crystalline phases [22]. Valence-core interactions were accounted for by the use of pseudopotentials that included the semi-core 3s and

3p states of Ti. The plane-wave basis of the Kohn-Sham states was limited to a kinetic-energy cut-off of 300 eV or 450 eV, the latter being used when the oxygen species was present. Full atomic and electronic relaxations were performed on cubic-shaped 512-atom Si supercells with Γ-sampled Brillouin-zones. Formation energies were calculated with respect to chemical potentials of Si, Ti and O species calculated from crystalline Si, $TiSi_2$ (C49 phase) and SiO(α-quartz), respectively.

7.4.Results and Discussion

Fig. 1 shows the conventional DLTS spectra of the Ti-implanted Si samples, which were annealed at 650 ^{o}C and 800 ^{o}C. Two strong peaks with their maxima at about 40 K and 150 K dominate the DLTS spectrum of the n-type Cz-Si sample, which was annealed at 650 ^{o}C. In the spectrum of the p-type Cz-Si sample annealed at 650 ^{o}C there is one dominant peak with its maximum at about 183 K. Concentration profiles of the traps, which gives rise to the dominant peaks are shown in Fig. 2. The spectra for Cz-Si samples annealed at 650 ^{o}C resemble those reported in the literature for n-type and p-type Si samples which were doped with Ti either during crystal growth or by high-temperature in-diffusion[1]-[2],[5],[8]-[11]. Electronic signatures (activation energy for electron emission and pre-exponential factor) were determined for the dominant traps from Arrhenius plots of T^2-corrected electron emission rates, measured with the use of LDLTS. A comparison of the derived values with those known from the literature for defects in Ti-doped n-Si crystals allows us to associate the peaks in n-type Cz-Si with electron emission from Ti_i^- and Ti_i^0. The peak in p-type Cz-Si is associated with hole emission from Ti_i^{++} [1]-[2],[5],[8]-[11].

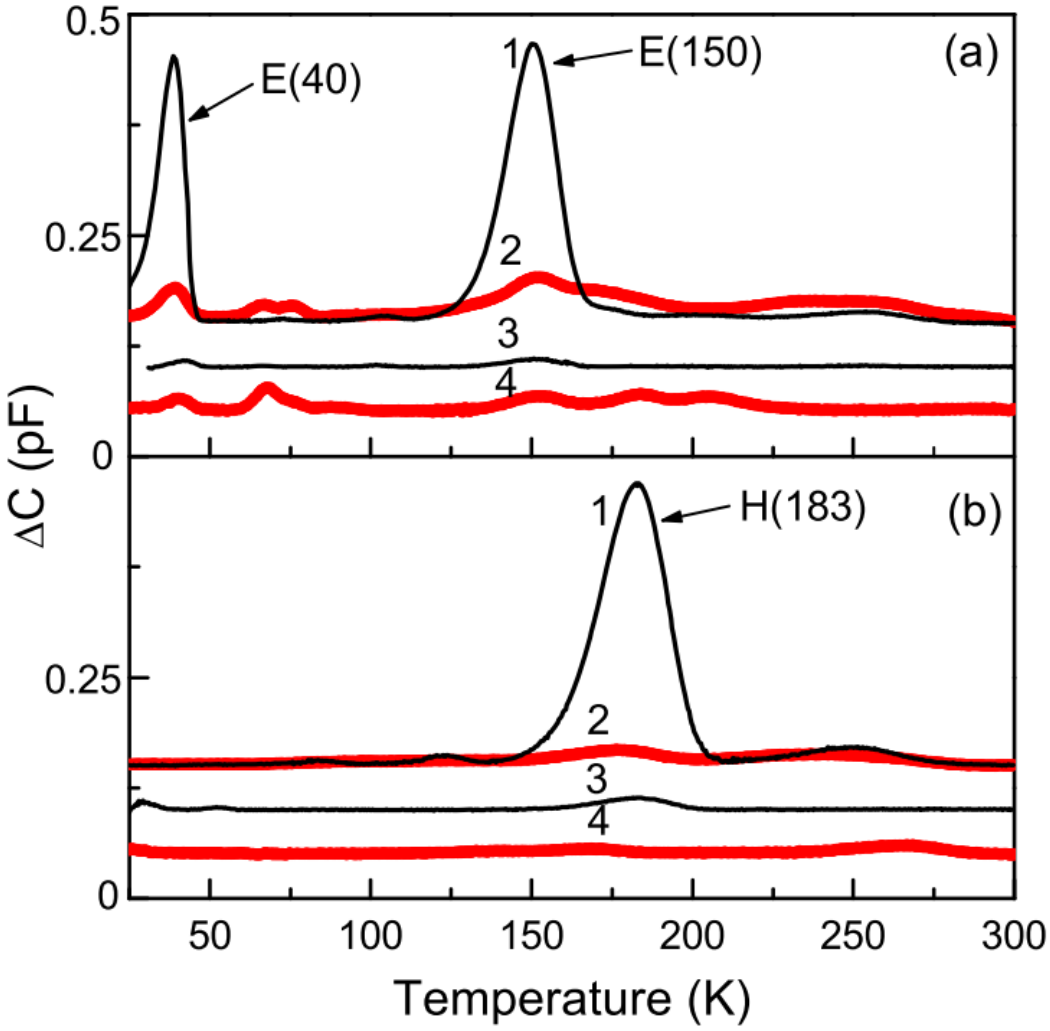

FIG. 1. DLTS spectra of the Ti implanted (a) n-type and (b) p-type samples taken after a 30 minute annealing at 650 °C (spectra 1 and 2) and 800 °C (spectra 3 and 4). The spectra 1 and 3 are for the Cz-Si samples, and the spectra 2 and 4 are for the FZ-Si samples. The measurement conditions were the following: a) rate window e_n = 80 s^{-1}, reverse bias U_r = –4.0 V, filling pulse voltage U_p = –2.0 V, and filling pulse length t_p = 1 ms; b) e_n = 80 s^{-1}, U_r = –8.0 V, U_p = –4.0 V, and t_p = 1 ms.

The DLTS spectra for Fz-Si implanted samples, which were annealed at 650 °C, differ significantly from those for similarly implanted and annealed Cz-Si samples. Magnitudes of the DLTS peaks related to carrier emission from the Ti_i traps are much smaller for FZ-Si samples compared to those for Cz-Si samples. After annealing at 800 °C the magnitudes of the Ti_i-related DLTS peaks in Cz-Si samples are significantly reduced in comparison to those in the same materials annealed at 650 °C.

Some traces of deep-level defects are detected in all samples annealed at 800 ^{o}C but the concentrations of the traps do not exceed 5×10^{12} cm^{-3}.

Fig. 2 shows concentration profiles of Ti impurity atoms measured by SIMS in the Cz- and FZ-samples in as-implanted state and after annealing at 650 and 800 ^{o}C. Also the concentration profiles of electrically active Ti_i atoms derived from DLTS and C-V measurements in n- and p-type Cz-Si samples annealed at 650 ^{o}C are presented in Fig. 2(a). A combined analysis of the SIMS and DLTS profiles show that the concentration of interstitial Ti atoms is close to the total concentration of Ti atoms in the Cz-Si samples annealed at 650 ^{o}C, while in the similarly annealed FZ-Si samples only a small fraction (a few %) of Ti atoms introduced by ion implantation resides at tetrahedral interstitial positions. Concentrations of the traps related to the minor peaks seen in the DLTS spectra of the FZ-Si samples annealed at 650 ^{o}C is much smaller than the total concentration of Ti atoms detected by SIMS in the probed region. Apparently, most of Ti atoms in the FZ samples annealed at 650 ^{o}C are in a state that is not detected by DLTS.

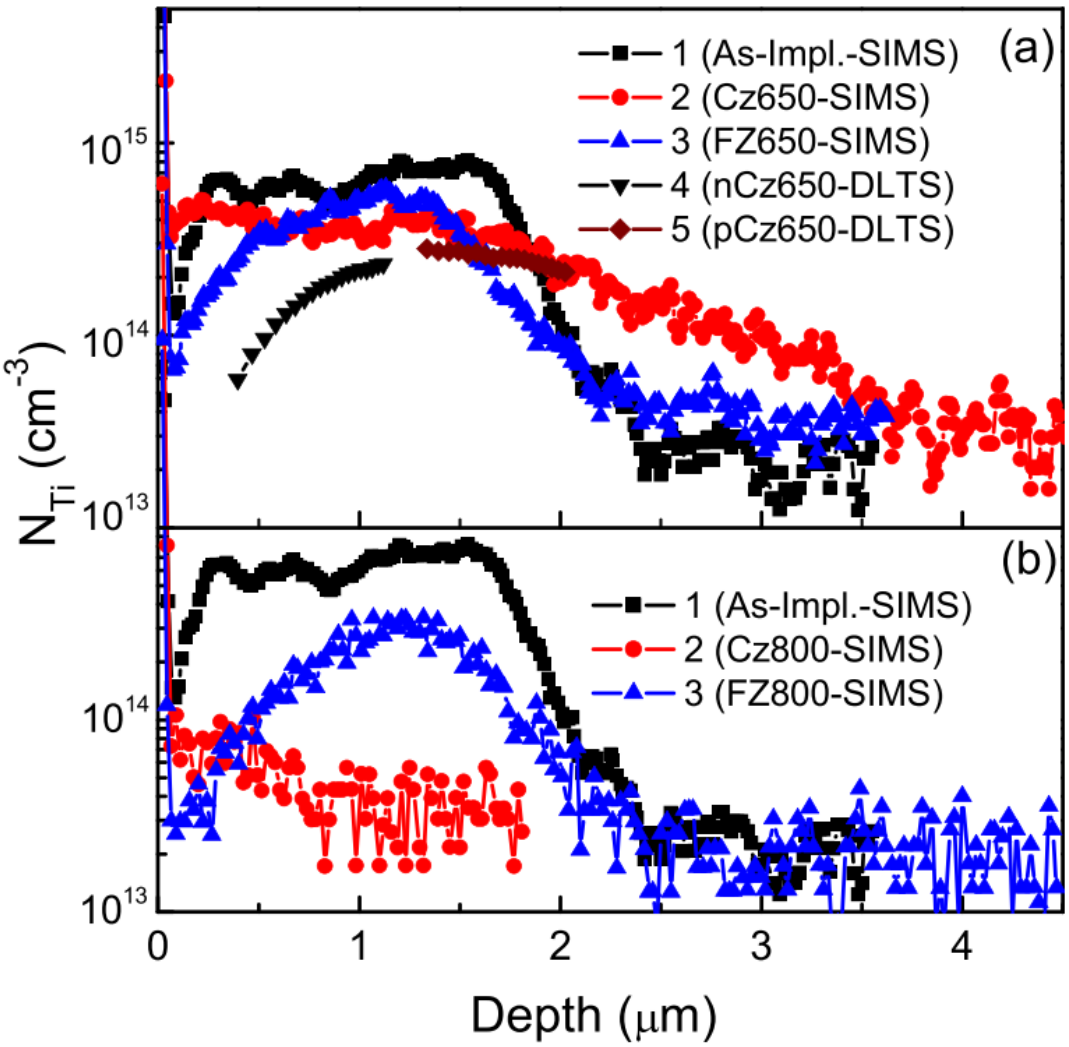

FIG. 2. Concentration depth profiles of Ti atoms in the Ti-implanted Cz- and FZ-Si samples measured by SIMS in as-implanted state and after annealing for 30 min at (a) 650 °C and (b) 800 °C. Concentration depths profiles of Ti_i atoms derived from DLTS and C-V measurements on n- and p-type Cz-Si samples annealed at 650 °C are also shown in (a).

As the implanted Ti peak concentration was below 10^{15} cm^{-3} and the Ti is a very slow diffuser at 650 °C it seems unlikely that the difference is due to Ti related precipitates. Consequently we hypothesize that a large portion of these electrically inert Ti atoms reside at substitutional sites. The contrasting behavior of Ti in the Cz- and FZ-Si samples annealed at 650 °C is likely to be due to interactions of implantation-induced vacancies (V) with impurity atoms upon annealing. It is well known that oxygen atoms are effective traps for mobile vacancies in silicon and some of the V-O

complexes (eg., VO_5 and VO_6) survive after annealing at temperatures as high as 700 ^oC [23]. As the concentration of oxygen atoms in the Cz-Si samples studied exceed that of the Ti atoms by at least three orders of magnitude, it is reasonable to suggest that vacancy-oxygen reactions are dominating the Ti-vacancy reaction in the Cz-Si samples. The oxygen concentration in the FZ-Si samples is much lower compared to that in the Cz-Si samples, so, in FZ-Si many more vacancies are available to react with the implantation-induced Ti atoms. Such interactions can result in Ti atoms residing at substitutional lattice sites, [16] where according to our measurements they are electrically inert.

The concentration profiles of Ti impurity atoms measured by SIMS in Cz-Si samples after annealing at 800 ^oC [Fig. 2(b)] show that this 30-min heat-treatment was enough for redistribution of Ti atoms in the probed region down to the SIMS detection limit. The diffusion length for Ti_i atoms for these conditions of annealing exceeds 2 μm, [5] facilitating escape from the region probed. In the FZ-Si samples annealed at 800 ^oC the concentration of Ti atoms in the region from about 0.5 μm to about 1.75 μm exceeds 10^{14} cm^{-3}. A comparison of the Ti SIMS profiles in the FZ- and Cz-Si samples annealed at 800 ^oC indicates that as expected the substitutional Ti atoms are much less mobile than Ti_i atoms in Si.

Now we move on to the first-principles calculations where we start by reporting the GGA-level results. After full structural relaxation, minimum-energy configurations for Ti_i and Ti_s ended up with full tetrahedral (T_d) symmetry. In line with previous theoretical results [16] the ground state of Ti_i was found to have spin S = 1, 3/2, 1, and ½ for charge states ++, +, 0, and −, whereas for Ti_s we found S = 0 and S = 1/2 for the 0 and − charge states, respectively. A variety of low-symmetry distorted structures were further inspected but, in comparison to T_d structures, led to insignificant or no energy gains.

The calculated formation energy of Ti_i (in equilibrium with $TiSi_2$ precipitates) was found to be 2.96 eV. This value matches quite well the 3.05 eV formation energy measured from depth-profile DLTS measured on $TiSi_2$/Si structures [4]. In line with recent DFT-GGA calculations, [15] our results show

that neutral (S = 1) Ti_i has a formation energy at least 0.86 eV lower than the diamagnetic Ti_s and that in p-type material this difference can go up to 2 eV. We can estimate the solubility of Ti in Si as $n_0 exp(-E_f/k_BT)$ at a specific temperature T, where n_0 is the density of available sites (5×10^{22} cm^{-3} for Ti_s and half of that for Ti_i), E_f is the formation energy and k_B is the Boltzmann constant. For neutral Ti this gives $[Ti_i] = 3.6 \times 10^{13}$ cm^{-3} and $[Ti_s] = 1.9 \times 10^{11}$ cm^{-3} at the melting point (T ~ 1400 ^oC), which means that in non-implanted (as-grown) samples about 0.5% of dispersed Ti will be incorporated at substitutional sites. This estimate actually represents an upper bound since Ti_i can be further stabilized as positive ions for a wide range of Fermi-level (E_F) values.

Based on the experiments, we have argued above that in contrast to Cz-Si, the relatively low interstitial oxygen (O_i) concentration in FZ-grown material gives vacancies (V) (from implanted regions) the opportunity to interact with Ti_i impurities, therefore resulting in the formation of Ti_s. Although the idea is a plausible one, we have to demonstrate that vacancies bind more strongly to Ti_i than to O_i. This was done by looking at the binding energies (E_b) of the competing reactions:

$$V + Ti_i \rightarrow Ti_s + E_{b,Ti} \quad (1)$$

$$V + O_i \rightarrow VO + E_{b,O}, \quad (2)$$

with VO being the vacancy-oxygen complex. From the calculations, the formation energies for neutral V, VO and O_i are 3.53 eV, 3.53 eV and 1.60 eV, respectively. Both donor and acceptor levels of vacancy show a negative-U ordering and we place them at $V(0/++) = E_V + 0.11$ eV and $V(=/0) = E_C - 0.27$ eV, in agreement with previous results [24]. For the VO defect we predict its (–/0) energy level at $E_C - 0.17$ eV matching the measured value [25]. Combining formation energy and electrical level calculations we obtained $E_{b,Ti}$ and $E_{b,O}$ as a function of E_F. Accordingly, while $E_{b,O}$ is about 1.6 eV for most E_F values, it decreases to about 1.3 eV in p- and n-type Si. On the other hand, $E_{b,Ti}$ is higher than 2 eV for most E_F values, and peaks at 2.67 eV under intrinsic conditions. These results support our

view in that Ti_s is not formed in Cz-Si subjected to implantation/anneals because of the large number of O impurity atoms available to react with vacancies.

In line with the long-standing model of Ludwig and Woodbury,[26] the crystal field of the Si host lifts the degeneracy of the Ti 3d-orbitals into doublet (e) and triplet (t_{2g}) states. For Ti_i, the t_{2g}^4 state lies in the gap while the e^0-state is located above the CB minimum. In Ti_s, the strong coupling of the Ti t_{2g} states to the four dangling bonds ($a_1^2 + t_{2g}^2$) of the Si vacancy results in the formation of bonding and anti-bonding t_{2g} resonances within the valence and conduction bands, respectively. The empty e^0-state is left in the gap and possesses a strong atomic-like character. In agreement with previous DFT reports[15]-[16] it is located 0.15 eV below the CB minimum at $\mathbf{k} = \Gamma$.

Electrical levels were determined by means of the marker method, taking as marking reference the ionization potential and electron affinity of bulk Si [27]. In agreement with comparable DFT-GGA calculations, [16] Ti_i was found to give rise to two donor levels, at E(++/+) = E_V + 0.10 eV and E(+/0) = E_V + 0.51 eV, and to one acceptor level at $E_C - 0.14$ eV. While E(++/+) and E(0/−) agree closely with the DLTS data, the first donor level is about 0.3 eV below the experimental value. This discrepancy may reflect the fact that the marker method works better when the defect under scrutiny has levels close to those of the marker. Subsequent GGA+U calculations showed that on-site correlation ($U \neq 0$) brings the Ti_i(+/0) level closer to the experimental value, although it also shifts the (++/+) and (0/−) levels closer to the band edges. A compromise among discrepancies for all three levels was obtained for $U \approx 3$ eV, with E(++/+) = E_V + 0.06 eV and E(+/0) = E_V + 0.59 eV and the acceptor level at E(−/0) = $E_C - 0.05$ eV.

For Ti_s the GGA calculations (U = 0) lead to an acceptor level E(0/−) = $E_C - 0.14$ eV, in agreement with comparable calculations reported previously, [15]-[16] but at variance with the present DLTS data. We found, however, that the effect of U on the Kohn-Sham levels of Ti_s is rather strong, especially on the e-state. Sensitivity tests to the impact of U showed that this level progressively shifts towards

the CB edge with increasing U, and starts to merge with the host CB for $U \geq 2$ eV. Using the marker method and within GGA+U (U = 3 eV) we did not find an acceptor level for Ti_s. This supports the view of an electrically inert and isovalent Ti_s in Si, but also suggests that previous predictions of a E(0/−) level may have resulted from an inadequate treatment of correlation within LDA/GGA.

7.5.Conclusion

Summarizing, from a combined SIMS-DLTS study of Cz- and FZ-Si samples implanted with Ti ions and annealed in the temperature range 600-900 ^{o}C we found evidence for the existence of substitutional Ti atoms in the Si lattice. It is argued that the implantation-induced Ti_i atoms in FZ-Si crystals interact with implantation-induced vacancies and take a substitutional position. This does not happen in Cz-Si as the most probable reactions of vacancies are with the highly abundant oxygen atoms. No energy levels due to Ti_s have been detected and from the SIMS data their diffusivity is found to be lower than that of Ti_i. From formation energy calculations we show that vacancies bind considerably stronger to Ti_i than to O_i defects. This explains the preference for the reaction route $V + Ti_i \rightarrow Ti_s$ in low-O FZ-Si samples in contrast to O-rich Cz-Si where all implanted-induced vacancies are consumed by O_i defects. The calculations also show that the treatment of on-site correlation within the 3d shell of Ti is an important ingredient for a correct description of the electrical activity of Ti_s in Si.

7.6.Acknowledgements

We would like to thank the EPSRC (UK) and FCT (Portugal) under the grants PTDC/CTM-ENE/1973/2012 and PEst-C/CTM/LA0025/2011 for funding. Prof. Russel Gwilliam of the Surrey Ion Beam Centre is thanked for undertaking the Ti implants. The SIMS measurements were undertaken by Dr. Alison Chew of Loughborough Surface Analysis Ltd, UK. JC thanks Dr. Benjamin Hourahine for useful discussions.

7.7.References

[1] J.-W. Chen, A. G. Milnes, and A. Rohatgi, Solid State Electronics **22**, 801 (1979).

[2] K. Graff, Metal Impurities in Silicon-Device Fabrication (Springer, Berlin, 1995).

[3] B. B. Paudyal, K. R. McIntosh, and D. H. Macdonald, J. Appl. Phys. **105**, 124510 (2009).

[4] S. Hocine, and D. Mathiot, Appl. Phys. Lett. **53**, 1269 (1988).

[5] S. Kuge and H. Nakashima, Jpn. J. Appl. Phys. **30**, 2659 (1991).

[6] J. T. Borenstein, J. I. Hanoka, B. R. Bathey, J. P. Kalejs and S. Mil'shtein, Appl. Phys. Lett. **62**, 1615 (1993)

[7] D. A. van Wezep, R. van Kemp, E. G. Sieverts, and C. A. J. Ammerlaan, Phys. Rev. B **32**, 7129 (1985).

[8] A. C. Wang and C. T. Sah, J. Appl. Phys. **56**, 1021 (1984)

[9] D. Mathiot and S. Hocine, J. Appl. Phys. Phys. **66**, 5862 (1989).

[10] W. Jost and J. Weber, Phys. Rev. B **54**, R11038 (1996).

[11] S. Leonard, V. P. Markevich, A. R. Peaker, and B. Hamilton, Appl. Phys. Lett. **103**, 132103 (2013).

[12] J. Olea, M. Toledano-Luque, D. Pastor, G. González-Díaz, and I. Mártil, J. Appl. Phys. **104**, 016105 (2008).

[13] H. Castán, E. Pérez, H. García, S. Dueñas, L. Bailón, J. Olea, D. Pastor, E. García-Hemme, M. Irigoyen and G. González-Díaz, J. Appl. Phys. **113**, 024104 (2013).

[14] A. Luque, A. Martí, E. Antolín, C. Tablero, Physica B **382**, 320 (2006).

[15] K. Sánchez, I. Aguilera, P. Palacios, and P. Wahnón, Phys. Rev. B **79**, 165203 (2009).

[16] D. J. Backlund and S. K. Estreicher, Phys. Rev. B **81**, 235213 (2010).

[17] L. Dobacewski, A. R. Peaker, and K. Bonde Nielsen, J. Appl. Phys. **96**, 4689 (2004).

[18] G. Kresse and D. Joubert, Phys. Rev. B **59**, 1759 (1999).

[19] G. Kresse and J. Hafner, Phys. Rev. B **47**, 558 (1993); ibid, Phys. Rev. B **49**, 14251 (1994); G. Kresse and J. Furthmüller, Phys. Rev. B **54**, 11169 (1996).

[20] J. P. Perdew, K. Burke and M. Ernzerhof, Phys. Rev. Lett. **77**, 3865 (1996).

[21] S. L. Dudarev, G. A. Botton, S. Y. Savrasov, C. J. Humphreys and A. P. Sutton, Phys. Rev. B **57**, 1505 (1998).

[22] J. Morgan and G. W. Watson, J. Phys. Chem. C **113**, 7322 (2009).

[23] L. I. Murin, J. L. Lindstrom, V. P. Markevich, A. Misiuk, and C.A. Londos, J. Phys.: Condens. Matter **17**, S2237 (2005).

[24] A. F. Wright, Phys. Rev. B **74**, 165116 (2006).

[25] G. D. Watkins and J. W. Corbett, Phys. Rev. **121**, 1001 (1961).

[26] G. W. Ludwig and H. H. Woodbury, Phys. Rev. Lett. **5**, 98 (1960).

[27] J. Coutinho, V. P. Markevich, A. R. Peaker, B. Hamilton, S. B. Lastovskii, L. I. Murin, B. J. Svensson, M. J. Rayson and P. R. Briddon, Phys. Rev. B **86**, 174101 (2012).

Paper 3

Evidence for an-Iron Hydrogen Complex in p-type Silicon

S. Leonard, V. P. Markevich, A. R. Peaker, B. Hamilton, J.D. Murphy

Appl. Phys. Lett., vol. 107, p. 032103, 2015.

8. Evidence for an Iron-Hydrogen Complex in p-type Silicon

8.1. Abstract

Interactions of hydrogen with iron have been studied in Fe contaminated p-type Czochralski silicon using capacitance-voltage profiling and deep level transient spectroscopy (DLTS). Hydrogen has been introduced into the samples from a silicon nitride layer grown by plasma enhanced chemical vapor deposition. After annealing of the Schottky diodes on Si:Fe+H samples under reverse bias in the temperature range 90-120 ^{o}C a trap has been observed in the DLTS spectra which we have assigned to a Fe-H complex. The trap is only observed when a high concentration of hydrogen is present in the near surface region. The trap concentration is higher in samples with a higher concentration of single interstitial Fe atoms. The defect has a deep donor level at E_v + 0.31 eV. Direct measurements of capture cross section of holes have shown that the capture cross section is not temperature dependent and its value is 5.2×10^{-17} cm^2. It is found from an isochronal annealing study that the Fe-H complex is not very stable and can be eliminated completely by annealing for 30 minutes at 125 ^{o}C.

8.2. Introduction

Iron is a common impurity in silicon for photovoltaic applications [1]. It is one of the most harmful contaminants and has a strong detrimental effect on solar cell performance[1]-[3]. The most energetically favorable location for a single Fe atom in the Si lattice is a tetrahedral interstitial site. [4] Interstitial iron (Fe_i) in Si has a donor level at about E_v + 0.38 eV and large capture cross section for electrons that makes it a strong recombination center in p-type Si[1],[5]. Fe_i can diffuse in Si at room temperature and in p-type Si it forms complexes with shallow acceptor dopants[6],[7]. The iron-acceptor complexes can be dissociated upon annealing at temperatures higher than 100 ^{o}C or at room temperature under above band gap illumination [1]. Some cheaper “solar grade” silicon which is widely used for production of solar cells contains higher concentrations of Fe and other metallic impurities compared to “electronic grade” material. Due to the desire to be able to use cheaper silicon feedstock with a higher metallic content the understanding of iron-related defects in the “solar grade” silicon and finding ways of their elimination or passivation is a hot topic of research [8].

For crystalline silicon there are very effective ways to getter Fe, [9] but in multi-crystalline silicon the gettering techniques are less effective due to Fe decoration of grain boundaries and extended defects [10]. For this reason there has been a lot of interest in electrical passivation of Fe. Hydrogen is commonly used to passivate lifetime-limiting defects in silicon and is normally introduced into Si-based photovoltaic devices from the silicon nitride anti-reflection coating [11]. Several groups have used DLTS to examine the effects of hydrogen on Fe in p-type silicon, but with no strong evidence of passivation or formation of Fe-H complexes with deep levels in the gap [12]-[15]. This can be expected taking into account a well-known fact that both interstitial hydrogen and iron atoms are generally positively charged in p-type Si and so the Coulomb repulsion of Fe_i and H prevents the formation of Fe-H complexes. In n-type silicon contaminated with iron, a hole trap with an energy level at about E_v + 0.31 eV was detected and assigned to a Fe-H defect [16]. Ab initio calculations predicted that a Fe-H complex should be stable at room temperature and have a deep donor level at

about E_v + 0.40 eV and a deep acceptor level at about E_c - 0.3 eV [17]. Recently there have been reports of the passivating effect of hydrogen on Fe in multi-crystalline silicon, with some publications showing that H does appear to have a strong and thermally stable passivating effect of iron in multi-crystalline silicon [18],[19]. However this contradicts the conclusions of other studies which show the absence of H-induced Fe passivation [20].

8.3. Experimental Methods

Electronic grade boron doped Cz-Si wafers (~12 Ωcm) were cleaved into ~5cm by 5cm squares. The samples were rubbed with iron (99.95% purity from Testbourne Limited, UK) on the back side and then annealed in air in the temperature range 790-875 ^{o}C in a pre-heated furnace for 24 hours. The heat treatments were followed by rapid cooling (below 200 ^{o}C in <10 s) to room temperature.[21] A surface iron silicide is formed as a result of this process [22] and is removed with a planar etch comprising HF (40%), HNO_3 (69%), and CH_3COOH (glacial) in the ratio 8:75:17. Samples were subjected to an HF dip, followed by an RCA clean and hydrogen was then introduced into the wafer from a silicon nitride layer grown by direct plasma enhanced chemical vapour deposition at 350 ^{o}C. The samples were left at room temperature for over a week, cut into smaller pieces, and then the silicon nitride layer was removed with diluted HF (10%). Schottky diodes were formed on the samples by sputtering Ti and Al through a shadow mask and a layer of Au was thermally evaporated onto the back side to form an Ohmic contact. The samples with the Schottky diodes were annealed under vacuum in the temperature range 50-175 ^{o}C with and without reverse bias. After reverse bias annealing (RBA) the samples were cooled down to lower temperatures for electrical measurements with the bias applied. Current-voltage and capacitance-voltage (C-V) measurements were undertaken at different temperatures to check the quality of the diodes, determine the concentration of shallow uncompensated acceptors, and to determine the probing depths for capacitance transient measurements. DLTS and Laplace DLTS (LDLTS) [23] were used to characterize defects with deep electronic levels and determine the concentration of Fe_i related centers.

8.4. Results and Discussion

Fig. 1 shows the conventional DLTS spectra of two different Fe contaminated Si samples before and after annealing for 30 minute at 110 ^{o}C with the applied reverse bias of +5 V. In spectra 1 and 3, taken before the RBA, the only trap that can be detected is one with its DLTS peak maximum at about 56 K. The DLTS signatures {activation energy for hole emission (E_h) and pre-exponential factor (A)} for this trap have been determined from Arrhenius plots of T^2-corrected hole emission rates measured with the use of Laplace DLTS technique as $E_h = 0.10 \pm 0.01$ eV and $A = 1\times10^7$ $s^{-1}K^{-.2}$ These values are close to those reported in the literature for a complex incorporating a substitutional boron atom and an interstitial iron atom (Fe-B) [1],[12],[15]. Concentrations of the Fe-B defect before any annealing steps were determined using DLTS, and in the bulk were $7 \pm 2\times10^{11}$ cm^{-3} in sample Si-Fe1 (spectrum 1) and $1.3 \pm 0.3\times10^{13}$ cm^{-3} in sample Si-Fe2 (spectrum 3) with the concentration reducing closer to the surface. Dissociation of the Fe-B complex upon annealing at temperatures higher than 100 ^{o}C is known to result in the appearance of single interstitial iron atoms in Fe-contaminated Si samples. Usually the Fe-B $\leftrightarrow$ Fe_i + B reaction in boron-doped Si is fully reversible and it is a common approach to consider the concentration of available single interstitial Fe atoms in a Si:B+Fe sample as equal to the concentration of Fe-B complexes measured after a long enough association period at room temperature [1],[6],[7],[15]. So, in the following we will refer to the above values of concentrations of Fe-B complexes in the un-annealed Si-Fe1 and Si-Fe2 samples as the initial concentrations of single interstitial Fe atoms, [Fe_i].

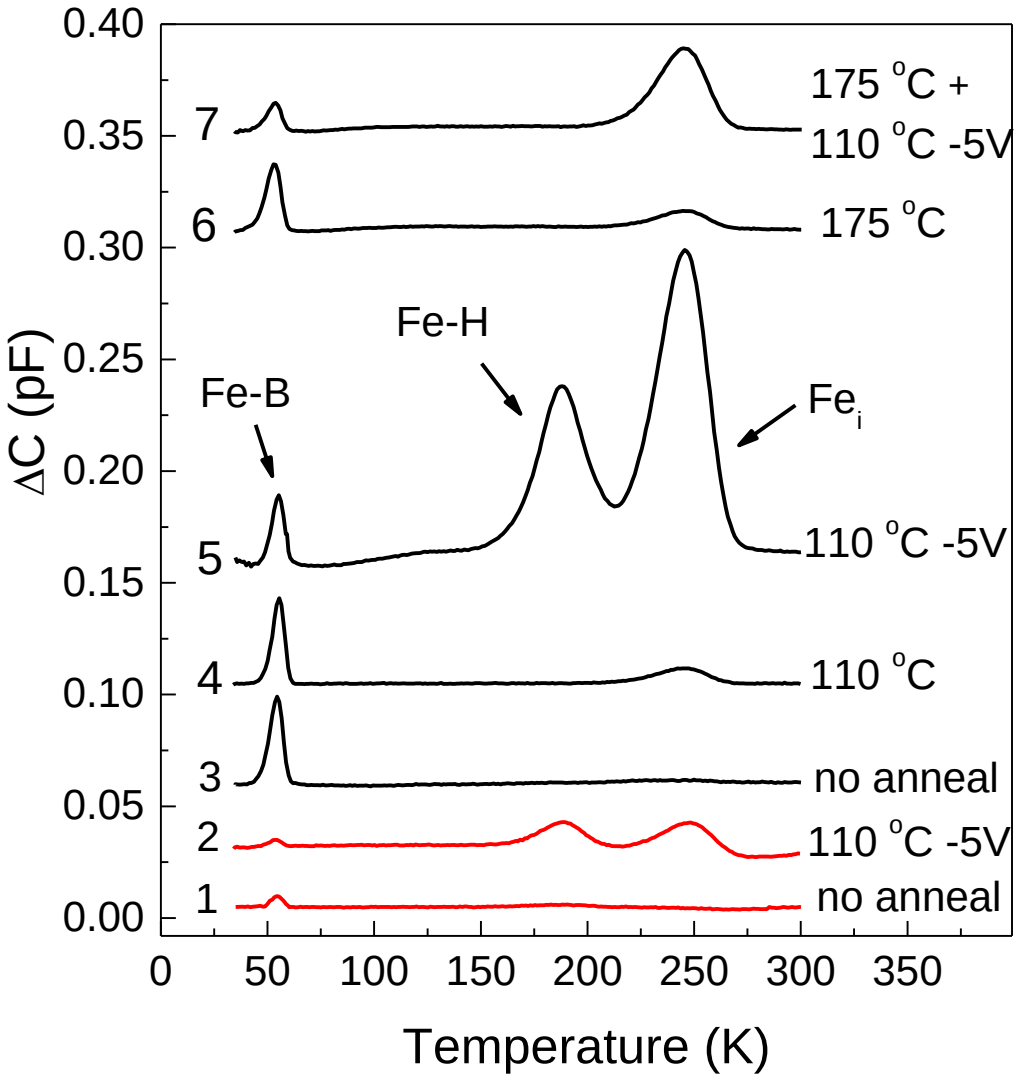

FIG. 1. DLTS spectra of Fe contaminated p-type Cz-Si samples with initial Fe_i concentrations of 7 x 10^{11} cm^{-3} (1,2 in red) and 1.3x10^{13} cm^{-3} (3-7 in black) taken before any annealing (1,3), after a 110 °C anneal (4) after a 110 °C, +5 V, 30 minute RBA (2,5), after a 175 °C 30 minute anneal (6) and after a 175 °C 30 minute anneal followed by a 110 °C, +5 V, 30 minute RBA (7). The measurement conditions were the following: rate window (e_h) = 80 s^{-1}, reverse bias (U_r) = +5 V, filling pulse voltage (U_p) = 0 V, and filling pulse length (t_p) = 1 ms. The peaks in spectra 2 (and 5) are bigger than those in spectra 1 (and 4), due to the change in carrier concentration due to the movement of hydrogen and do not represent an increase in total Fe concentration.

In spectra 2 and 5, recorded after 110 °C RBAs of the Si-Fe1 and Si-Fe2 samples, two other peaks can be seen, one with its maximum at 190 K and the other at 245 K. The DLTS signatures for the trap with its peak maximum at 245 K (E_h = 0.46 ± 0.02 eV and A = 5×10^6 $s^{-1}K^{-2}$) are close to those reported

in the literature for Fe_i [1],[12],[15]. The DLTS signatures for the trap with its peak maximum at 190 K (E_h = 0.31 $\pm$ 0.02 eV and A = 9.3×10^5 $s^{-1}K^{-2}$) do not coincide with the values reported for traps in Fe-contaminated p-type Si but are close to those reported in Ref. 16 for a minority carrier trap detected in Fe-contaminated n-type Si and assigned to a Fe-H complex. From Fig. 1 it can be seen that the magnitude of the peak at 190 K is much bigger in spectrum 5 than in spectrum 2. The only difference between the samples, on which spectra 2 and 5 have been recorded, is the Fe_i concentration, so it can be suggested that the defect responsible for the DLTS peak with its maximum at 190 K is related to Fe. When a Si-Fe2 sample was annealed at 110 ^oC without bias (spectrum 4) there was no peak at 190 K and the magnitude of the peak at 245 K (assigned to Fe_i) was much smaller due to the re-formation of Fe-B pairs during annealing and cooling down.

From comparison of the spectra pairs 1 & 2 and 3 & 5 it might at first appear that the total concentration of defects is higher in the samples subjected to reverse bias annealing. This simple comparison is however misleading because it does not take into account changes in the diode capacitance and depletion width due to the dissociation of B-H complexes and redistribution of hydrogen, as well as the very non-uniform concentration profiles of the Fe-related defects, which are shown in Fig. 2.

Fig. 2 (a) shows the concentration profiles, determined from CV measurements, of uncompensated shallow acceptor centers (N_a^-) induced by different annealing treatments of a Si-Fe2 sample with initial [Fe_i] = 1.3×10^{13} cm^{-3}. The original profile (before annealing) shows a strong drop in N_a^- close to the surface. This is because of the hydrogen passivation of substitutional boron atoms [24]. An analysis of the profile indicates that the concentration of the electrically inactive B-H complexes is over 10^{15} cm^{-3} close to the surface. The B-H complexes dissociate at temperatures higher than 100 ^oC, [24] therefore over 10^{15} cm^{-3} hydrogen atoms can appear in the sub-surface region upon annealing. Fig. 2 shows that reverse bias annealing (110 ^oC, +5V, 30 minutes) has resulted in the hydrogen passivation of boron atoms deeper into the bulk of the silicon sample. This is due to the H

atoms being positively charged, and therefore drifting towards the bulk when under reverse bias and forming the B-H complexes when the sample is cooled down. After the 30 minute 175 ^{o}C anneal with no bias, the hydrogen has been strongly redistributed and its concentration is at least an order of magnitude lower close to the surface (Fig. 2(a)). Spectrum 6 in Fig. 1 has been recorded on a Si-Fe2 sample with initial [Fe_i] = 1.3×10 ^{13} cm^{-3} after a 30 minute 175 ^{o}C anneal under no bias. The spectrum shows mainly the Fe-B-related signal and a small signal due to hole emission from Fe_i. Spectrum 7 has been recorded on the same sample after a subsequent reverse bias annealing (110 ^{o}C, 30 minute, +5V). No peak at 190K is observed in the spectrum. The only difference between spectra 5 and 7 in Fig. 1 is that the sample on which spectrum 5 was recorded has much more hydrogen in the sub-surface region. This indicates that the defect giving rise to the DLTS peak at 190 K can only be formed when there is a large amount of H, and, as we have already demonstrated a correlation with the bulk iron concentration, we therefore assign it to a Fe-H complex.

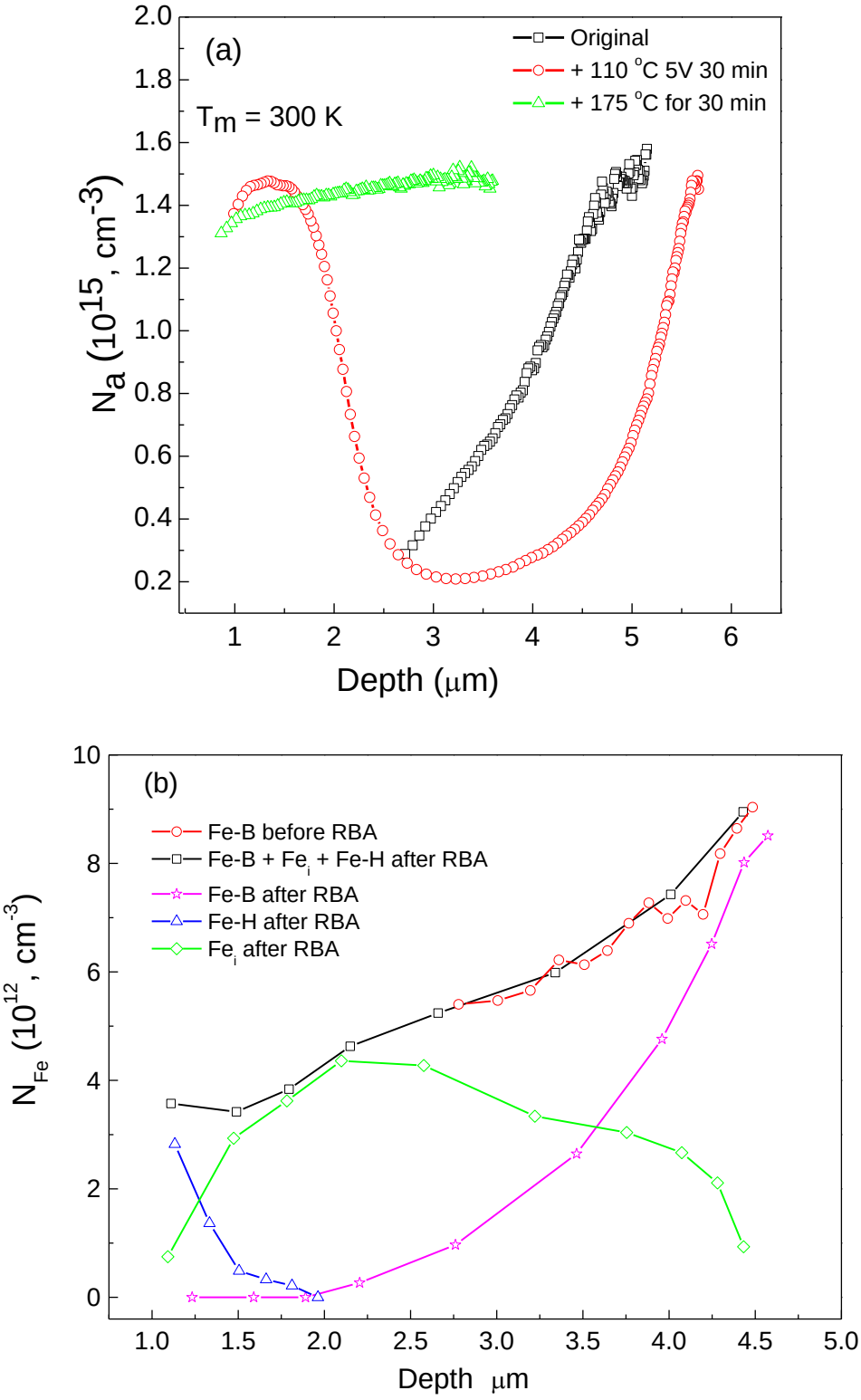

FIG. 2. Concentration depth profiles for Fe contaminated p-type Cz-Si sample with initial [Fe_i] = 1.3x10^{13} cm^{-3} of (a) uncompensated acceptors and (b) Fe-B before a reverse bias anneal, and of Fe-B, Fe_i and Fe-H after a 110 °C, 30 minute, +5V reverse bias anneal. The combined total of all the Fe related centers after the reverse bias anneal is also plotted.

Fig. 2 (b) shows the concentration depth profile of the Fe-B complex before reverse bias annealing and the Fe-B, Fe-H and Fe_i after the RBA. They are derived from CV measurements and LDLTS profiling measurements using a correction based on Debye screening to determine the crossing point of the Fermi level and the trap level (the λ point) [25] at 57 K, 190 K and 250 K respectively. It can be seen that the Fe-H complex concentration is steeply profiled, rising towards the surface. The reasons for this spatial dependency are not fully understood but we note here that the Fe-H formation and dissociation reactions are strongly dependent on the position of the Fermi level. In the bulk p-type region Fe_i is positively charged under the annealing conditions used, making it unlikely that it will react with positively charged H and more likely to form complexes with negatively charged acceptors in this case substitutional boron. However, in the depletion region the Fe_i atoms are neutral and can interact with available H atoms forming Fe-H complexes. Under the annealing conditions the depletion region extends ~2.5μm from the surface and the Fe-H profile is detectable to a depth of ~2 μm. The Fe-H formation rate and equilibrium concentration of the complex depends on the Fermi level position in the depletion and λ regions as well as the hydrogen supply and we hypothesise that these three factors might be responsible for the shape of the profile. By comparing the combined concentrations of Fe-B, Fei and Fe-H after the RBA to the initial concentration of Fe-B before the RBA (Fig. 2(b)) it can be seen that there is no significant change in the total concentration of Fe related centers. This provides further evidence of the center responsible for the DLTS peak at 190 K being associated to a Fe related defect.

Fig. 3(a) shows the conventional DLTS spectra of Si-Fe2 samples with initial $[Fe_i] = 1.3\times10^{13}$ cm^{-3} annealed for 30 minutes under +5V reverse bias at different temperatures in the range from 80 to 120 ^{o}C. The DLTS signal due to the Fe-H complex can be seen to appear after a 90 ^{o}C RBA and has its highest magnitude after the 110 ^{o}C RBA. The peak then starts to diminish after a 120 ^{o}C RBA. In the DLTS spectra of samples subjected to RBAs above 130 ^{o}C the Fe-H complex is not observed at all. The small temperature window and the requirement of annealing under reverse bias for the formation

and existence of the Fe-H complex explains why it has not been observed before. A similar material and similar annealing conditions to those chosen by us were used in Ref.13 but the Fe-H complex was not observed in that study. In that work wet chemical etching was used to introduce hydrogen and the authors measured less than 10^{14} cm^{-3} hydrogen atoms in the subsurface region, which appears not to be enough to create Fe-H complexes. Fig. 3(b) shows how 30 minute isochronal anneals under no bias effect the Fe-H complex created upon reverse bias annealing at 110 ^{o}C. The complex can be seen to disappear completely after a 125 ^{o}C anneal.

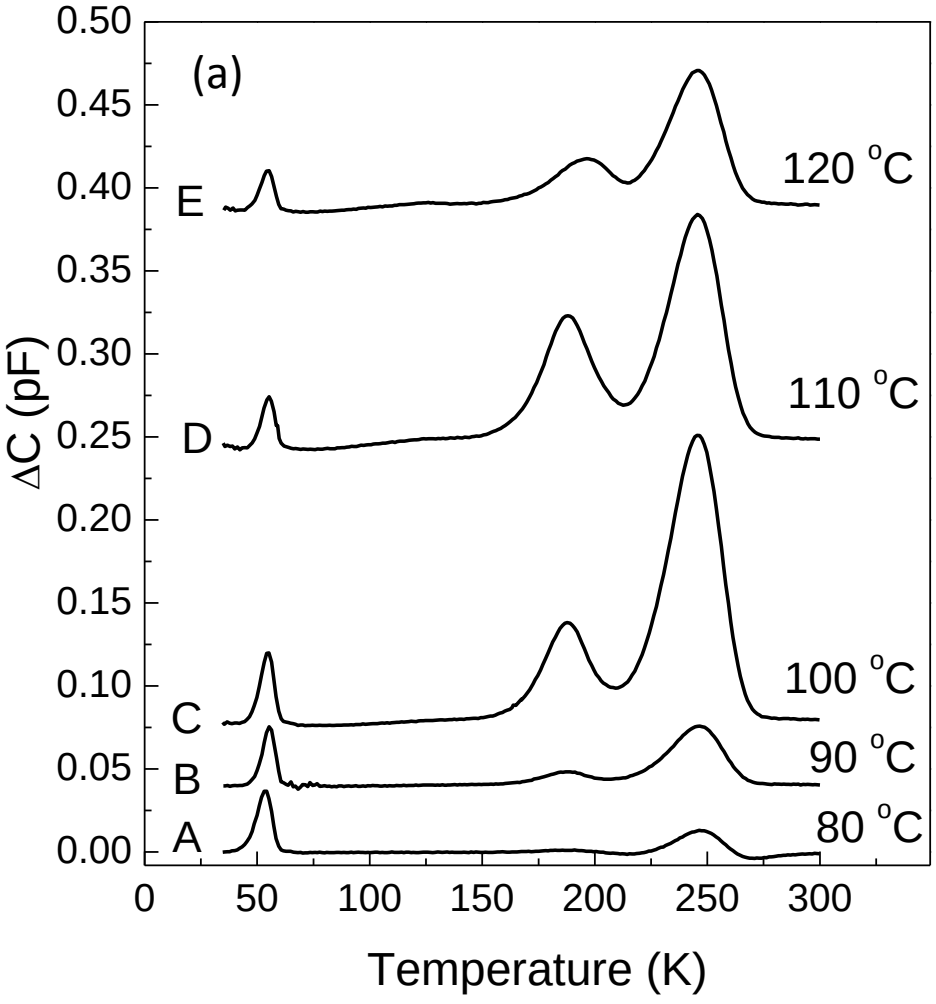

FIG. 3. (a) DLTS spectra of Fe contaminated p-type Cz-Si sample with initial [Fe_i] = 1.3x10^{13} cm^{-3} taken after a 30 minute +5V RBA at (A) 80 ^{o}C, (B) 90 ^{o}C, (C) 100 ^{o}C, (D) 110 ^{o}C and (E) 120 ^{o}C. The measurement conditions were the following: (e_h) = 80 s^{-1}, (U_r) = +5 V, (U_p) = 0 V, and (t_p) = 1 ms.

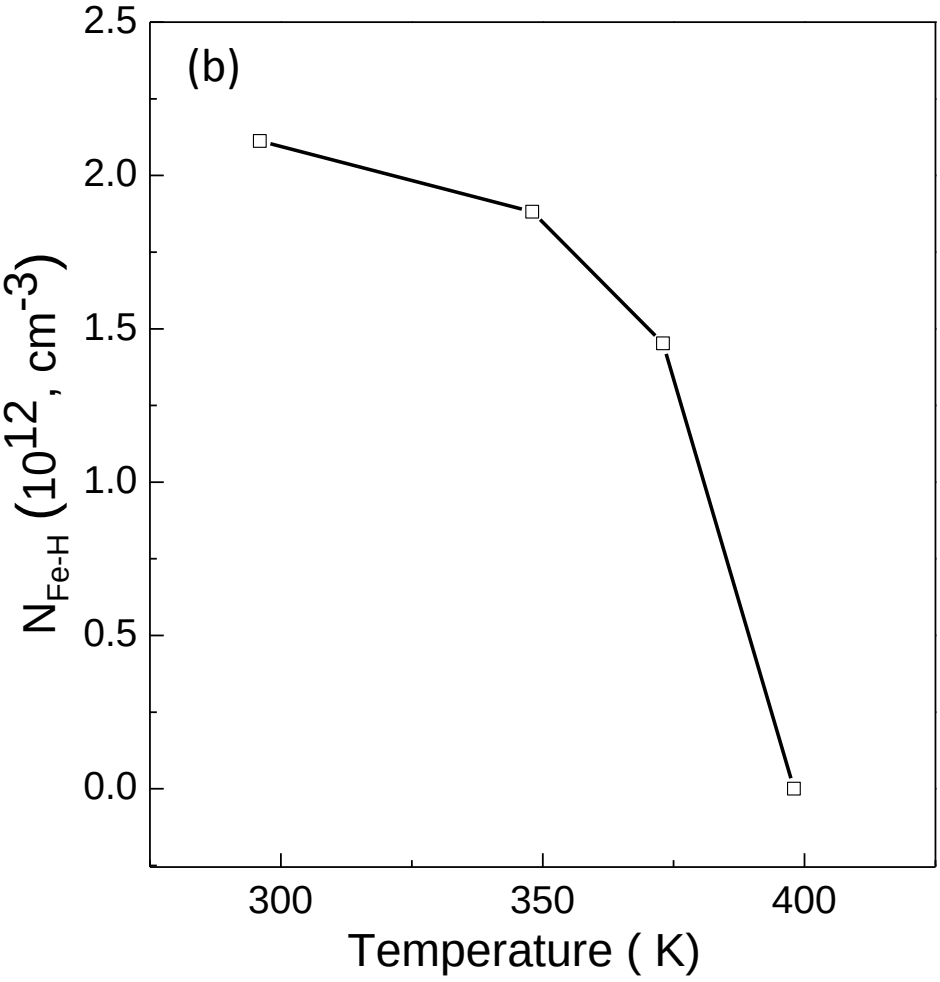

Fig 3. (b) Changes in concentration of the Fe-H complex upon 30 minute isochronal annealing without bias of a Fe contaminated p-type Cz-Si sample with initial [Fe_i] = 1.3x10^{13} cm^{-3} after creation of the complex by a 30 minute, 110 ^{o}C, +5V reverse bias anneal. The given values of Fe-H concentration are averaged concentrations of the complex in the range 1.3 – 2.0 µm below the surface.

An analysis of the total concentration of all electrically active Fe_i-related traps (Fe_i, Fe_i-B, and Fe_i-H) calculated by summing the individual contributions determined from the magnitudes of all three DLTS peaks before and after the different annealing steps has shown that there is no significant change in the total number of the Fe_i related centers and therefore it does not appear that some Fe atoms have been completely electrically passivated. Determining the composition (number of hydrogen atoms incorporated and structure) of the detected Fe-H complex with the use of CV and

DLTS measurements is a difficult task. The ab initio calculations predict that H does not bind with Fe-B pairs and the most energetically favorable Fe-H complex consists of a Fe atom at a hexagonal lattice site with a hydrogen atom bonded to the Fe atom [17]. The activation energy for hole emission from the Fe-H trap determined from an Arrhenius plot of T^2 corrected emission rates has been found to be 0.31 eV, which is in close agreement to the hole ionization energy for a donor level of the Fe-H complex found by ab initio calculations [17]. Direct hole capture cross section measurements have been carried out and show that the capture cross section (σ) is not temperature dependent and its value is 5.2×10^{-17} cm^2. The σ value is within the range of capture cross sections for capture of charge carriers by neutral centers, confirming the donor nature of the level.

A consideration of the electronic properties of Fe_i and H atoms in silicon suggests that these atoms are unlikely to form a pair in the bulk of p-type Si because of their Coulomb repulsion.[26] In the recent study by Liu et al.[19] an almost complete passivation of Fe_i by hydrogen has been reported. The authors have suggested that annealing at 700 ^oC can form negatively charged hydrogen atoms which can then pair with positively charged Fe_i to form stable Fe-H complexes in multi-crystalline silicon. However our results suggest that the Fe-H complex generated during our experiments would dissociate at such high temperatures. Further, the Fe-H complex we have observed has a deep donor level within the band gap, so it can be an effective recombination center. It would seem that the strong decrease in [Fe_i] observed by Liu et al. upon hydrogen introduction at much higher temperatures than we have used could be associated with the formation of a different complex with hydrogen or some other mechanism is involved.

8.5. Conclusion

To conclude, we have presented evidence for a Fe-H complex forming in Fe-contaminated p-type Czochralski silicon upon reverse bias annealing in the temperature range of 90-120 ^{o}C. The complex only forms when there is large amounts of H and its concentration is related to the concentration of Fe_i in the samples. The complex has a deep donor level at E_V + 0.31 eV which is in a good agreement with the value predicted by ab initio calculations [17] and has a direct hole capture cross section of 5.2×10^{-17} cm^2. The complex can be seen to disappear completely after a 125 ^{o}C anneal for 30 minutes. No evidence of total electrical passivation of Fe due to the incorporation of hydrogen has been obtained in this work.

We would like to thank EPSRC (UK) for funding this work via grant EP/K006975/1 at Manchester and via grant EP/J01768X/2 at Warwick.

8.6. References

[1] A. A. Istratov, H. Hieslmair, and E. R. Weber, “Iron and its complexes in silicon,” Appl. Phys. A, vol. 69, pp. 13–44, 1999.

[2] G. Coletti, R. Kvande, V. D. Mihailetchi, L. J. Geerligs, L. Arnberg, and E. J. Ovrelid, “Effect of iron in silicon feedstock on p- and n-type multicrystalline silicon solar cells,” J. Appl. Phys., vol. 104, no. 10, p. 104913, 2008.

[3] R. Kvande, L. J. Geerligs, G. Coletti, L. Arnberg, M. Di Sabatino, E. J. Ovrelid, and C. C. Swanson, “Distribution of iron in multicrystalline silicon ingots,” J. Appl. Phys., vol. 104, no. 6, p. 064905, 2008.

[4] S. K. Estreicher, M. Sanati, and N. G. Szwacki, “Fundamental Interactions of Fe in silicon : First-Principles Theory,” Solid State Phenom., vol. 133, pp. 233–240, 2008.

[5] K. Wunstel and P. Wagner, “Iron-Related Deep Levels in Silicon,” Solid State Commun., vol. 40, pp. 797–799, 1981.

[6] G. Zoth and W. Bergholz, “A fast, preparation-free method to detect iron in silicon,” J. Appl. Phys., vol. 67, no. 11, p. 6764, 1990.

[7] W. Wijaranakula, “The Reaction Kinetics of Iron-Boron Pair Formation and Dissociation in P-Type Silicon,” J. Electrochem. Soc., vol. 140, no. 1, p. 275, 1993.

[8] J. Hofstetter, J. F. Lelièvre, C. del Cañizo, and A. Luque, “Acceptable contamination levels in solar grade silicon: From feedstock to solar cell,” Mater. Sci. Eng. B, vol. 159–160, pp. 299–304, Mar. 2009.

[9] S. P. Phang and D. Macdonald, “Direct comparison of boron, phosphorus, and aluminum gettering of iron in crystalline silicon,” J. Appl. Phys., vol. 109, no. 7, p. 073521, 2011.

[10] A.R. Peaker, V. P. Markevich, B. Hamilton, G. Parada, A. Dudas, A. Pap, E. Don, B. Lim, J. Schmidt, L. Yu, Y. Yoon, and G. Rozgonyi, Phys. Status Solidi A, 209, 1884-1893, (2012).

[11] F. Jiang, M. Stavola, A. Rohatgi, D. Kim, J. Holt, H. Atwater, and J. Kalejs, “Hydrogenation of Si from SiN (H) films: Characterization of H introduced into the Si,” Appl. Phys. Lett., vol. 83, no. 5, p. 931, 2003.

[12] S. J. Pearton and A. J. Tavendale, “Electrical properties of deep silver- and iron-related centres in silicon,” j. phys. C Solid State Phys, vol. 17, pp. 6701–6710, 1984.

[13] O. V Feklisova, A. L. Parakhonsky, E. B. Yakimov, and J. Weber, “Dissociation of iron-related centers in Si stimulated by hydrogen,” Mater. Sci. Eng. B, vol. 71, pp. 268–271, 2000.

[14] M. Kouketsu and S. Isomae, “Hydrogen passivation of iron-related hole traps in silicon,” J. Appl. Phys., vol. 80, no. 3, p. 1485, 1996.

[15] C. K. Tang, L. Vines, B. G. Svensson, and E. V. Monakhov, “Interaction between hydrogen and the Fe-B pair in boron-doped p-type silicon,” Appl. Phys. Lett., vol. 99, no. 5, p. 052106, 2011.

[16] T. Sadoh, K. Tsukamoto, A. Baba, D. Bai, A. Kenjo, T. Tsurushima, H. Mori, and H. Nakashima, “Deep level of iron-hydrogen complex in silicon,” J. Appl. Phys., vol. 82, no. 8, p. 3828, 1997.

[17] M. Sanati, N. Szwacki, and S. Estreicher, “Interstitial Fe in Si and its interactions with hydrogen and shallow dopants,” Phys. Rev. B, vol. 76, no. 12, p. 125204, Sep. 2007.

[18] B. J. Hallam, P. G. Hamer, S. R. Wenham, M. D. Abbott, A. Sugianto, A. M. Wenham, C. E. Chan, G. Xu, J. Kraiem, J. Degoulange, and R. Einhaus, “Advanced Bulk Defect Passivation for Silicon Solar Cells,” IEEE J. Photovoltaics, vol. 4, no. 1, pp. 88–95, 2014.

[19] A. Liu, C. Sun, and D. Macdonald, “Hydrogen passivation of interstitial iron in boron-doped multicrystalline silicon during annealing,” J. Appl. Phys., vol. 116, no. 19, p. 194902, Nov. 2014.

[20] P. Karzel, A. Frey, S. Fritz, and G. Hahn, “Influence of hydrogen on interstitial iron concentration in multicrystalline silicon during annealing steps,” J. Appl. Phys., vol. 113, no. 11, p. 114903, 2013.

[21] J. D. Murphy and R. J. Falster, “Contamination of silicon by iron at temperatures below 800 °C,” Phys. status solidi – Rapid Res. Lett., vol. 5, no. 10–11, pp. 370–372, Nov. 2011.

[22] J. D. Murphy and R. J. Falster, “The relaxation behaviour of supersaturated iron in single-crystal silicon at 500 to 750 °C,” J. Appl. Phys., vol. 112, no. 11, p. 113506, 2012.

[23] L. Dobaczewski, P. Kaczor, I. D. Hawkins, and a. R. Peaker, “Laplace transform deep-level transient spectroscopic studies of defects in semiconductors,” J. Appl. Phys., vol. 76, no. 1, p. 194, 1994.

[24] C. T. Sah, “Deactivation of the boron acceptor in silicon by hydrogen,” Appl. Phys. Lett., vol. 43, no. 2, p. 204, 1983.

[25] D. Stievenard and D. Vuilaume, Profiling of defects using deep level transient spectroscopy, J. Appl. Phys. Vol. 60, p. 973 (1986).

[26] T. Heiser and A. Mesli, “Charge-State-Dependent diffusion and carrier-emission-limited drift of iron in silicon,” Phys. Rev. Lett., vol. 68, p. 978, 1992.

Paper 4

Molybdenum nano-precipitates in silicon: A TEM and DLTS study

S. Leonard, V. P. Markevich, A. R. Peaker, B. Hamilton, K. Youssef, and G. Rozgonyi

Phys. Status Solidi, vol. 251, no. 11, pp. 2201–2204, 2014.

9. Molybdenum nano-precipitates in silicon: a TEM and DLTS study

9.1.Abstract

The quest for low cost solar cells has resulted in attempts to use lower purity silicon rather than conventional electronic grade material. The metallic content of such ‘solar silicon’ is usually much higher than electronic grade material and this compromises the efficiency of photovoltaic conversion via a variety of recombination mechanisms. Molybdenum is a common metallic contaminant in Si which is difficult to getter because of its low diffusivity. It is known that Mo incorporates into the Si lattice as single interstitial atoms, introducing a deep donor level into the gap. In this work we show that Mo in silicon can also form nano-precipitates which may represent a new general class of efficient recombination centers. We have observed the Mo precipitates by TEM as 5 to 10 nm clusters in Si samples into which molybdenum was introduced during growth or by ion implantation and annealing. In general, such precipitates can form in Si samples containing metals with low diffusivity during high-temperature treatments and subsequent cooling. We report the carrier capture and emission properties of Mo nano-precipitates, which show that these could be very effective recombination centers for minority carriers in p-type Si. In particular we present data and analysis of minority carrier charge exchange at these nano-dimension metallic defects.

9.2.Introduction

Precipitates have often been observed in silicon but are normally associated with the heavy 3d transition metals with high solubility and diffusivity such as copper. However these precipitates are normally very large and although they can be detrimental due to causing shunts across a junction, they tend to have very little electrical activity [1]. The lighter transition metals such as molybdenum are generally thought to act as point defect recombination centres and not to precipitate, but in this paper we will show evidence that molybdenum can actually form small “nano-precipitates” under thermal conditions and concentrations similar to those used in the manufacturing of solar cells from solar grade silicon. We will also show that these can act as powerful recombination centres, unlike traditional larger precipitates.

9.3.Physical structure of Mo nano-precipitates

We report here measurements on epitaxial silicon layers doped during growth with about $3x10^{13}$ molybdenum atoms and about $1.5x10^{15}$ boron atoms and on Czochralski Si samples implanted with molybdenum. Mo was introduced into p type silicon with 3 Ωcm resistivity by 2 MeV implantation with a $5x10^{12}$ cm^2 dose. The Mo-implanted samples were annealed in the range 700 ^oC to 900 ^oC to remove the implant damage and activate the molybdenum. We have chosen molybdenum to study the behavior of these precipitates because it is a known contaminant of cast solar silicon at concentrations up to 10^{13} cm^{-3} [2] and is present in electronic grade epitaxial silicon after certain growth procedures [3]. The samples contain small precipitates which we associate with molybdenum and refer to as Mo nano-precipitates. Figure 1 shows a high resolution transmission electron microscope (TEM) image which shows the presence of nano precipitates in the epitaxially grown samples.

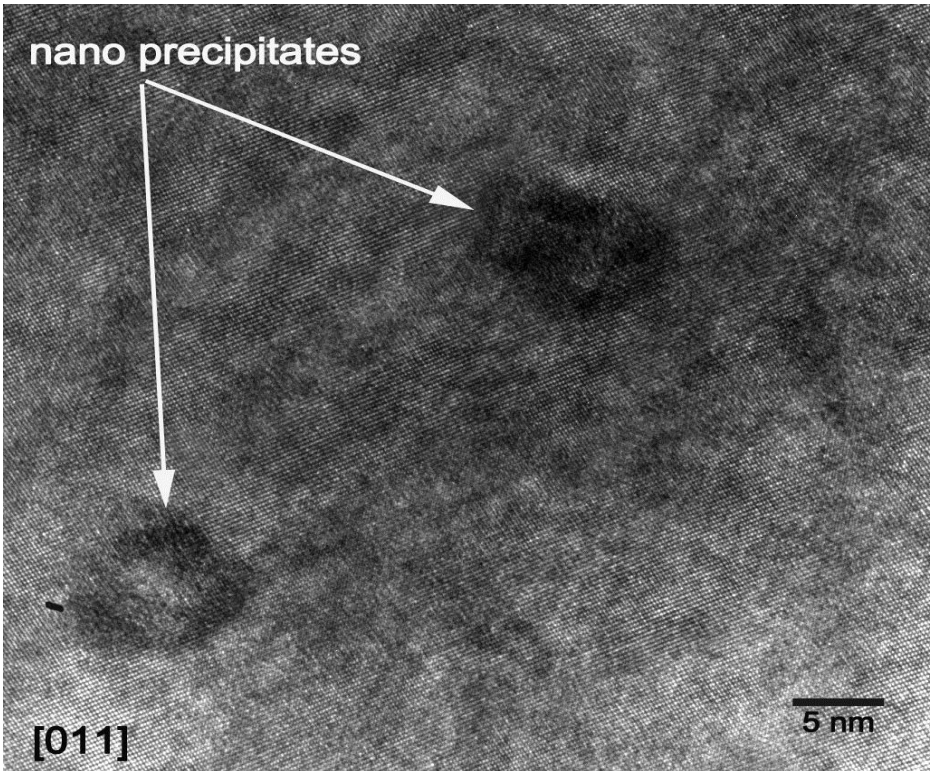

Figure 1. High resolution Transmission Electron Microscopy image of molybdenum nano-precipitates.

Further chemical analysis of the nano-precipitates has been undertaken using a Titan electron microscope. A combination of high-angle annular dark field (HAADF) and energy-dispersive X-ray (EDX) measurements has provided conclusive evidence that the precipitates contained molybdenum although it has not as yet given us an exact chemical identity.

Figure 2 shows a lattice image taken from the Titan of one on the nano-precipitates located 800 nm from the surface, shown by a lighter patch on the image. The image to the right of it shows the HAADF analysis and the green dots show that Mo exists in the precipitate.

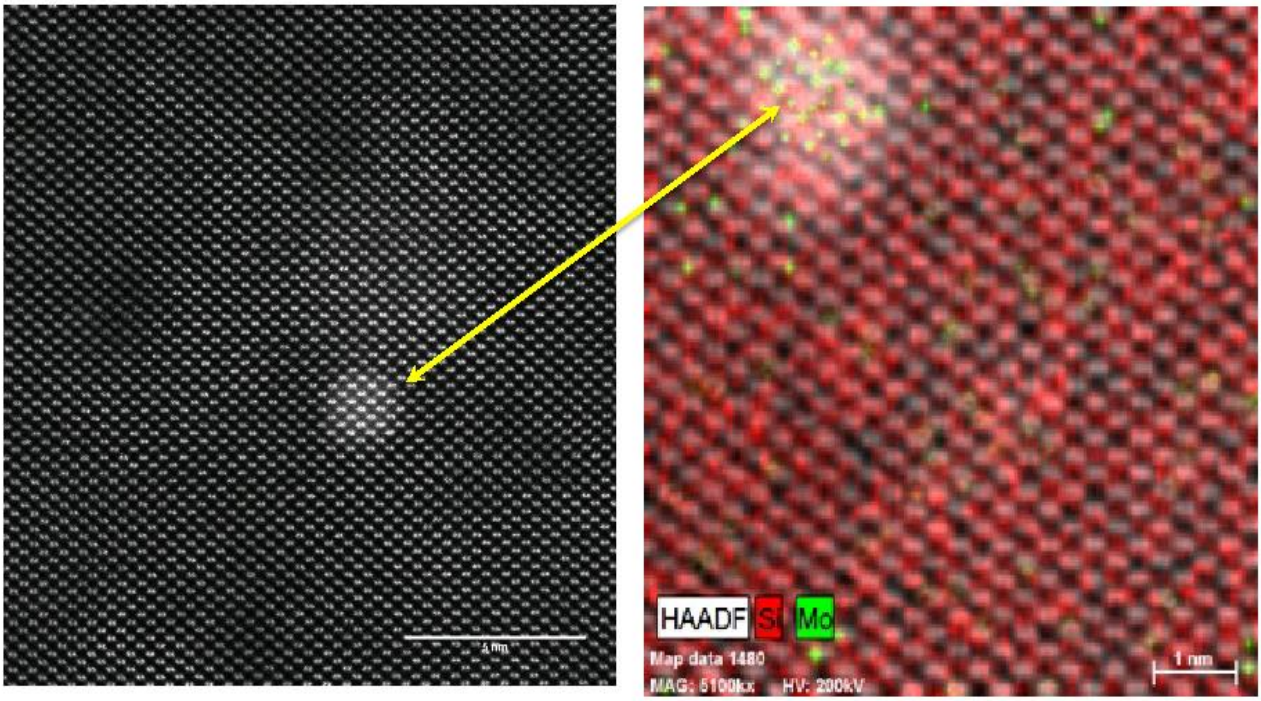

Figure 2. Lattice image of a Mo nano-precipitate and analytical image. Silicon atoms are shown in red and Mo in green. The scale marker in the left figure is 5 nm and at the right 1 nm.

There are several different molybdenum silicide compositions which are stable at annealing temperatures used in this work and in common silicon ingot casting such as Mo_3Si (cubic), Mo_5Si_3 (tetragonal) and $MoSi_2$ (tetragonal). The disilicide is known to grow on a silicon surface epitaxially in the (100) plane [4] so is a likely candidate. However we do not yet have enough information to conclusively define exactly what the precipitates structure is.

9.4.Electronic measurements and properties

Schottky diodes were formed on the samples by sputtering Ti/Al through a shadow mask and a layer of Au was thermally evaporated onto the back side to form an Ohmic contact. Current-voltage and capacitance voltage (C-V) measurements were undertaken to check the quality of the diodes and determine the concentration of shallow uncompensated acceptors, and work out the probing depth for capacitance transient measurements. DLTS and Laplace DLTS (LDLTS) [5] were used to characterize defects with deep electronic levels. The conventional DLTS spectra are shown in figure

3, comparing the p-type epitaxially grown sample doped with molybdenum with another sample with no molybdenum doping (blue spectrum).

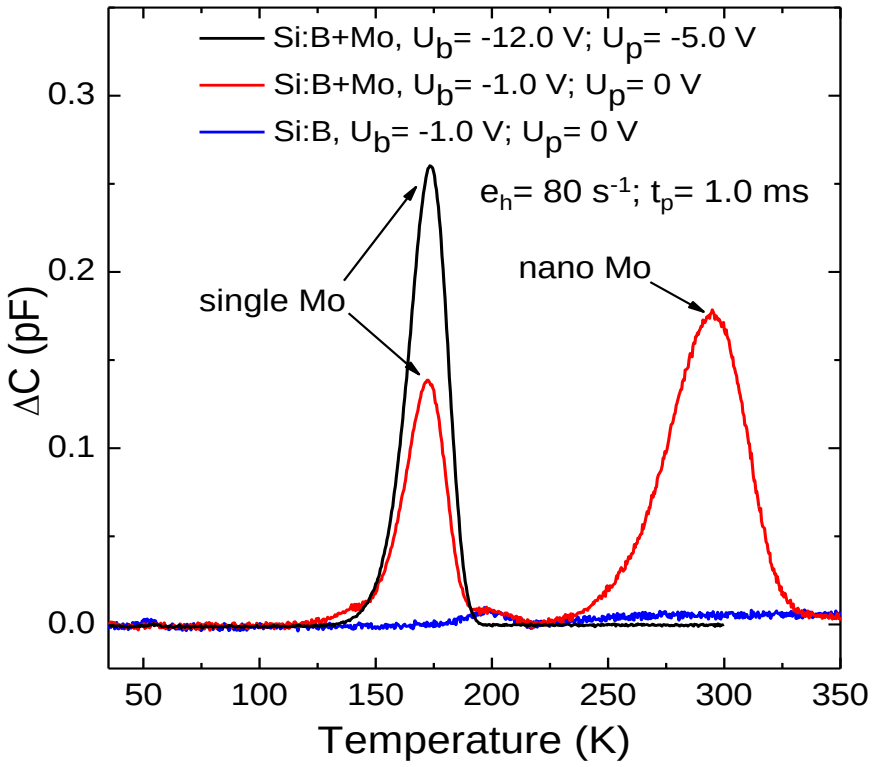

Figure 3. DLTS scan of a p-type silicon layer doped with Mo during epitaxy (red) compared to a layer with no molybdenum doping (blue).

The large peak at around 175 K is a peak that has previously been related to single molybdenum atoms in solution [6, 7] and an Arrhenius plot confirmed it was the same peak. Measurements at different biases enable us to profile the concentration of the Mo-related defects as a function of depth. The DLTS spectra recorded with two biases are shown as red and black spectra in figure 3. The spectrum shown in black relates to a region of a few microns into the bulk of the sample and only shows the peak with its maximum at about 175 K, which is related to single molybdenum atoms in solution. The spectrum in red relates to a region around 1µm from the surface and shows two peaks. The first is the same as before at 175 K with a trap concentration of about 10^{13} cm^{-3} atoms,

but the second at around 298 K is a new peak that has not been observed before and we believe relates to the nano-precipitates. These new hole traps are found exclusively in the region where the molybdenum precipitates were found in the TEM images. The activation energy of hole emission from the nano precipitates was determined as Ev + 0.47 eV from an Arrhenius plot meaning the defect possess a mid gap energy level and could be an effective recombination site. The implanted samples had slightly different DLTS spectra to the epitaxially grown samples. We believe this could be due to the formation of larger precipitates in the implanted samples due to a higher concentration of Mo. There will also be an increase in the concentration of vacancies caused by the implantation which could alter the formation of precipitates. Different size and shape precipitates are likely to have different electrical characteristics in DLTS. TEM images of the implanted samples will be taken in the near future which will give us a better idea of the formation and size of the molybdenum precipitates in the implanted material.

Figure 4 shows the majority carrier capture measurement of the two peaks seen in figure 3. The capture behaviour of the nano-precipitates looks very similar to that of a point defect and not like to those for traditional larger precipitates, which show specific capture behaviour dependant on the electronic structure [8]. However the value of majority carrier capture cross section is very small, of only 2.2×10^{-19} cm^2.

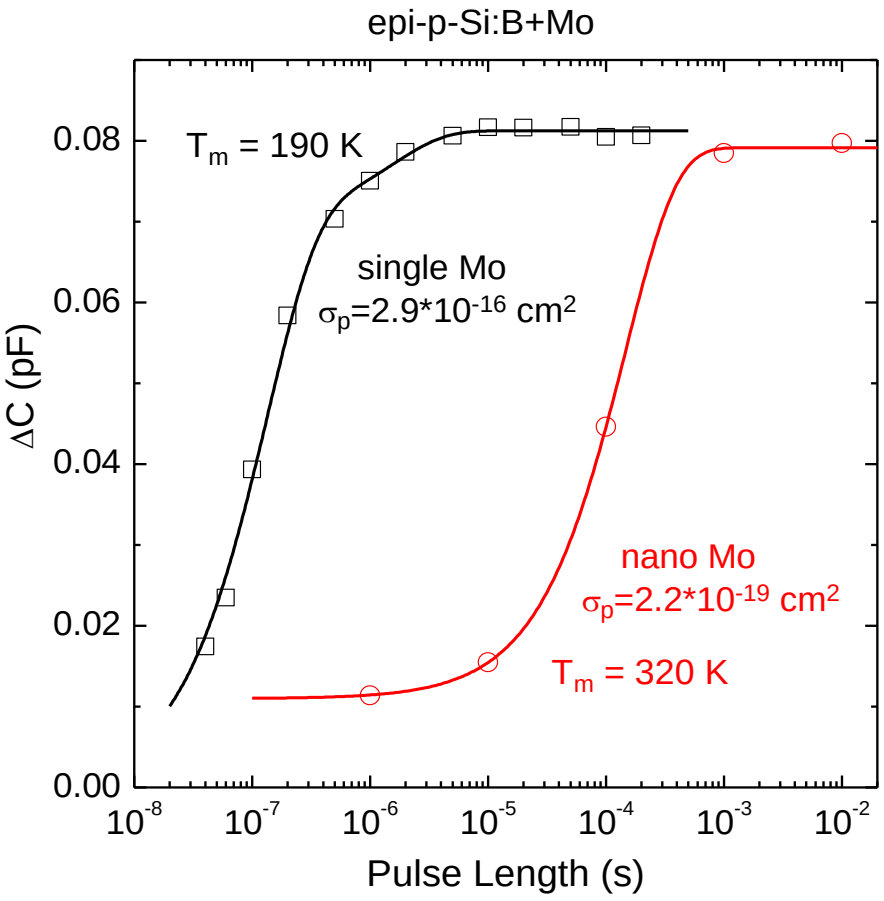

Figure 4. Majority carrier capture behaviour of the isolated Mo defect and the nano-precipitates.

Minority carrier capture cross section was measured with the ion implanted samples using minority carrier transient spectroscopy [9] and found to be very large (~10^{-14} cm^{-3}), suggesting this could be an extremely powerful recombination centre for minority carriers. It is likely that there is Coulombic attraction of the minority carriers to the nano-precipitate and that the nano-precipitate will act quite differently to a normal point defect in solution.

9.5. SIMS results

Secondary Ion Mass Spectrometry (SIMS) measurements were taken from both the epitaxially grown samples and the samples implanted with 5 x 10^{12} cm^{-2} atoms of molybdenum and subsequently annealed at 700 ^{o}C and 900 ^{o}C for 30 minutes in N_2 gas. The epitaxially grown samples had molybdenum in quantities below the detection limit of SIMS for molybdenum. The results for the implanted samples (into which a lot more molybdenum was introduced) along with DLTS concentration profiles are shown in figure 5. The precipitates can be seen to be confined to the region of Mo peak concentration. Typically a sharpening of the SIMS peaks is observed in ion-implanted samples in which a layer with precipitates is formed upon annealing [10]. However this cannot be observed in figure 5 and is probably due to the fact that the precipitates are very small, so the atoms would be only moving a matter of nanometres to form the precipitates. There appears to be practically no movement of the molybdenum atoms upon annealing. That indicates low diffusivity of Mo in Si at 900 ^{o}C and shows why Mo is so difficult to getter. The electrical measurements show much smaller concentrations of electrically active defects than the SIMS measurements of molybdenum. This can be considered as an indication of molybdenum precipitation assuming that a nano-precipitate of a few hundred atoms acts as a trap for one or two charge carriers.

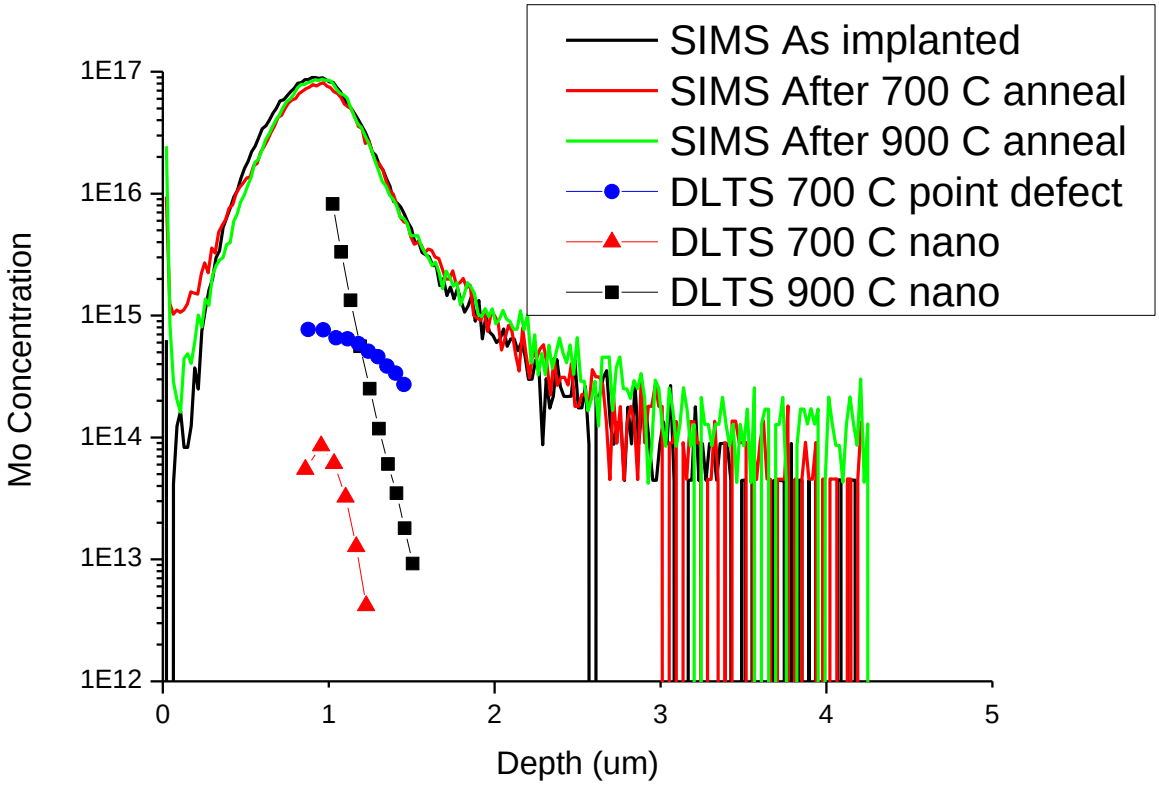

Figure 5. SIMS and DLTS concentration profile measurements of Molybdenum in silicon.

9.6. Conclusions

Very small molybdenum nano-precipitates in the order of 2-10 nm have been observed in both TEM and electrical measurements of intentionally contaminated silicon. The nano-precipitates appear to be very powerful recombination centres with a mid-gap energy level and very large minority carrier capture cross sections. They are a new class of recombination centres with different physics to traditional point defect impurities and larger precipitates and dislocations. It is very possible that such precipitates occur for many of the metals with low diffusivities, and could form in growth processes for cast solar silicon. We suspect that the phase of the precipitate is tetragonal $MoSi_2$ which is extremely stable once formed and would not be removable without re-melting. As the agglomeration of the Mo creates very powerful recombination centres this would mean they could have a large effect on solar efficiency.

9.7. Acknowledgements

We would like to thank EPSRC (UK) for the funding. Professor Russel Gwilliam of the Surrey Ion Beam centre is thanked for undertaking the Mo Implants. The SIMS measurements were undertaken by Dr. Alison Chew of Loughborough Surface Analysis Ltd, UK.

9.8. References

[1] A.R. Peaker, V. P. Markevich, B. Hamilton, G. Parada, A. Dudas, A. Pap, E. Don, B. Lim, J. Schmidt, L. Yu, Y. Yoon, and G. Rozgonyi, Phys. Status Solidi A, 209, 1884-1893, (2012).

[2] T. Buonassisi1, A. A. Istratov, M. D. Pickett, M. Heuer, J. P. Kalejs, G. Hahn, M. A. Marcus, B. Lai, Z. Cai, S. M. Heald, T. F. Ciszek, R. F. Clark, D. W. Cunningham, A. M. Gabor, R. Jonczyk, S. Narayanan, E. Sauar and E. R. Weber, Prog in Photovoltaics; Res Appl, 14, 513-531, (2006).

[3] M.L. Polignano C. Bresolin, G. Pavia, V. Soncini, F. Zanderigo, G. Queirolo and M. Di Dio, Materials Sci. Eng. B53, 300-309, (1998).

[4] A. Perio and J. Torres, J. Appl. Phys., 59, 2760- 2764, (1986)

[5] L. Dobaczewski , A.R. Peaker, K. Bonde Nielson, J. Appl. Phys., 96, 4689-4728, (2004).

[6] A. Rohatgi, R. H. Hopkins, J. R. Davis, R. B. Campbell, and H. C. Mollenkopf, Solid-State Electronics, 23, 1185, (1980).

[7] J. L. Benton, D. C. Jacobson, B. Jackson, J. A. Johnson, T. Boone, D. J. Eaglesham, F. A. Stevie, and J. Beccero, J. Electrochem. Soc., 146, 1929 (1999).

[8] M. Seibt, M. Griess, A. A. Istratov, H. Hedemann, A. Sattler and W. Schröder, Phys. Solidi. A, 166, 171 (1998).

[9] B. Hamilton, A.R. Peaker, D.R. Wright, J. Appl. Phys., 50, 6373, (1979).

[10] K. J. Dudeck, E. Huante-Ceron, A. P. Knights, R. M. Gwilliam and G. A. Botton, Semiconduct. Sci. Technol., 28, 125012, (2013).

Paper 5

Electron Capture and Emission at Nanoscale Transition Metal Precipitates in Semiconductors

J. Jacobs, S. Leonard, V. P. Markevich, A. R. Peaker and B. Hamilton

Submitting to Phys. Rev. Lett. ~10/2015

10. Electron-hole recombination at metallic nano-precipitates: implications for silicon solar energy conversion

10.1. Abstract

The efficiency of solar energy conversion by multi-crystalline silicon PV cells is critically dependent on the nature of the electronic defects within the material. There is growing evidence that very small transition metal (TM) precipitates (sub-10nm diameter) are especially effective at promoting electron-hole recombination and so degrading efficiency. Metallic precipitates, in equilibrium, carry a surface charge which is attractive for capture of optically injected minority carriers but repulsive for majority carrier capture; the latter process may then limit the recombination at the precipitate ensemble. By fabricating molybdenum nano-precipitate doped silicon, with low background carrier density we were able to measure directly the particle capture cross-sections of these defects. In the size regime 3-10 nm, it was determined that the narrowing of repulsive potential surrounding the metallic surface enhances tunnelling mediated majority carrier capture by several orders of magnitude and these observations help to explain the potential importance of TM nanoprecipitates in limiting cell efficiency.

10.2. Introduction

The development of sustainable and renewable energy conversion systems has become the focus of intense research activity worldwide. In the field of solar energy conversion this involves, for example, the fundamental examination of energy and charge transfer processes in photovoltaic (PV) materials [1] [2]. Currently silicon based technology supplies more than 90% of the world's PV generated electricity and this is likely to remain the case for at least two decades. The ability to manufacture large area Si PV systems, with a low thermal and carbon emission budgets whilst maintaining high solar energy conversion efficiency will be of paramount importance if the aspiration to supply 16% of the world's electricity from photovoltaics by the year 2050 is to be met [3] [4]. The low cost Si, most commonly multi-crystalline (MC) Si, used in PV cell manufacture does not have the high level of purity associated with electronic grade silicon and often contains transition metal (TM) impurities which are well known to play a dominant role in efficiency reduction by promoting fast electron-hole recombination, degrading the ability of the PV cell to collect photo excited electrons [5].

Mechanisms for removing or re-siting TMs within the PV cell structure are routinely employed in cell manufacture, usually in the form of "gettering" methods which use thermal cycling to drive TMs into widely separated (e.g. surface or grain boundary) regions leaving much of the volume relatively un-contaminated and able to perform energy conversion with an efficiency close to 20%. A scaling down of the thermal budget for cell manufacture in order to reduce both the carbon emission footprint and the $/W figure will inevitably impact on the ability to remove TM related defects, since both defect formation and diffusion are temperature sensitive processes. High spatial resolution X-ray fluorescence experiments have shown that small (sub 30 nm) TM precipitates degrade the minority carrier diffusion length and are thus likely to play an important role in efficiency degradation of multi-crystalline cells [6]. Recent x-ray fluorescence data have confirmed that 10 nm size Cr precipitates form in MC silicon [7]. It is becoming clear that nanoscale

TM clusters, precipitated during the processing of MC silicon may exert a strong influence on the efficiency of the solar energy conversion process, and for future MC solar silicon spatial control of such nano-precipitates will be essential.

Metallic nano-precipitates are at first sight unlikely candidates for promoting fast electron-hole recombination which requires efficient, sequential, capture of majority and minority carriers. Such objects will form a three dimensional electrically floating, nanoscale Schottky barrier (SB) with the semiconductor matrix; in thermal equilibrium they will become charged in accordance with Schottky-Mott theory. The equilibrium surface charge distribution generates a Debye screened Coulomb potential which is attractive to the minority carriers but repulsive to majority carriers. This suggests that metallic precipitates would possess highly asymmetric capture cross-sections and exhibit fast minority carrier trapping but not fast electron-hole recombination. Recombination would be “bottle-necked” by this slow, repulsive, capture transition of the majority carriers [8].

10.3. Experimental Methods

The present work was motivated by the need to directly measure carrier capture at TM nano-precipitates in Si, in order to help understand why such defects degrade the solar energy conversion process. High purity single crystal material was used to form a model system into which a specific TM, molybdenum was incorporated, both by ion implantation and by doping during epitaxial growth. Mo is a slow diffusing TM and a common contaminant in Si which is known to produce isolated point defects with energy levels deep in the forbidden gap of p-type Si; structurally, these have been linked to interstitial Mo atoms [9] [10], and shown to degrade solar energy conversion. In addition, it has been established that Mo nano-precipitates also readily form in Si. These are typically small (few nm radii), result from diffusion limited growth and have been directly imaged in single crystal Si using transmission electron microscopy in the electron energy loss mode [11]. TEM images and a distinct electrical signature for Mo nano-precipitates, in the form of a broadened high temperature DLTS spectral feature, have also been established on samples similar to those studied in this work

[12]. In our model materials system we were thus able to study both the dispersed point defect and precipitated Mo populations which co-exist and interact within the solid. We have used secondary ion mass spectrometry (SIMS) and deep level transient spectroscopy (DLTS) to measure, respectively, the atomic and electrically active (deep energy level) concentrations associated with the presence of the Mo. The transient capacitance data derived from DLTS allows direct measurement of electron and hole capture cross sections which determine the significance of a defect or impurity as a channel for carrier recombination and ultimately its likely impact on solar cell efficiency. We determine that majority carrier capture, mediated by phonon assisted tunnelling, is strongly enhanced by size dependent narrowing of the repulsive potential: cross section enhancement by several orders of magnitude is measured. We further determine that, unlike the macroscopic equivalent case, image force barrier lowering is both enhanced and size dependent in the few nm regime which further increases the capture rate. The inverse charge exchange process (majority carrier emission) is also influenced by these factors and this sensitivity to the form of potential surrounding the nano-precipitate leads to size dependency of the emission rate.

Our measurements and supporting calculations are based on fundamental electrostatic principles; they suggest that sub 5 nm diameter metallic nano-precipitates in semiconductors constitute a distinct type of defect species capable of producing efficient electron-hole recombination and significantly influence carrier lifetimes and PV conversion efficiencies**.**

Results and Discussion

We report here data obtained from p-type Si, which is most commonly used for PV technology. Epitaxial material containing Mo nano-precipitates as a result of Mo incorporated during growth and also boron doped Czochralski (Cz) silicon ion-implanted with Mo, were studied. The principle experimental measurement was of hole and electron capture and emission rates associated with the nano-precipitates using DLTS. These transition processes studied are summarised in figure 1.

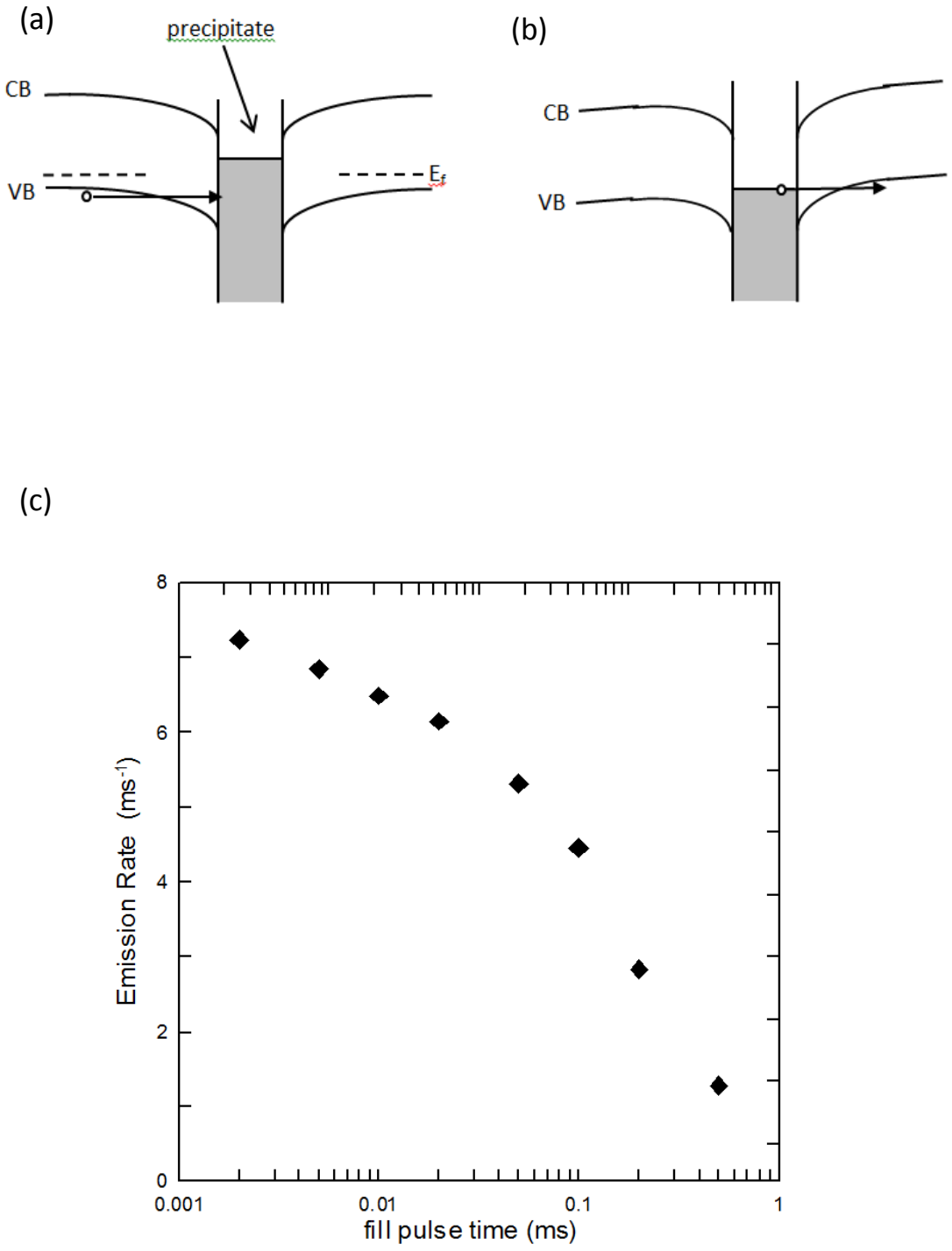

Figure 1. **(a) The energy barrier configuration for hole capture into the single hole deficient N-1 charge state; the degree of non-alignment between the metal and semiconductor Fermi energies is a strong function of the Coulomb charging energy for small systems. (b) Hole emission occurs from equilibrium charge state, N, but in a depletion field. The external potential drop is small (≈40 meV) owing to the limited spatial extent of the precipitate potential .(c) Illustrates that the shortest fill pulses yield the fastest emission rates, consistent with a size distribution of precipitates.**

Such measurements permit spectral separation of the contribution to the signal from different deeply bound states, based on particle binding energy, allowing identification of clear temperature windows in which each defect species can be studied. In the present case windows were established which allowed us to separate capture and emission occurring in the Mo nano-precipitate ensemble from processes occurring within the interstitial point defect population. DLTS measurements exploit the ability to controllably modulate the width of a surface depletion region (using pulsed bias voltages) over an ensemble of electrically active defects; for this work a surface Schottky barrier (SSB) formed by evaporation of Ti was used for this. In order to gain a sufficient depletion modulation range a rather low background equilibrium hole density was chosen ($1.5x10^{15}$ cm^{-3}) for all samples and Mo was introduced at a level of ~ 10^{15} atoms cm^{-3} in a region 0.7 - 1 µm below the Si surface. Although both hole and electron transitions were studied, the focus here is on the majority carrier capture and emission processes, since the aim is to clarify the size dependence of the associated rates. Electron (minority carrier) capture was observed to be fast and consistent with a Coulomb like attractive potential.

Isolated Mo atoms occupying interstitial sites produce a well-defined energy level in the gap with a thermal binding energy for holes of 0.29 eV [9] [10], whereas Mo nano-precipitates exhibit a higher degree of thermal stability but no well-defined emission rate from which a binding energy might be deduced. We determine an average binding energy for hole emission of approximately 0.47 eV, quite distinct from the point defect case. The associated DLTS spectrum is significantly broadened indicating a range of thermal emission rates for holes. A comparison of DLTS and SIMS data for Mo doped samples used in this work demonstrates clearly that the majority of the molybdenum atoms did not reside at the interstitial site. This is consistent with the findings below, that nano-precipitates, ranging in diameter from 2 nm and 10 nm, and containing between approximately 300 to 30,000 atoms, display electrical activity involving charge exchange of only a small numbers of electrons or holes. The number of holes, N, stored on the surface of a spherical nano-precipitate in thermal equilibrium is a function of diameter; for the range of particle sizes discussed in this work N

is estimated to vary from 5 for the smallest precipitate to 26 for the largest, assuming spherical geometry. All of the charge exchange processes measured here could be accounted for by single hole transitions i.e. N$\rightarrow$N-1 for hole emission and N-1$\rightarrow$N for hole capture.

The charge exchange kinetics for majority holes were studied using a cyclic bias pulse sequence applied to the SSB, viz. a zero bias "capture" pulse of variable time (10^{-7} s -10^{-2} s), preceded by a long (0.1 second) reverse bias "emission" pulse. The emission pulse depletes the semiconductor over the Mo containing region, bending the bands and extracting free carriers. Carrier capture transitions are then supressed during this phase of data collection during which pure hole emission is measured. The long emission pulse length ensures that the whole ensemble is prepared in a hole-deficient (N-1) configuration for the following capture pulse. The emission pulse also serves to measure the charge captured - only the fraction of the ensemble which succeeded in capturing holes will contribute to the magnitude of the subsequent hole emission signal. During the capture pulse, the SSB depletion collapses over the Mo containing region, the nano-precipitates become immersed in the equilibrium hole gas of the semiconductor and proceed to capture holes. The amplitudes of the emission capacitance transients, normalised to indicate the fractional charge occupancy ($\Delta C/\Delta C_{max}$), as a function of capture pulse width (and for a range of temperatures) are shown in Figure 2; these data provide the fundamental information needed to extract a capture rate and hence capture cross section.

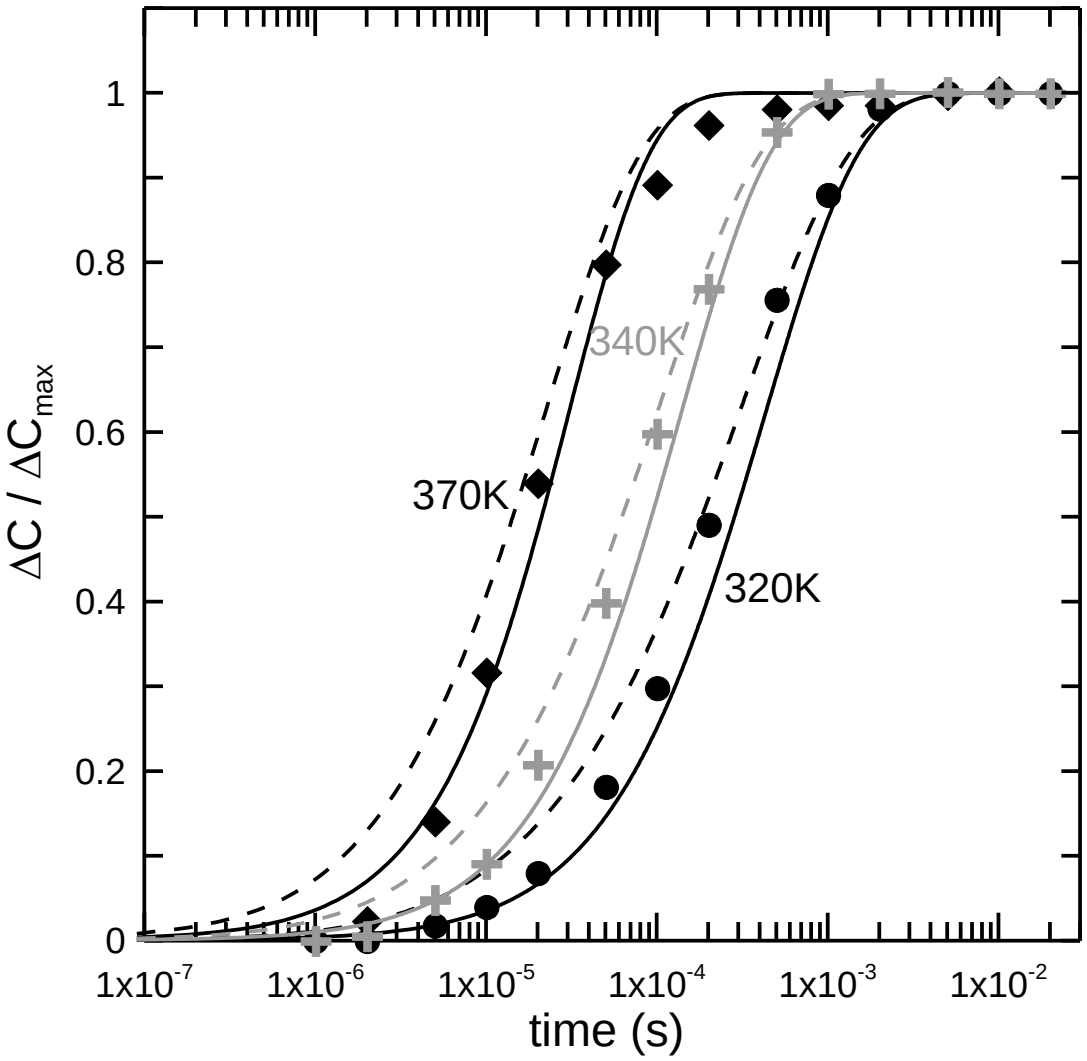

Figure 2. The capacitance signal resulting from the increase in stored charge as the fill pulse width is increased. The data are fitted to Gaussian (solid line) and Ostwald (dashed line) nanoprecipitate size distributions.

The general shape of this family of curves indicates that capture is more efficient at high temperatures, consistent with capture at a repulsive potential [8], through which holes in the tail of a Fermi distribution have a high probability of tunnelling: this is akin to an emission process (Fig 1) and the two processes have similar measured rates. As a result, both capture and emission play a role in the observed rate of return to equilibrium surface charge N during the capture phase; this is distinct from the more familiar point defect deep level response characterised by DLTS.

The freedom to add or to remove electrons from the Fermi surface of a metallic nano-precipitate is a charge exchange pathway quite distinct from particle exchange processes normally occurring at deeply bound states associated with point defects in semiconductors. In particular both capture and emission transitions for majority carriers (Figure 1) require completion of either a thermionic emission or a tunnelling transition process. Any change in the shape of the surrounding potential barrier due to precipitate size or instantaneous net surface charge will influence both majority carrier capture and emission in the same way: either increasing or decreasing both rates in the same sense. Capture and emission rate constants are not fixed quantities and are, moreover, strongly coupled. Confirmation of these ideas were directly obtained from the transient capacitance data which showed that shortening the size of the fill pulse consistently led to the faster emission transient in the measurement phase. Such behaviour is not expected and has not been reported for a single species of point defects for which thermal emission rates are independent of the capture properties. It is argued below that this behaviour arises naturally from a size distribution of nano-precipitates, for which majority charge capture and release are mediated by tunnelling through a size sensitive electrostatic potential.

The variation in electrostatic potential over the size distribution of precipitates for both the N and N-1 charge configurations plays a dominant role in controlling the single particle capture and emission tunnelling processes and was calculated for the case of spherical symmetry. Potentials were evaluated for nano-precipitates residing in the bulk, neutral semiconductor and depletion field environments in order to analyse both capture and emission phases of the experiments.

Previous calculations of potentials associated with metallic structures of small dimension have been reported [13]-[16] which indicate that for characteristic sizes below 10 nm, increased tunnelling rates can explain enhanced forward conduction for surface Schottky contacts and for scanning tunnelling I-V spectroscopy. The above calculations were performed analytically within the depletion approximation and under mean field theory. For the low background doping level and near

equilibrium capture processes explored experimentally here, the depletion approximation is inadequate. For accurate determination of potentials, Poisson's equation must include the semiconductor free electron and hole contributions to the local charge density: Debye screening is taken into account. Poisson's equation now becomes non-linear, and for spherical symmetry can be written:

$$\nabla^2 V(r) = \frac{\partial}{\partial r}\left(r^2 \frac{\partial V(r)}{\partial r} \right) = -\frac{e}{\varepsilon_s \varepsilon_0}\left[N_V e^{\left(\frac{eV(r)-E_g}{kT} \right)} - N_C e^{\left(-\frac{eV(r)}{kT} \right)} + N_D^+ - N_A^- \right] \quad (1)$$

Equation (1) is the first step towards determining the potentials required for the prediction of equilibrium hole capture and emission rates and consequently cross section estimates. However this equation alone does not take into account the influence of image force corrections. The image force accounts for the electrostatic interaction between the incoming particle and the polarisation charge induced on the metal as the particle moves closer. Performing this calculation revealed that image force barrier lowering is size dependent, and becomes significant (greater than several KT) for few nm scale metal structures. The potentials obtained, corrected for image force barrier lowering are shown in Figure (3) in which the calculated size dependence of image force lowering is shown as an inset. The latter calculation was performed using boundary conditions which ensured that during the approach of the incoming hole, both the surface potential and the total charge on the metal remained constant [17].

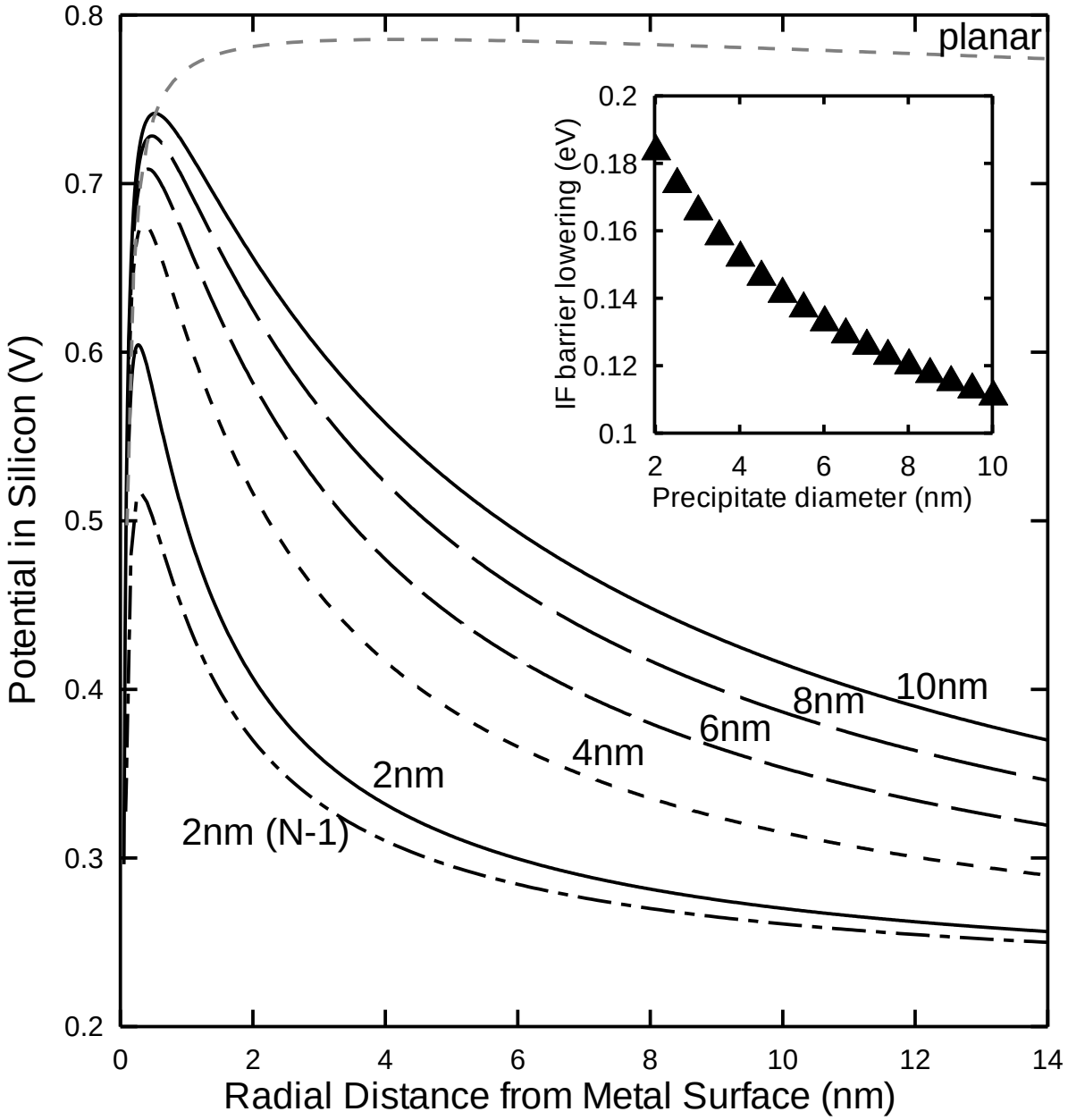

Fig 3. The form of the thermal equilibrium potential developed around nanoprecipitates as a function of size and for the equilibrium, N, charge state. For the 2 nm diameter particle, the potential is shown also for the (N-1) state. For comparison, the potential for a plane surface Molybdenum SB is also recorded.

These potentials, for spherical Mo nano-precipitates ranging from 2 to 10 nm in diameter are calculated for an equilibrium charge N, the charge configuration prior to (equilibrium) hole emission. For the smallest precipitate (2 nm diameter), the computed potential for the (N-1) charge state, the charge configuration associated with hole capture is given. The narrowing and image force lowering

of the surrounding potentials promotes faster tunnelling rates for both capture and emission. We note that at the smallest particle diameters, the computed potentials converge approximately to the Coulomb form: V(r) ≈ 1/ε(r-R) which would be obtained in the absence of dopant charge: in this size regime the potential spread is less than the average inter-dopant (B) atom spacing. It is useful to compare the scale of size associated potential narrowing at nano-precipitates with the spatial profile of the potential associated with a large area planer SSB. For consistency, the TM Mo was used in this calculations and the slowly varying potential is shown also in Fig.3.

The calculated potentials V(r) were used to evaluate the hole capture and emission rates (using the WKB approximation); tunnelling proceeds predominantly from the tail of the Fermi Dirac function for the hole gas in the semiconductor, f_s and the metal f_m. Tunnelling occurs over the three dimensional spherical surface and in order to improve the accuracy of the calculated tunnelling rate, and hence cross section estimate, care must be taken to correctly account for particle k vector distribution over the range of particle energies which contribute to tunnelling. Here we adopt the approach frequently used for computing tunnelling rates at STM tips and other small dimensional metallic structures [13], integrating the energy dependent tunnelling transmission coefficient over all perpendicular and parallel wave vectors ($E^{\perp}$ and $E_{//}$) involved in the tunnelling process. Spherical energy surfaces were assumed for semiconductor and metal close to the respective Fermi energies. This summation of leads to a particle transfer rate:

$$J = \int \exp\left[-2\sqrt{\frac{2m^*}{\hbar^2}} \int_{r_1}^{r_2} \sqrt{V(r) - E_{\perp}}\, dr \right] \int \rho(E)\left(f_s(E) - f_m(E) \right) dE_{//} dE_{\perp} \qquad (2)$$

Where r_1 and r_2 represent the extremities of the barrier V(r) for each tunnelling energy E. Values of hole capture cross section were obtained for a range of nano-precipitate diameters and temperatures; these are shown in Fig. 4. Clearly these computed cross sections exhibit strong size and temperature dependence. The size dependence emerges naturally from the progressive thinning of the hole repulsive potential barrier as the size is reduced. The temperature dependence of the cross section is a consequence of the narrowing of the effective barrier width for particles high in the Fermi tail.

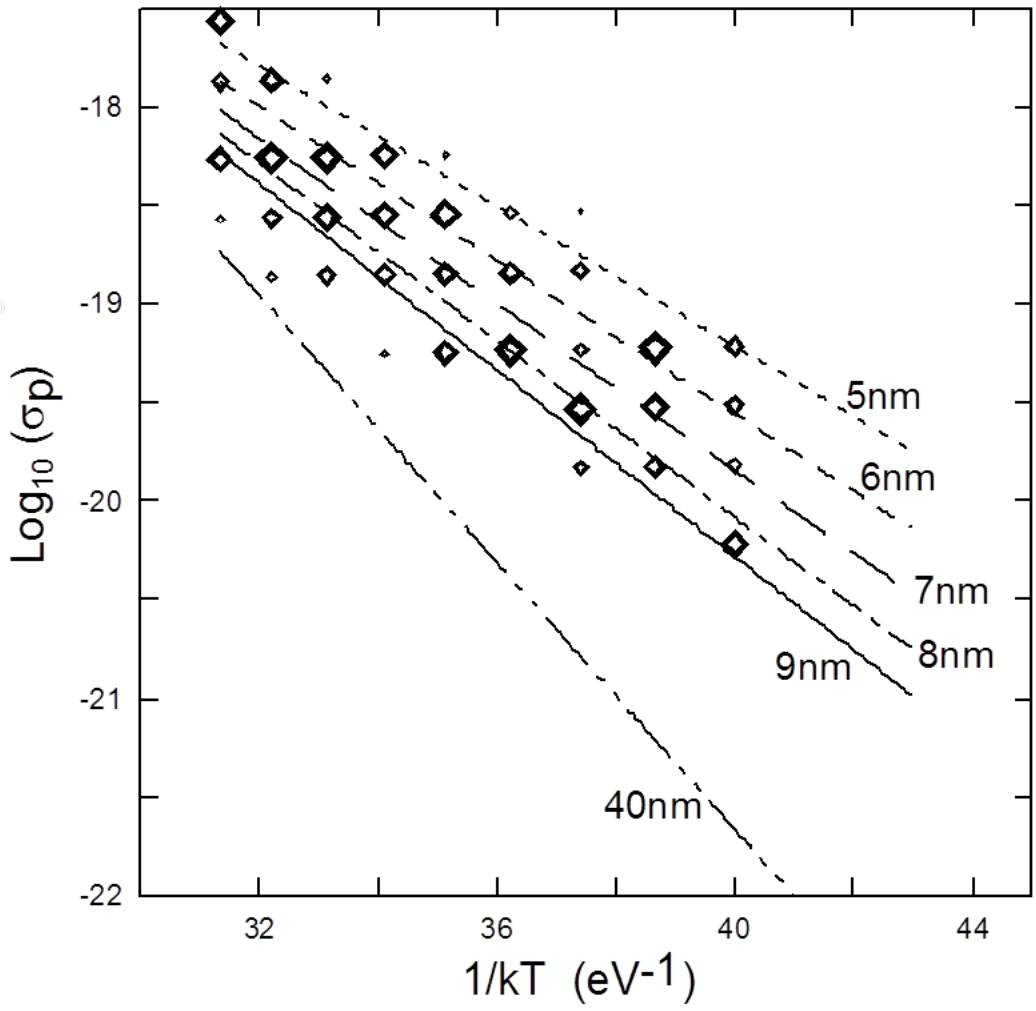

Figure 4. The computed capture cross sections for repulsive hole capture at nanoprecipitates. The range of experimentally determined cross sections for each precipitate size is also indicated. The experimental data can be accounted for particle sizes ranging from 5 nm to 9 nm diameter. A 40 nm diameter particle is included for comparison. The size of data points is scaled to match the contribution of a given sigma value to the signal as deduced from fitting.

The calculated cross sections for a 40 nm diameter particle are also shown on Fig. 4. For this larger, though substantially sub-micron size particle the cross section is ≈ 10^{-22} cm^2; at room temperature this value is close to those reported for capture into repulsive point defects [8] [18]. However, the room temperature value of σ for the smallest diameter shown is close to four orders larger than that for the 40 nm precipitate, much closer to reported values for charge neutral point defects.

The raw experimental data given in Fig.2 could not be reproduced using a single nanoparticle diameter; the association of a size distribution was required in order to get reasonable agreement. Two plausible size distribution functions were tested: Gaussian centred on 6 nm diameter and an Ostwald distribution function (characteristic of diffusion limited particle growth rates), with a particle diameter range 2-10 nm. These size ranges are consistent with the available electron energy loss and high-angle annular dark field TEM data [11] [12] on similar samples, and close to the smallest TM precipitate sizes measured to date using synchrotron radiation XRF imaging. The fits to both distribution functions are shown in Figure 2 and each fit includes the experimentally determined spatial profile. It was assumed that the chosen size distributions were valid over the entire spatial distribution. The highest temperature data samples had the largest fraction of the spatial distribution and for those data the Ostwald size distribution function matches more closely with the experimental data and is a plausible distribution function for nano-precipitation of slow diffusing TMs. For each fill pulse width, capture occurs into particles of varying size and therefore with varying capture rates. The range of cross sections which were measured to contribute to capture for each pulse width are also indicated in fig. 4.

10.4. Conclusion

In conclusion, we have produced single crystal, p-type Si structures which contain nano-precipitates formed from Mo atoms which were deliberately incorporated into the Si lattice. The electron and hole capture rates of the nano-precipitates were measured in order to understand the potential role played by sub 10 nm diameter metallic precipitates as recombination centres in Si; this question is

important for the future manufacture of multi-crystalline silicon solar cell technology. For an embedded metallic structure in a semiconductor, the equilibrium electrostatic configuration is dominated by the formation of a dipole layer (Schottky–Mott theory) and this constraint leads to an attractive potential for minority carriers but to a repulsive potential for majority carrier capture. Slow capture rates are therefore anticipated for majority carriers at such structures, and a likely consequence is they might exhibit efficient minority carrier trapping but inefficient carrier recombination. We show experimentally that majority carrier capture cross sections characteristic of metallic precipitates smaller in diameter than 5 nm are several orders of magnitude larger than those typical of repulsive capture at point defect at room temperature. In order to make spectroscopically resolvable capture rate measurements, the TM Mo was incorporated at a low atomic concentration ($10^{15}\,cm^{-3}$) and nano-precipitates formed during the thermal cycle applied to the samples. This procedure allowed us to detect and measure the nano-precipitate properties without interference from Mo point defect species using variable capture pulse length DLTS transient capacitance spectroscopy. Our experimental data were tested by calculating the cross sections for majority carrier capture and the potentials associated with repulsive capture at nm scale precipitates (assuming spherical geometry). For these low carrier density structures, it was necessary to take into account the Debye screening over the particle sizes investigated. It was determined that for sub 10 nm diameter particles, the repulsive capture cross section was increased by up to 3 orders of magnitude at room temperature. The experimentally determined range of cross sections for an Ostwald size distributed ensemble of nanoparticles was reproduced by our calculations for a diameter range of 2-10 nm. The repulsive capture process was determined to be strongly size dependant and sensitive to charge state; the observed temperature dependency was also reproduced.

This work demonstrates that very small metallic precipitates will act as important recombination centres in solar grade silicon. We note that solar (p-type) silicon typically has a background hole density which is an order of magnitude higher than that of the test samples used here. This will

further enhance the hole capture rate, as will the additional potential narrowing associated with a high value of N_A^+. These observations provide insight into to the mechanisms which "switch on" very small metallic precipitates as recombination centres. Moreover they point to the importance of gaining better control of the defect engineering required to prevent slow diffusing TM species from damaging the solar energy conversion efficiency of future MC silicon produced with reduced thermal budget. Our findings are not specific to the TM studied here, and apply to any sufficiently small metallic particles in a semiconductor. Such nanoparticles would seem to constitute a new class of recombination center.

10.5. Acknowledgements

We would like to thank the EPSRC (UK) for the funding and Professor Russel Gwilliam of the Surrey Ion Beam Centre for undertaking the Mo implants.

10.6. References

[1] R. M. Swanson, Science, **324**, 891, (2009)

[2] N. S. Lewis, Science, **315**, 798, (2007)

[3] International Energy Agency, Technology Roadmap, Solar Photovoltaic Energy, OECD/IEA, Paris (2014)

[4] M.M. Hand, S. Baldwin, et al., Renewable Electricity Futures Study, National Renewable Energy Laboratory, (2012)

[5] A. R. Peaker, V. P. Markevich, B. Hamilton, G. Parad, A. Dudas, A. Pap, E. Don, B. Lim,

J. Schmidt, L. Yu, Y. Yoon, and G. Rozgonyi, Phys. Status Solidi A **209,** 1821, (2012)

[6] T. Buaonassi, A. A. Isatratov, M. A. Marcus, B. Lai, Z. Cai, S. M. Heald and E. R Weber. Nature Materials **457**, (2005)

[7] M. A. Jensen, J. Hofstetter, A. E. Morishige, G. Coletti, B. Lai, D. P. Fenning and T. Buonassisi, Appl. Phys. Lett. **106**, 202104, (2015)

[8] A. C. Wang, L. Su Lu, and C. T. Sah, Physical Review B, **30**, 10, 5896, (1984)

[9] A. Rohatgi, R. H. Hopkins, J. R. Davis, and R. B. Campbell, Solid-State Electron., **23**, 1185, (1980)

[10] J. L. Benton, D. C. Jacobson, B. Jackson, J. A. Johnson, T. Boone, D. J. Eaglesham, F. A. Stevie, and J. Beccero, J. Electrochem. Soc. **146**, 1929, (1999)

[11] M.L. Polignano, C. Bresolin, G. Pavia, V. Soncini, F. Zanderigo, G. Queirolo and M. Di Dio, Materials Science and Engineering B, **53,** 300, (1998)

[12] S. Leonard, V. P. Markevich, A. R. Peaker, B. Hamilton, K. Youssef, and G. Rozgonyi, Phys. Status Solidi, **251**, 2201, (2014)

[13] G.D. J. Smit, S. Rogge and T.M. Klapwijk, Appl. Phys. Lett., **81**, 3852, (2002)

[14] L. Hao, P.A. Bennett, J. Appl Phys. **108,** 014303, (2010)

[15] N. V. Vostokov, and V.I. Shashkin, On the role of tunnelling in Metal-Semiconductor Nanocontacts, p211, (2004)

[16] M. D. Negoita and T.Y. Tan, J. App.l Phys. **94**, 5064, (2003)

[17] J.D. Jackson, Classical Electrodynamics, Wiley, (1999)

[18] M. Lax, Physical Review, **119**, 5, (1960)

11. Conclusion

To conclude, in this work we have investigated the effect of Mo, Ti and Fe in silicon and have reported several new results. The aim of this work has been to better understand the role of metallic impurities in silicon with the ultimate goal of finding ways to cost effectively reduce their negative effects on solar cell efficiency. This is especially important for lower purity “solar grade” cast silicon which has far higher impurity concentrations. With recent reports showing that grain boundaries are not necessarily the reason for lower efficiencies in multi-crystalline silicon,[1] the ability to effectively control the impact of impurity metals is essential in the quest to produce low cost, high efficiency solar cells. Although we have provided no direct solutions as to how this could be done in current large scale manufacturing plants, the new results we have reported will help to further understand passivation techniques.

In our work with Ti we have reported the almost complete passivation of Ti with hydrogen in n-type silicon. Under the right annealing conditions, the vast majority of all the observable Ti related peaks were removed after the incorporation of H. According to the theory it is likely that this is due to the creation of TiH_4 which is predicted to be electrically inactive [2]. However the electrically inactive titanium hydrogen complex was not stable, and a complete recovery of the Ti related peaks was observed in DLTS after annealing at 250 ^{o}C. There were three different electrically active Ti-H complexes observed, in contradiction to previous work [3]. We also showed that Ti in the substitutional lattice site is electrically inactive, which was confirmed by DFT calculations. After ion implantation and annealing over 650 ^{o}C, far more Ti atoms will move into substitutional lattice sights in FZ, than in Cz due to the larger quantities of oxygen consuming vacancies in Cz silicon. Both pieces of work show there are ways to reduce the effect of Ti, which is a very effective recombination centre and a traditionally difficult to getter metal due to its low diffusivity.

One of the most interesting results from this work was the observation of the presence of Mo nano-precipitates in the range of 2-10 nm by TEM images and DLTS measurements. The electrical

measurements show different properties to conventional point defects and larger precipitates. The nano-precipitates had large minority carrier capture cross sections and mid gap energy levels which make them very effective recombination centres. We believe that it is likely that these nano-precipitates will form from other slow diffusing transition metals in relatively low purity, cast solar silicon, and could have a significant effect on solar cell efficiency. In our case, it is likely that the nano-precipitate we have observed is the disilicide $MoSi_2$ which is very stable, and could not be removed without melting. The presence of very stable nano-precipitates, which have a large effect on minority carrier life time could be an important reason between the efficiency gaps in multi-crystalline and single crystal solar cells. Numerical modelling based on Poisson's equations have confirmed that nano-precipitates made from any transition metal our likely to be very powerful minority carrier recombination centres. Therefore there is a huge amount of further work that can be done on the field of nano-precipitates to help understand the origin of their presence and the effect they will have on solar efficiency. In particular detailed thermal studies examining intentionally contaminated silicon with various slow diffusing transition metals could help to further understand the formation and size of precipitates in different types of silicon. The electrical effects of the precipitates could then be studied using a mixture of DLTS, LDLTS and MCTS. Unfortunately this work was beyond the scope of this PhD as it would require extensive time on a TEM to examine the precipitates, which was not available to us.

Another important discovery from this work was the observation of the formation of a Fe-H complex. This work is of particular significance due to the scientific debate over the potential passivating effect that hydrogen has on iron. While theory [4] and some experimental papers [5] have suggested that hydrogen will not passivate interstitial iron, some experiments have shown that hydrogen does appear to passivate iron [6]. Our work shows that the Fe-H complex we have formed is electrically active, and that the complex would not be stable at the temperatures used in the passivation technique. However this poses the exciting question of what causes the increase in carrier lifetime caused by annealing with a hydrogen rich silicon nitride layer seen in ref [6]. A

collaboration has been set up with Australia National University (ANU) to repeat their experiment from [6] using single crystal silicon instead of multi-crystalline, so DLTS can be used to examine the presence of Fe. Very recent preliminary results show that the DLTS signals from Fe_i centres are not present after the passivation technique. Much detailed further work is needed to understand how the passivation process is working and how stable it is. If the iron really has been passivated by the hydrogen, then it should be possible to de-passivate it after certain annealing conditions. As Iron is typically the most common metallic impurity in solar silicon, it is a very interesting and important topic with a lot of scope for further work.

References

[1] A.R. Peaker, V. P. Markevich, B. Hamilton, G. Parada, A. Dudas, A. Pap, E. Don, B. Lim, J. Schmidt, L. Yu, Y. Yoon, and G. Rozgonyi, Phys. Status Solidi A, vol. 209, p. 1884-1893, (2012).

[2] D. J. Backlund and S. K. Estreicher, Structural, electrical, and vibrational properties of Ti-H and Ni-H complexes in Si, Phys. Rev. B, vol. 82, p. 155208 (2010).

[3] W. Jost and J. Weber, Titanium-hydrogen defects in silicon, Phys. Rev. B vol. 54, R11038 (1996).

[4] S. K. Estreicher, M. Sanati, and N. G. Szwacki, “Fundamental Interactions of Fe in silicon : First-Principles Theory,” Solid State Phenom., vol. 133, pp. 233–240, 2008.

[5] P. Karzel, A. Frey, S. Fritz, and G. Hahn, “Influence of hydrogen on interstitial iron concentration in multicrystalline silicon during annealing steps,” J. Appl. Phys., vol. 113, no. 11, p. 114903, 2013.

[6] A. Liu, C. Sun, and D. Macdonald, “Hydrogen passivation of interstitial iron in boron-doped multicrystalline silicon during annealing,” J. Appl. Phys., vol. 116, no. 19, p. 194902, Nov. 2014.